IAEA TECDOC SERIES

IAEA-TECDOC-1773

IAEA-TECDOC-1773

Use of Neutron Beams for Materials Research Relevant to the Nuclear Energy Sector

IAEA
International Atomic Energy Agency

USE OF NEUTRON BEAMS FOR MATERIALS RESEARCH RELEVANT TO THE NUCLEAR ENERGY SECTOR

The following States are Members of the International Atomic Energy Agency:

AFGHANISTAN
ALBANIA
ALGERIA
ANGOLA
ARGENTINA
ARMENIA
AUSTRALIA
AUSTRIA
AZERBAIJAN
BAHAMAS
BAHRAIN
BANGLADESH
BELARUS
BELGIUM
BELIZE
BENIN
BOLIVIA, PLURINATIONAL STATE OF
BOSNIA AND HERZEGOVINA
BOTSWANA
BRAZIL
BRUNEI DARUSSALAM
BULGARIA
BURKINA FASO
BURUNDI
CAMBODIA
CAMEROON
CANADA
CENTRAL AFRICAN REPUBLIC
CHAD
CHILE
CHINA
COLOMBIA
CONGO
COSTA RICA
CÔTE D'IVOIRE
CROATIA
CUBA
CYPRUS
CZECH REPUBLIC
DEMOCRATIC REPUBLIC OF THE CONGO
DENMARK
DJIBOUTI
DOMINICA
DOMINICAN REPUBLIC
ECUADOR
EGYPT
EL SALVADOR
ERITREA
ESTONIA
ETHIOPIA
FIJI
FINLAND
FRANCE
GABON
GEORGIA
GERMANY
GHANA
GREECE
GUATEMALA
GUYANA
HAITI
HOLY SEE
HONDURAS
HUNGARY
ICELAND
INDIA
INDONESIA
IRAN, ISLAMIC REPUBLIC OF
IRAQ
IRELAND
ISRAEL
ITALY
JAMAICA
JAPAN
JORDAN
KAZAKHSTAN
KENYA
KOREA, REPUBLIC OF
KUWAIT
KYRGYZSTAN
LAO PEOPLE'S DEMOCRATIC REPUBLIC
LATVIA
LEBANON
LESOTHO
LIBERIA
LIBYA
LIECHTENSTEIN
LITHUANIA
LUXEMBOURG
MADAGASCAR
MALAWI
MALAYSIA
MALI
MALTA
MARSHALL ISLANDS
MAURITANIA
MAURITIUS
MEXICO
MONACO
MONGOLIA
MONTENEGRO
MOROCCO
MOZAMBIQUE
MYANMAR
NAMIBIA
NEPAL
NETHERLANDS
NEW ZEALAND
NICARAGUA
NIGER
NIGERIA
NORWAY
OMAN
PAKISTAN
PALAU
PANAMA
PAPUA NEW GUINEA
PARAGUAY
PERU
PHILIPPINES
POLAND
PORTUGAL
QATAR
REPUBLIC OF MOLDOVA
ROMANIA
RUSSIAN FEDERATION
RWANDA
SAN MARINO
SAUDI ARABIA
SENEGAL
SERBIA
SEYCHELLES
SIERRA LEONE
SINGAPORE
SLOVAKIA
SLOVENIA
SOUTH AFRICA
SPAIN
SRI LANKA
SUDAN
SWAZILAND
SWEDEN
SWITZERLAND
SYRIAN ARAB REPUBLIC
TAJIKISTAN
THAILAND
THE FORMER YUGOSLAV REPUBLIC OF MACEDONIA
TOGO
TRINIDAD AND TOBAGO
TUNISIA
TURKEY
UGANDA
UKRAINE
UNITED ARAB EMIRATES
UNITED KINGDOM OF GREAT BRITAIN AND NORTHERN IRELAND
UNITED REPUBLIC OF TANZANIA
UNITED STATES OF AMERICA
URUGUAY
UZBEKISTAN
VANUATU
VENEZUELA, BOLIVARIAN REPUBLIC OF
VIET NAM
YEMEN
ZAMBIA
ZIMBABWE

The Agency's Statute was approved on 23 October 1956 by the Conference on the Statute of the IAEA held at United Nations Headquarters, New York; it entered into force on 29 July 1957. The Headquarters of the Agency are situated in Vienna. Its principal objective is "to accelerate and enlarge the contribution of atomic energy to peace, health and prosperity throughout the world''.

IAEA-TECDOC-1773

USE OF NEUTRON BEAMS FOR MATERIALS RESEARCH RELEVANT TO THE NUCLEAR ENERGY SECTOR

INTERNATIONAL ATOMIC ENERGY AGENCY
VIENNA, 2015

COPYRIGHT NOTICE

For further information on this publication, please contact:

Physics Section
International Atomic Energy Agency
Vienna International Centre
PO Box 100
1400 Vienna, Austria
Email: Official.Mail@iaea.org

Printed by the IAEA in Austria
October 2015

IAEA Library Cataloguing in Publication Data

Use of neutron beams for materials research relevant to the nuclear energy sector. — Vienna : International Atomic Energy Agency, 2015.
p. ; 30 cm. — (IAEA-TECDOC series, ISSN 1011–4289; no. 1773)
ISBN 978–92–0–108915–1
Includes bibliographical references.

1. Neutron beams — Experiments. 2. Nuclear reactors — Materials. 3. Materials — Research. I. International Atomic Energy Agency. II. Series.

IAEAL 15–00993

FOREWORD

Nuclear technologies such as fission and fusion reactors, including associated waste storage and disposal, rely on the availability of not only nuclear fuels but also advanced structural materials. In 2010–2013, the IAEA organized and implemented the Coordinated Research Project (CRP) on Development, Characterization and Testing of Materials of Relevance to Nuclear Energy Sector Using Neutron Beams. A total of 19 institutions from 18 Member States (Argentina, Australia, Brazil, China, Czech Republic, France, Germany, Hungary, Indonesia, Italy, Japan, Netherlands, Republic of Korea, Romania, Russian Federation (two institutions), South Africa, Switzerland and United States of America) cooperated with the main objective to address the use of various neutron beam techniques for characterization, testing and qualification of materials and components produced or under development for applications in the nuclear energy sector.

This CRP aimed to bring stakeholders and end users of research reactors and accelerator based neutron sources together for the enhanced use of available facilities and development of new infrastructures for applied materials research. Work envisioned under this CRP was related to the optimization and validation of neutron beam techniques, including facility and instrument modifications/optimizations as well as improved data acquisition, processing and analysis systems. Particular emphasis was placed on variable environments during material characterization and testing as required by some applications such as intensive irradiation load, high temperature and high pressure conditions, and the presence of strong magnetic fields. Targeted neutron beam techniques were neutron diffraction, small angle neutron scattering and digital neutron radiography/tomography.

This publication is a compilation of the main results and findings of the CRP, and the CD-ROM accompanying this publication contains 19 reports with additional relevant technical details.

The IAEA acknowledges the valuable contributions of the individual participants and the support of the international experts in contributing to and reviewing this publication, in particular M. Grosse (Germany). The IAEA officers responsible for this publication were D. Ridikas of the Division of Physical and Chemical Sciences and V. Inozemtsev of the Division of Nuclear Fuel Cycle and Waste Technology.

EDITORIAL NOTE

This publication has been prepared from the original material as submitted by the contributors and has not been edited by the editorial staff of the IAEA. The views expressed remain the responsibility of the contributors and do not necessarily represent the views of the IAEA or its Member States.

Neither the IAEA nor its Member States assume any responsibility for consequences which may arise from the use of this publication. This publication does not address questions of responsibility, legal or otherwise, for acts or omissions on the part of any person.

The use of particular designations of countries or territories does not imply any judgement by the publisher, the IAEA, as to the legal status of such countries or territories, of their authorities and institutions or of the delimitation of their boundaries.

The mention of names of specific companies or products (whether or not indicated as registered) does not imply any intention to infringe proprietary rights, nor should it be construed as an endorsement or recommendation on the part of the IAEA.

The IAEA has no responsibility for the persistence or accuracy of URLs for external or third party Internet web sites referred to in this publication and does not guarantee that any content on such web sites is, or will remain, accurate or appropriate.

CONTENTS

1. INTRODUCTION

1.1. BACKGROUND

Long term nuclear energy security will strongly depend on the availability of not only nuclear fuels but also advanced structural and functional materials. These materials have to withstand extreme conditions: high temperature/pressure, intense neutron irradiation, strongly corrosive environments, presence of magnetic/electric fields, and all that in combination with complex loading states and cyclic operation histories. Further developments in advanced materials for the existing thermal reactors may improve safety margins, reduce the frequency of component replacement, ensure higher burn-ups and, therefore fuel cycle economics and safety. For advanced future reactors (e.g. fast reactors, high temperature reactors, fusion reactors, accelerated driven systems), the development of advanced materials is crucial due to the extreme environment and operation conditions associated with these innovative systems.

Engineering components in all these nuclear technologies such as reactors, waste storage and disposal, components, fuels, cladding and waste forms, rely on development of advanced materials for their economic, safe, and reliable operation. The demands of quality control on each component to be used in the nuclear energy sector are very stringent and are critical in terms of acceptability and licensing. These, in turn, call for the development and fabrication of components with high quality and reliability. This process demands the characterization of materials and fabricated components during and after the fabrication process. The testing of these parts after use provides information on their behaviour under various conditions of operation and/or in the diagnosis in case of their failure.

The crystallographic, chemical and micro-structure, mechanical strength, anisotropy in properties, response to external stresses, radiation resistance, and in certain cases magnetic fields are some of the characteristics that determine the suitability of a material for use in advanced present and future nuclear energy sector. To achieve these transformational advances in materials performance a science-based approach is needed. The science-based approach combines fundamental understanding of materials behaviour at the micro-structural level combined with phase-field and atomistic theories, high precision experimental and characterization techniques including advanced modelling and simulation tools. Up to now it is extremely difficult to forecast material behaviour on long-term basis whereas radiation, thermo-mechanical loading and chemical attacks all combine to severely impair their states. Moreover, the knowledge gained remains mostly empirical and cannot be easily extrapolated to new materials, new environments, or new operating conditions, and therefore calls for in-depth investigations.

1.2. USE OF NEUTRON BEAMS FOR MATERIALS RESEARCH

Various techniques have been developed to measure material properties at the microscopic and macroscopic level. X rays and charged particle beams are typically useful in the study of thin samples. Allied techniques such as positron annihilation spectroscopy (PAS), scanning tunnelling microscopy (STM), electron microscopy (EM), and other testing tools, each have a role to play in materials characterization, ranging from the atomistic level to the macroscopic scale. Neutrons are known as a unique bulk probe penetrating deep within a sample and without damaging the structure of the material under examination. The special nature of neutron interaction with matter provides important complementary and supplementary data to other techniques. Another advantage of neutrons is that they are sensitive to hydrogen

and other light elements even in the presence of heavy elements. Neutrons also can easily distinguish elements with close atomic numbers like, for example, Ni and Cr, even isotopes of individual elements, what would be impossible with X rays. Therefore, neutron beam facilities might play a specific role in such developments for testing and characterization of new nuclear fuels and structural materials or components. Research reactors (RR) have the potential to provide all necessary infrastructures in addition to neutron beams as a probe for advanced material testing and characterization. Dedicated in-core irradiation channels, material test loops, auxiliary facilities as hot laboratories, are often available at research reactors to provide realistic conditions for this purpose.

The large penetration depth and selective absorption of neutrons make them a powerful tool in non-destructive testing (NDT) of materials with large samples. Residual stress formed in a material during manufacturing, welding, utilization or repairs can be measured by means of neutron diffraction (ND). In fact neutron diffraction is the only NDT method, which can facilitate 3-D mapping of residual stress in a bulk component. Such studies are important in order to improve the quality of engineering components in production and to optimise design criteria in applications. Anisotropies in macroscopic properties like thermal and electrical conductivities, mechanical properties of materials used for instance in fuel elements depend on the textures developed during their preparation or thermal treatment, external thermal, chemical or radiation exposure. Such experiments can be also efficiently studied by using neutron diffraction technique. Very attractive could be the so called in-situ neutron diffraction investigations of samples under external thermo-mechanical load conditions.

Small Angle Neutron Scattering (SANS) is another method for investigation of structure inhomogeneities in a large scale of dimensions between 0.5nm and 5μm, therefore applicable for material science in terms of material structure changes (e.g. forming of the aggregates, clusters, precipitates, pores, etc.). Again thanks to deep penetration of neutrons, both atomic and macroscopic structure of materials can be derived. SANS is highly isotope-specific and is suitable for investigation of liquids as well as solids. Investigation of materials in the presence of magnetic fields (fusion technology) is also possible by SANS thanks to the neutron spin. Further advantage of SANS is a possibility to carry out so called in-situ experiments with samples under external load (variable temperatures, mechanical tension/compression, irradiation environments, magnetic fields, etc.)

Neutron imaging (NI) also uses the property that neutrons deliver high penetration through bulk material layers including heavy elements. Therefore, macroscopic examination of nuclear fuel (U or Pu) with respect to production quality, enrichment, burnable poison or fuel kernels distribution is possible. Study of spent fuel with respect to pellet integrity, fission product distribution and swelling also could be performed. Such investigations can be extended to fuel element cladding performance, in particular the hydrogen ingress after normal or accidental operation. Other fields where neutron radiography is advantageous are: quality control of neutron absorbing material with respect to homogeneity, inspection of welds for nuclear components, macroscopic study of wall materials from fusion test facilities after long term exposure, etc.

The above experimental techniques have a great potential to significantly contribute to multi-scale understanding of fuels and structural materials for nuclear systems and in dealing with scientific and engineering aspects of nuclear materials. In particular, they are able to support an experimental data base on nuclear materials for establishing multi-scale models and simulations as validated predictive tools for the design of nuclear systems, fuel/structure

component fabrication and performance. Some experiments could be specifically designed to serve as a reference data to validate the models. Therefore, combining experimental and theoretical knowledge from diverse fields of material research will benefit each.

1.3. PURPOSE AND STRUCTURE OF THIS PUBLICATION

In 2010-2013 the IAEA organized and implemented a Coordinated Research Project (CRP) on Development, Characterization and Testing of Materials of Relevance to Nuclear Energy Sector Using Neutron Beams. As it was required, the CRP participants employed at least one of the neutron beam techniques mentioned above in their Research Contracts/Agreements.

As stated in the CRP proposal document the overall objective of this CRP was to employ advanced neutron beam techniques for solving problems of current interest to materials research for the nuclear energy sector, to standardize and qualify relevant experimental techniques and modelling methods, and to promote and establish collaboration among participants of the project and additional interested parties. The specific objectives of this CRP were to:

- Investigate and characterise materials using neutron beams under extreme conditions relevant for present and future nuclear technologies, e.g. intensive irradiation load, high temperature/pressure/corrosive environment, magnetic fields for fusion, etc.;
- Optimize and validate advanced neutron beam experimental and modelling techniques as well as processes of data acquisition and analysis, and to develop expertise in characterization and testing of materials in the nuclear energy sector;
- Create an experimental database to contain reference data to validate the models and calculation tools in nuclear material research;
- Bring the stakeholders and end users of RRs together for the enhancement of available facilities for applications of RRs in material research relevant to the nuclear energy sector, including nuclear fission and fusion technologies.

As the main output of the above mentioned CRP, this publication aims to expand the knowledge and understanding of material behaviour in terms of their characterization and qualification under extreme conditions for nuclear energy technologies, and also to contribute to the enhancement of utilization and applications of research reactor and accelerator based neutron sources.

Through a great number of contributed papers, concrete examples are given with relevant technical information including some additional materials supplied by the international experts describing the current status of use of diverse neutron beam techniques for materials research targeting the nuclear energy sector.

The present report consists of six technical sections describing the main results achieved during this CRP, list of references, list of contributors to drafting and review, and list of individual paper contributors together with their affiliations and individual paper titles. This publication also includes an attached CD-ROM, in which all 18 individual technical reports are included electronically.

2. RESULTS ACHIEVED

Nuclear technologies rely on the availability of advanced fuel and structural materials. These structural materials have to be able to resist extreme conditions like for instance high neutron, proton and gamma fluxes and fluencies, high temperatures, or corrosive and abrasive media and combinations of them. In particular new concepts for nuclear energy production like fusion or next generation fission reactors requires materials suitable for the application at temperatures up to 1000°C under strong irradiation resulting in atomic displacements up to 120 dpa (displacement per atom). The very high safety standards valid for nuclear installations involve the excluding of material failure under all real operation or hypothetical incident-accident conditions too. To predict the material behaviour even at the end of the usage, the structural processes occurring have to be understood. These processes can result in the degradation of the mechanical properties. Examples are thermal ageing, irradiation and hydrogen embrittlement, formation or relaxation of residual stresses, corrosion and erosion or material fatigue. In the development phase of new reactor concepts the material behaviour during operation and transient conditions has to be understood, often by extrapolation of the known behaviour.

The material degradation processes can only be understood if the changes in the micro-structural of the material are known. Neutron based methods like neutron diffraction (ND), small angle neutron scattering (SANS) or neutron imaging (NI) techniques are powerful tools to investigate the micro-structure of materials in the length scale from atomic elastic displacement from 10^{-4} nm by ND via nano-scale precipitates by SANS to macroscopic dimensions by NI. Due to the large penetration depth of neutrons for many materials, several sample environments can be applied providing the possibility of in-situ experiments in special dedicated high temperature or high pressure chambers. For nuclear materials it is of particular interest because they are often activated after irradiation and have to be shielded.

Below text aims to introduce briefly some basic principles, laws and relations on neutron scattering, so some less experienced readers can follow easier the material presented in the coming sections.

The position of the Bragg peaks of neutron diffraction (ND) is determined by Bragg's law:

$$n\lambda = 2d_{hkl} \sin\theta \tag{1}$$

where n is the harmonics number, λ the neutron wave length, d_{hkl} the distance of the lattice plane hkl and θ the Bragg angle. The differentiated form of Eq. (1) is the basis of the measurements of lattice strain ε. For angular dispersive measurements it is given by the following equation:

$$\varepsilon = \frac{\Delta d}{d} = -\cot\theta\,\Delta\theta \tag{2a}$$

For the time of flight (TOF) method of neutron diffraction the strain can be determined by:

$$\varepsilon = \frac{\Delta d}{d} = \frac{\Delta t_{of}}{t_{of}} \tag{2b}$$

where t_{of} is the time of flight.

The Bragg peak intensity I_{hkl} and shape of neutron diffraction is connected with the structure, the volume fraction, the texture and the lattice distortion:

$$I_{hkl} \sim V / v \; p \left|F_{hkl}\right|^2 T_{hkl} \; e^{-2M} \tag{3}$$

In Eq. (3) V is the volume of the phase in the gauge volume, v the volume of the unit cell, p the multiplicity factor, F_{hkl} the structure factor, T_{hkl} the texture factor and M a parameter related to the averaged displacement of an atom from its mean position.

Information about type, size distribution and volume fractions of inhomogeneities with dimensions between 1 and 100 nm can be obtained by means of small angle neutron scattering (SANS). The dependence of the differential macroscopic scattering cross section $d\Sigma/d\Omega$ on the scattering vector Q measured in the small angle scattering experiment of inhomogeneities in a matrix (diluted system, no correlations between the precipitates) can be described by:

$$\frac{d\Sigma(Q)}{d\Omega} = \int_0^\infty D_V(R) \; R^3 \; \Delta\eta^2(R) \; \Phi(Q,R) \; dR \tag{4}$$

where R is the characteristic dimension of the inhomogeneities, $D_V(R)$ the volume distribution function, $\Delta\eta^2(R)$ the scattering contrast and $\Phi(Q,R)$ the Fourier transform of the shape of the inhomogeneities known as shape factor. By applying SANS to material systems with ferromagnetic components the differences between magnetic and nuclear scattering contrast can be used to obtain hints about the composition of the inhomogeneities and to separate volume fraction and contrast to determine the volume fraction quantitatively.

Neutron imaging (NI) or neutron radiography provides the possibility to determine the material distribution on a macroscopic scale with a spatial resolution down to about 10 µm. The pixel wise contrast in the transmission resulting in the radiography image can be described by:

$$\frac{I(x,y,\lambda) - I_B(x,y,\lambda)}{I_0(x,y,\lambda) - I_B(x,y,\lambda)} = \mathrm{T(x,y,}\lambda) = e^{-\Sigma_{total}(x,y,\lambda)/l} \tag{5}$$

where I, I_0 and I_B are the intensity behind and before the sample and the background intensity, respectively, x and y the pixel indices, T the transmission Σ_{total} the total macroscopic neutron cross section and l the neutron path length through the material. The total macroscopic neutron cross section depends on the isotope composition:

$$\Sigma_{total} = \sum_i N_i \sigma_i \tag{6}$$

with N as the number density of the isotope, i the isotope index and σ the microscopic neutron cross-section.

Neutron tomography (NT) allows a 3-dimensional reconstruction of the sample by measurement of a certain numbers of 2-dimensional radiography projections given by the sampling theorem.

2.1. INVESTIGATION OF OXIDE-DISPERSED-STRENGTHENED STEELS

Increasing the strength of constructional materials allows reducing the amount of material used in the manufacturing of various components and significantly increase their lifetime. In addition to improving mechanical properties by the production process of the materials for the nuclear industry (steel, structured alloys, etc.) the actual problem is to improve their radiation resistance too, i.e. to reduce their tendency to embrittlement and vacancy swelling. One of the most promising ways to solve this problem is to use the effect of metal or alloy hardening due to the formation of chemically stable non-metallic dispersed phases of submicron size, which inhibit the dislocations movement in the material.

At present, one of the most promising materials for future nuclear applications are the oxide-dispersed-strengthened (ODS) steels, which exhibit low yield strength, good fatigue and corrosion resistance, good uniform elongation, high initial strain hardening rates, a high strain rate sensitivity (the faster it is crushed the more energy it absorbs), high irradiative resistance and low creep rate. The absence of nickel and other alloying elements provide a rapid loss of activity of the utilized fuel elements.

ODS steels have a microstructure consisting of a soft ferrite matrix containing islands of martensite as the secondary phase (martensite increases the tensile strength). These alloys are made by mechanically alloying of steel powders with fine ceramic yttrium-oxide powder, to create a matrix in which very tiny oxide particles on a submicron scale are dispersed. These very fine particles make ODS alloys much stronger at high temperatures than similar alloys made by some different ways. Such extreme processing is necessary because yttrium oxide (Y_2O_3) is insoluble in molten steel. It is expected that nano-composited ferritic ODS steels expand the operating temperatures up to 800ºC.

In the above context, the most important task of material science is to understand the processes which occur during precipitation hardening in steels and alloys and which can help to prepare materials purposefully with the desired mechanical properties. Precipitation strengthening process can take place in the hardened material as a result of annealing at a certain temperatures or under irradiation. It is well known that the strength, creep resistance and radiation resistance of hardened material depend on the dispersed phase state: the degree of its crystal lattice coherence with matrix lattice, the location of nano-particles precipitation and their size. In addition, the precipitation of second-phase particles is accompanied by a lattice spacing changes in the matrix phase and, thus, the appearance of micro-strain, which has a significant effect on the materials characteristics.

Important role in the study of dispersion hardening processes occurring in structural materials play the diffraction and the small angle scattering of thermal neutrons. Both techniques have unique capabilities to determine the materials microstructure due to the high accuracy of the results, the possibility of analysis of multiphase materials, and especially the deep penetration length of neutrons, which is hundred times greater than the penetration length of X rays.

In this part of the report, research on various types of steel samples is presented employing high-resolution neutron diffraction (ND) and small angle neutron scattering (SANS). In particular, through a cooperative work within this CRP some investigations of ODS austenitic as well as ferritic steels, which are mainly used as structural materials for nuclear reactor components.

2.1.1. Use of neutron diffraction and small angle neutron scattering for steel studies

Precipitated phases can be observed and studied directly or through effects, which they produce in material microstructure. An analysis of the shape (width in the simplest case) of diffraction peaks can yield information on lattice distortions in individual grains (micro-strain) and their sizes that can be then connected with precipitated phases. These data can be obtained with equal success at both types of neutron diffractometers, with monochromatic beam or time-of-flight (TOF), if the resolution of a diffractometer is good enough (of the order of $\Delta d/d \sim 10^{-3}$). Especially convenient is the peak widths analysis which can be realized by using data obtained with a TOF diffractometer because of its very simple functional dependence of the peak width on the interplanar spacing (so called Gaussian peak shape approach):

$$W^2 = C_1 + (C_2 + C_3)\, d^2 + C_4\, d^4 \qquad (7)$$

where W is the peak width, C_1 and C_2 are the constants defining the diffractometer resolution function and known from measurements with a reference sample, $C_3 = (\Delta a/a)^2$ is the unit cell parameter dispersion (micro-strain), and C_4 is the constant related to the crystallite size (the so called modified Williamson-Hall analysis). The $W(d)$ relation should be modified slightly if Lorentzian profiles contribute to the peak shape (see, for instance, details provided in [1]).

With SANS one can probe structures at length scale between ~1 and ~100 nm by analysing neutron scattering into small scattering angles. ODS steel studies by SANS technique are based on the difference between the mean scattering length densities of the precipitated particles (Y_2O_3 or others) and homogeneous medium (steel matrix). SANS can be used for determination of the average radius, number density, and volume fraction of particles if their size is in nanometer range. Sometimes the size and number density of oxide nano-particles in steel can be effectively and quantitatively determined using combined measurements of SANS and small-angle X ray scattering (SAXS) data. Based on the difference of the SANS and SAXS intensity in absolute units, the compositions of the oxide nano-precipitates can be determined [2]. The same information can be obtained by SANS measurements in a strong magnetic field, which helps to separate the SANS intensity into nuclear and magnetic components (see, for instance, [3]) and suppress artefacts caused by scattering and refraction on magnetic domain walls.

2.1.2. Summary of results on the investigation of oxide-dispersed-strengthened and related steels

At the beginning of the CRP some initial work plan on research with the ODS and related steels was established among the partners of the project. In the first step, investigations were performed at room temperature with elastic deformation only. After, the same specimens were subjected to cyclic load at elevated temperatures (up to 1000ºC) for plastic deformation. Aspects investigated were inter-granular strains, residual stress and peak broadening. The deformed specimens were then available for SANS measurements to compare their initial and deformed microstructure. A first round of SANS measurements was performed on well characterized specimens. In brief, within the CRP six experiments were fully or partially dedicated to the studies of ODS, namely:

- "Characterization of Y_2O_3 particle distribution in oxide dispersion strengthened Eurofer steel for nuclear applications by means of SANS and ND", ENEA, Italy.
- "Microstructural investigation of ODS ferritic steels", BNC, Hungary.

- "Ferrite–martensite steels dispersion hardening studied by TOF neutron diffraction", JINR, Russia.
- "Study of ODS martensitic/ferritic materials", LLB, France.
- "Combined SANS and diffraction studies to investigate the structure property relationship of Generation IV reactor candidate materials and of structural components", JRC, The Netherlands.
- "Development, characterization and testing of materials of relevance to nuclear energy sector using neutron beams", LANL, USA.

The most important results obtained in the frame of these topics are discussed below.

Characterization of Y_2O_3 particle distribution in oxide dispersion strengthened Eurofer steel for nuclear applications by means of SANS and ND

Several of 9-14 Cr Eurofer-ODS ferritic/martensitic steel samples (9 to 14 percentage of chromium), submitted to different thermo-mechanical treatments and differing in elemental composition, were investigated by neutron diffraction with the D20 instrument (ILL, Grenoble, France). The Rietveld analysis of the high resolution neutron diffraction data indicate the contribution corresponding to Y_2O_3 is comparable to the experimental error, so the real stoichiometry has to be clarified (Fig. 1).

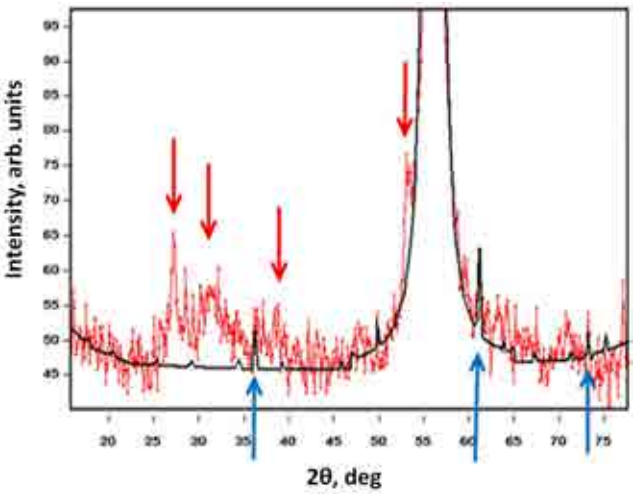

FIG. 1. A representative part of neutron diffraction pattern measured with the D20 diffractometer at ILL (Grenoble). The red arrows show the presence of unknown phases not corresponding to Y_2O_3, Fe_3O_4 or $M_{23}C_6$ phases. The blue arrows correspond to the most intense peaks of the Y_2O_3 phase.

The presence of unknown phases has been checked finding traces of the TiN phase; also different Y-Ti-O stoichiometries have been checked ($Y_2Ti_2O_7$, Y_2TiO_5) but none of them could be reliably identified explaining the origin of the small peaks in the low angle region, which were detected also by SANS [3]. Additional metallurgical information is therefore necessary to characterize the minority phases present in the as-received state of such steels. Also the asymmetric dislocation broadening of the (200) line, with scarce size contribution from very small clusters, was recognized. A clear difference was detected among the different samples, which was found to be qualitatively consistent with the expected micro-structural evolution.

SANS measurements have been carried out on the 14 Cr ODS Y_2O_3 0.35 wt% ferritic martensitic steel samples (provided by KIT, Germany), in which the Ti contents was ranging from 0.2-0.4 wt%. A reference 14 Cr ODS sample, with no Ti, and three samples with respective Ti contents of 0.2, 0.3 and 0.4 wt% were investigated by SANS at the D22 instrument (ILL, Grenoble). Sample-to-detector distances of 2 m and 11 m were utilized with a neutron wavelength of 6 Å[1], giving an experimental range corresponding to particle sizes ranging between 10 and 300 Å in size approximately. A saturating magnetic field of 1 T was applied to separately measure the nuclear and magnetic SANS components. The SANS results are shown in Fig. 2, from which it is evident that adding Ti promotes the growth of a new population of microstructural defects, which are ~2.0 nm in average size, and that at the same time significant changes in SANS cross-section are detected also in the low *Q* region.

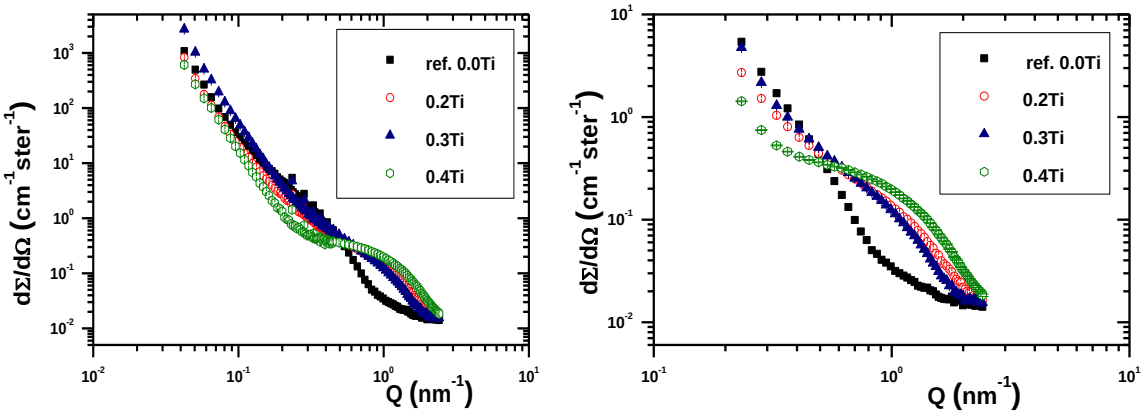

FIG. 2. Nuclear SANS cross-sections (cm^{-1} vs nm^{-1}) of 14 Cr ODS Y_2O_3 0.35 wt% ferritic – martensitic steel with different Ti contents: whole spectrum (left), 2 m sample-to-detector distance (right).

Based on the ratio of nuclear plus magnetic to magnetic SANS cross-sections (Fig. 3) as well as on TEM and APT results [4, 5], the smaller inhomogeneities can be tentatively identified as Y-Ti-O complexes, while the SANS variations observed at smaller Q values should be attributed to the evolution of large Cr carbides.

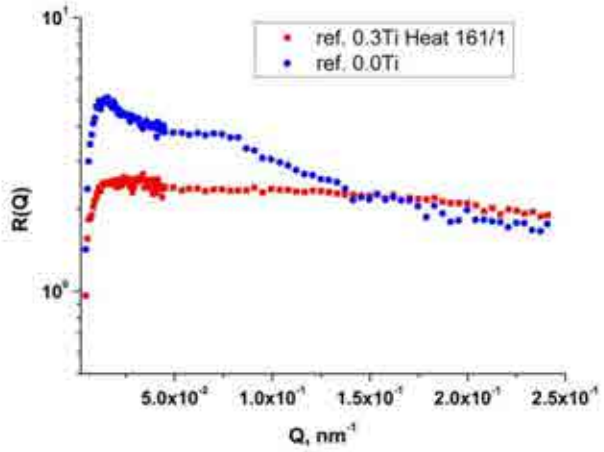

FIG. 3. Ratio of nuclear plus magnetic to magnetic SANS cross-sections for 14 Cr ODS with no Ti (upper curve) and 0.3 Ti (lover curve).

[1] 1 Å = 0.1 nm

Microstructural investigation of ODS ferritic steels

At Budapest Neutron Centre at the 10 MW research reactor a series of experiments using SANS technique were performed with ODS steel samples of different chemical compositions and after various heat treatments for the investigation of irradiation effects (in collaboration with JRC, The Netherlands).

In Ref. [6] SANS technique was used to investigate the phase separation in two (ODS) ferritic steels, PM2000 and MA956, during isothermal ageing at 475°C. The ferritic matrix of the investigated materials separates into Fe-rich α and Cr-rich α′ phases during ageing at this temperature. SANS is particularly powerful in the case of α′ phase separation because of the large difference between the neutron coherent scattering lengths of Fe ($9.45 \cdot 10^{-15}$ m) and Cr ($3.64 \cdot 10^{-15}$ m). The SANS experiments were performed on the Yellow Submarine instrument at ambient temperature. The samples used for the measurements were cut from the bars in the shape of plates of 1 mm thickness. The covering scattering vector range was from $4 \cdot 10^{-2}$ nm^{-1} to 2.5 nm^{-1}. The samples were placed into an external saturating magnetic field (~1.4 T) perpendicular to the incident neutron beam direction. The ratio of these two contributions was used to gain information on the chemical composition of the scatterers.

Figure 4 shows the magnetic and nuclear coherent scattering cross-sections of the as-received and the three aged states of the investigated material PM2000. A pronounced ageing-induced increase is found on the magnetic and nuclear scattering at scattering vectors $\langle Q \rangle$ 0.35 nm^{-1} and 0.40 nm^{-1} for PM2000 and MA956 respectively. Compared to the as-received material, additional small scatterers (with sizes below ~6–8 nm) can be observed in the aged samples.

It was concluded that the SANS measurements revealed the formation and subsequent growth of Cr-rich precipitates on the nanometer scale. The size distribution and the volume fraction of the precipitates were evaluated from the scattering data shown in (Fig. 5).

For PM2000 sample aged by 100 h some indications were found of the presence of other processes besides α′ formation during the early stages of the ageing. Micro-hardness was found to significantly increase as a function of ageing time for both materials. The hardening is related mainly to the formation of a Cr-rich α′ phase.

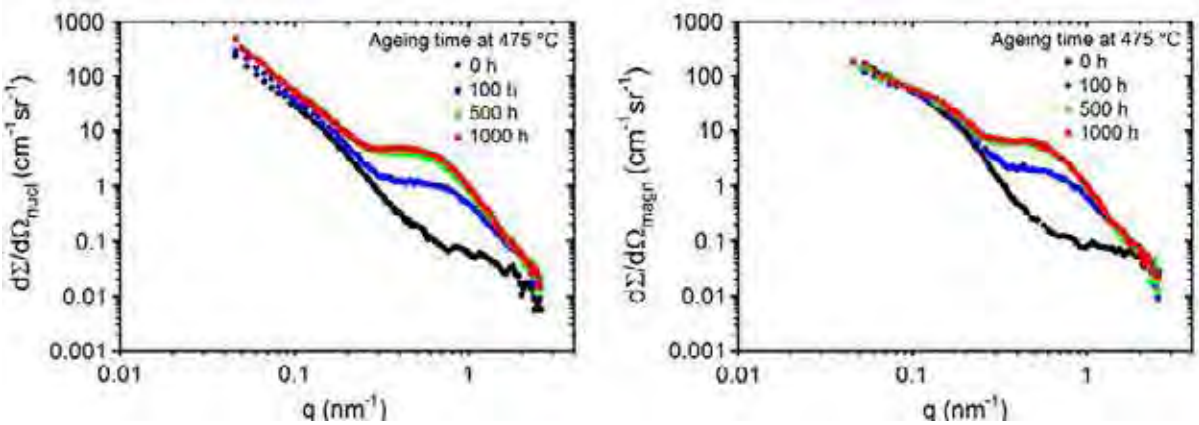

FIG. 4. Nuclear (left) and magnetic (right) SANS scattering cross-sections for PM2000 in as-received and three aged conditions.

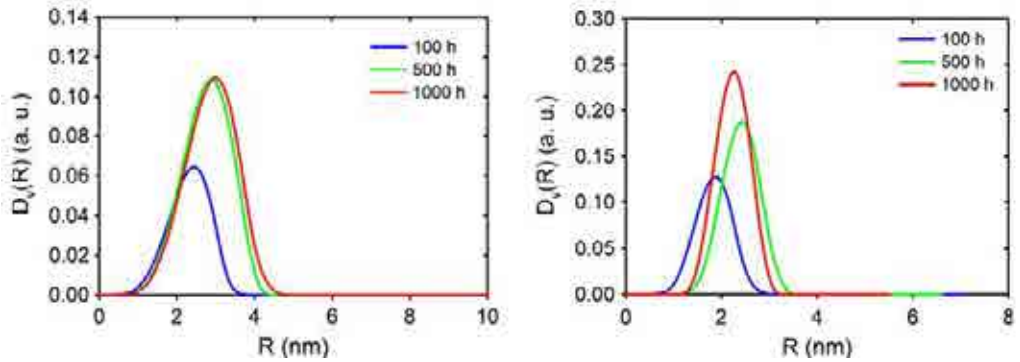

FIG. 5. Particle size distribution at three aged conditions in PM2000 (left) and MA956 (right).

Ferrite–martensite steels dispersion hardening studied by TOF neutron diffraction

Usually effects produced by any particular microstructure ("stress and size" effects) are rather small and, therefore, before investigation the micro-stress influence on the radiation resistance as well as modification of micro-stress under irradiation, it is necessary to clarify the capability of a neutron diffractometer for these purposes. For this not only a sufficiently high resolution in the minimum of the resolution curve is needed but its dependence on d_{hkl} (see Eq. (1)) must be well known. This can be done by measuring the diffraction patterns from a standard polycrystalline sample such as $Na_2Al_2Ca_3F_{14}$ (NAC) or some others (Al_2O_3 or LaB_6), recommended by the International Union of Crystallography for instrument calibration and definition of the resolution function with good accuracy. After that, using the obtained calibration parameters for further patterns processing from working samples by the help of the Rietveld method it was possible to obtain the precise lattice parameters, as well as the micro-strain and the average crystallite size.

The diffraction peak widths for two 40H4G18F steel samples, tempered at 600ºC and 700ºC, were measured with the HRPT diffractometer [7] operating with monochromatic beam at the SINQ neutron source in the Paul Scherrer Institute (Switzerland). These results are shown in Fig. 6 together with the instrument resolution function.

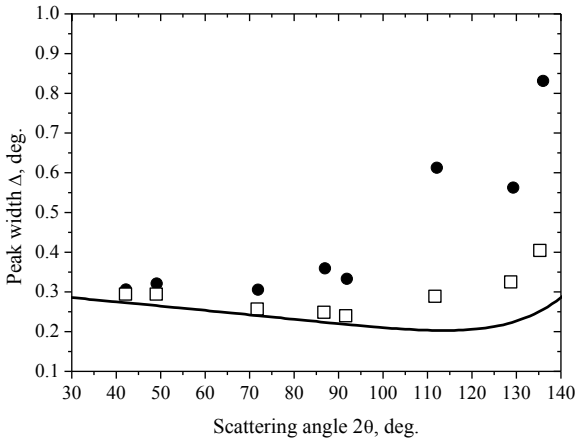

FIG. 6. Diffraction peak widths for two 40H4G18F steel samples tempered at 600ºC (squares) and 700ºC (circles) measured with HRPT at λ = 0.1494 nm in comparison with instrument resolution function (solid line).

One can see that with the HRPT diffractometer the diffraction peak broadening effects can be measured easily and with high accuracy. As it was discussed in the previous section for the W(d) dependence, anisotropic effects can be estimated, Williamson-Hall plot can be drawn and micro-strain and domain size may be calculated. The HRPT experimental practice shows that the peak broadening effects can be reliably detected for the micro-strain values $\varepsilon \geq 10^{-4}$ and for the average crystallite size of the $D \leq 200$ nm.

The Rietveld analysis realized with the advanced software packages such as FullProf [8] and GSAS [9] can also provide microstructure parameters, if resolution curve is known. For instance, in the study of cylindrical sample (∅ = 6 mm) made from the austenitic steels H16N15M3T1 with Ni_3Ti hardening phase, the neutron diffraction patterns were measured at room temperature for two wavelengths of the primary beam (λ = 0.1154 and 0.1494 nm). Processing of diffraction data by the Rietveld method (Fig. 7) provides estimations of the peak broadening due to lattice micro-strain and the average size of the coherent domains. It was found that the size effect contribution to the peak width is negligible, i.e. $D >> 200$ nm while micro-stresses contribute significantly.

Heat-resistant pipeline components (elements of steam and boiler superheaters, turbines, blades, etc.) of thermal power plants operating in the creep range at temperatures up to 650°C are often made from tempered ferrite-martensite steels with ~10 wt% chromium content. The heat treatment of tempered ferrite-martensite steels usually consists of two stages: austenization and tempering. Ferrite-martensite steels have a complex microstructure which consists of fine micro grains separated by different kinds of interfaces (austenite grain boundaries, block boundaries and twin boundaries) and carbides which are precipitated near these boundaries. Additionally, these steels exhibit a very high dislocation density after heat treatment, which are produced in the parent phase during the martensitic transformation. These new ferrite-martensite steels are of great interest for nuclear industry due to their unique heat- and radiation-resistant properties and evolution of their microstructure under various conditions is a subject for neutron scattering studies.

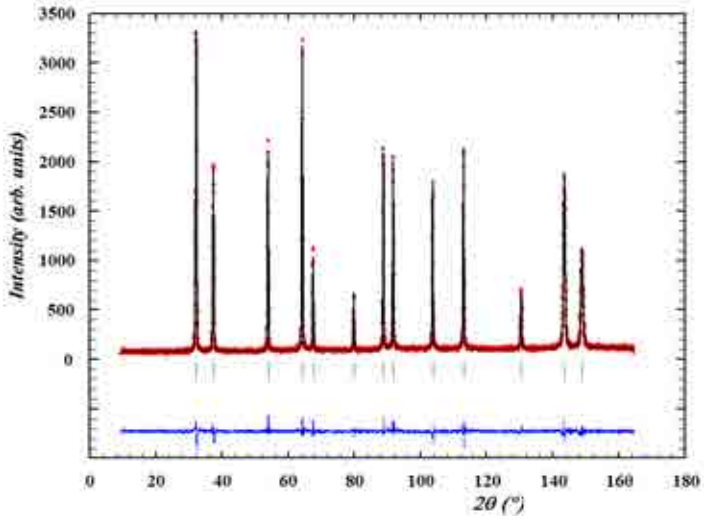

FIG. 7. A typical diffraction pattern from a steel sample measured with HRPT at λ = 0.11545 nm and processed by the Rietveld method. The experimental points, calculated profile (bottom) and peak positions (vertical bars) are shown as a function of scattering angle.

Finally, two newly heat-resistant ferrite-martensite steels 10H9K3V2MFBR and 10H9MFB (K3 and P91 hereinafter, developed in Russia) were investigated on the TOF diffractometer FSD at the IBR-2 pulsed reactor of JINR-Dubna in a wide range of tempering temperatures. The studied steels have the following chemical composition: K3 steel - 0.1%C, 9.36%Cr, 2.93%Co, 1.85%W, 0.45%Mo, 0.2%V, 0.05%Nb, 0.048%N, 0.005%B, the rest – Fe; P91 steel - 0.1%C, 9.36%Cr, 0.85-1.05%Mo, 0.2%V, 0.06-0.1%Nb, 0.25-0.5%Si, 0.3-0.6%Mn, the rest - Fe. The studied samples were normalized at 1050ºC and tempered for 3 hours at temperature of 750ºC [see contributed papers: Balagurov et al.].

Two series of experiments were performed. In a first measurement initially quenched K3 sample was heated *in situ* in the mirror furnace from room temperature to 600ºC. The diffraction data has been processed routinely by the Rietveld method and it was found that the temperature dependences of the lattice parameter and the Debye-Waller factor are linear. For instance, the linear thermal expansion coefficient of the material has a value $\alpha = (10.9 \pm 0.5)\cdot 10^{-6}$ K^{-1}, which is typical for this class of steels.

The observed diffraction peaks have significant broadening in comparison with reference sample (Fig. 8). In order to analyse peak broadening effects due to the crystal lattice micro-strain and finite size of coherently scattering crystallites the individual diffraction peaks were fitted. Detailed analysis of peak widths revealed anisotropic character of peak broadening at which some reflection deviate from linearity (especially for (200) and (310) peaks) and conventional Williamson-Hall analysis cannot be applied. This deviation is usually associated with the dislocation contrast factor variation, which has been mentioned repeatedly in the literature (see, for instance, in [10] and references therein) as well as observed previously in our neutron diffraction experiments. The observed anisotropic peak broadening effect is quite strong and can be readily registered due to good FSD resolution. For correct micro-strain evaluation the width anisotropy should be taken into account in the fitting procedure, which can be performed using the model proposed in [11] and illustrated in Fig. 9. The dislocation density behaviour during heat treatment for both studied steels is presented in Fig. 10. It can be clearly seen that main changes occur in the temperature interval from 500°C to 600°C where sharp decrease of dislocation density is observed. On the right: $(\Delta d)^2$ vs. $(d_{hkl})^2$ dependences for standard sample (lower curve, black points) and for the K3 ferrite-martensite steel sample tempered at 200°C (anisotropic broadening).

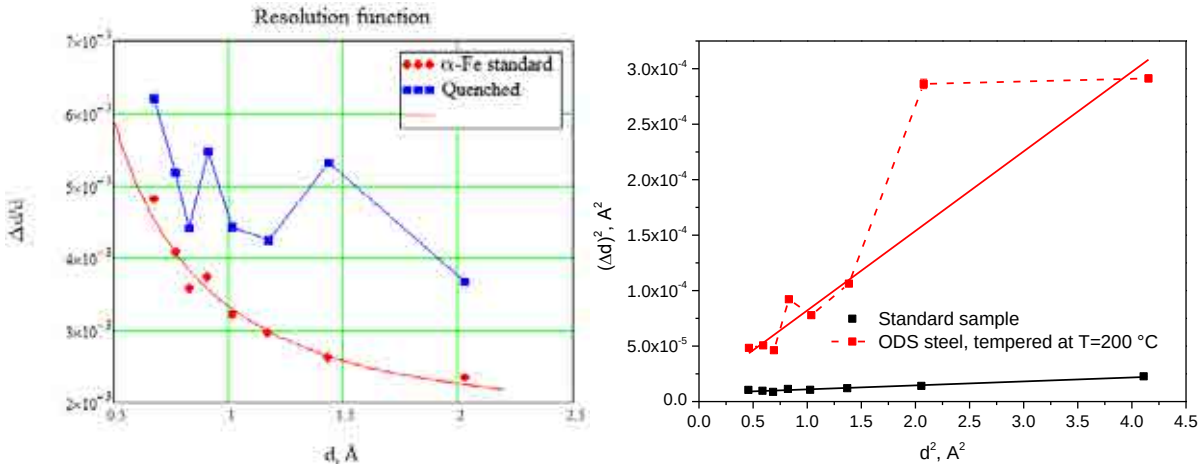

FIG. 8. Comparison of the diffraction peaks widths for a standard sample (lower curves) and for the K3 ferrite-martensite steel sample tempered at 200°C (upper curves).

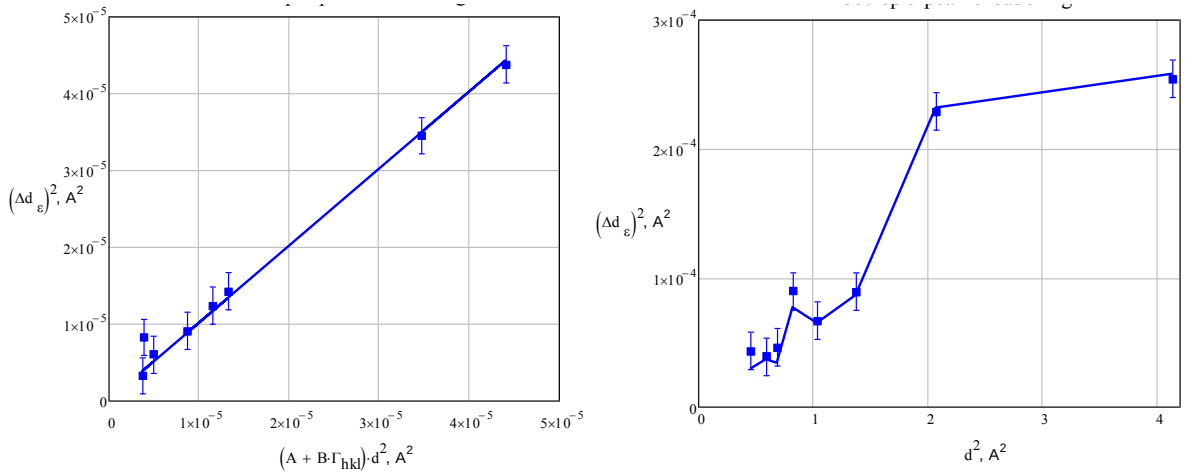

FIG. 9. Fitting of the tempered K3 ferrite-martensite steel sample anisotropic peak broadening: instead of d^2 the value $(A+B\cdot\Gamma_{hkl})\cdot d^2$ is used as a variable for $(\Delta d)^2$ dependence.

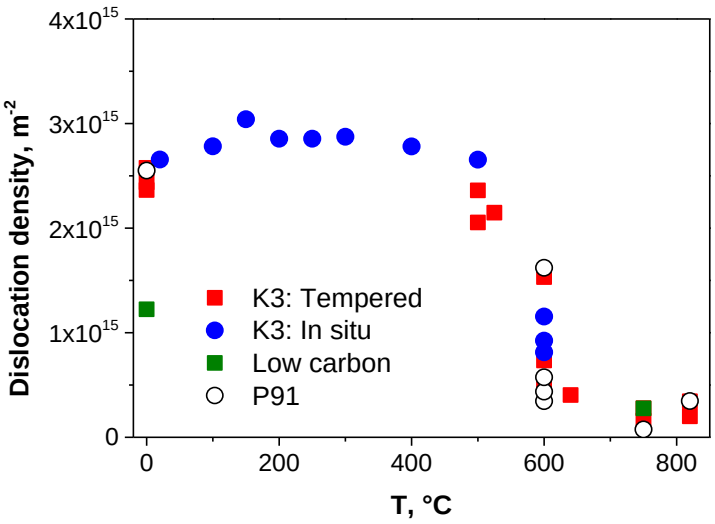

FIG. 10. Estimated dislocation density as a function tempering temperature for K3 and P91 studied steels.

In order to complete the neutron diffraction measurements, the heat-resistant 10H9MFB (P91) steel samples were investigated at the "Yellow Submarine" SANS instrument at the Budapest Neutron Center, Hungary. The measurements were performed with and without magnetic field and the SANS intensities were analysed by standard method, which helps to separate between nuclear and magnetic contributions. The nuclear contribution was fitted in order to evaluate main structural parameters of the studied systems (Fig. 11). According to the nuclear SANS data the nature of neutron scattering changes from surface fractals to the volume fractals, which also indicates the mass appearance of carbonitrides.

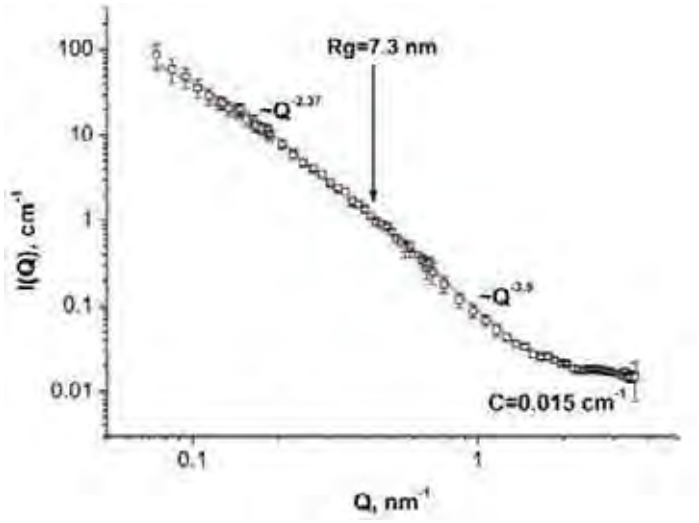

FIG. 11. Nuclear SANS data fit for the sample tempered at 600°C.

2.2. RESEARCH ON ZIRCONIUM BASED MATERIALS (INCLUDING HYDROGEN UPTAKE)

Zirconium alloys are widely used in nuclear installations as fuel, target rod cladding material as well as for pressure tubes. They show low corrosion rates in water or steam until temperatures of about 1000°C have a very low total neutron cross section and sufficient mechanical strength. Because of its anisotropic behaviour caused by the hexagonal crystal structure, various mechanical properties like strength or ultimate strain depends on texture. To ensure these properties for the application, the texture formation has to be defined by the thermo-mechanical treatment. For instance texture influences strongly the irradiation response of Zr-2.5Nb pressure tubes [11]. Serious problems of zirconium alloys are the hydrogen uptake during corrosion under operational conditions and during high temperature steam oxidation under accident conditions.

Neutron diffraction and imaging methods are very powerful to investigate zirconium alloys. In addition, the high penetration depth allows neutron diffraction from the bulk of real components like cladding or pressure tubes under different angles for deformation and texture analysis. Non-destructive inspections of fission fuel rod or spallation target cladding tubes are possible including inspection of the nuclear fuel itself. Finally, the high total neutron cross section of hydrogen allows the investigation of hydrogen related processes in components made from zirconium alloys.

In this part of the report, examples are given of the cooperative research in the fields of deformation and texture analysis of components made from zirconium alloys. Different aspects of hydrogen in zirconium as well as the inspection of nuclear fuel rods and highly irradiated components are described.

2.2.1. Deformation and texture in components made from zirconium alloys

Neutron diffraction has been applied to study the deformation behaviour and irradiation responses of zirconium alloys. The investigation of the evolution of the microstructure of zirconium during thermo-mechanical and annealing treatments as well as irradiation was a key point of the cooperation in this CRP. Five partners, namely CNEA, LANL, JINR, ANSTO and CIAE took part in these investigations.

Phase composition and strain

At CNEA, the phase compositions in Zr2.5Nb pressure tubes after three manufacturing stages were determined by analysis of the neutron diffraction patterns illustrated in Fig. 12. The main differences are in the minority phases. From the lattice constant of the β-zirconium phase, the niobium concentrations in this phase were estimated. Differences between the manufacturing states were found. Whereas for the extruded and cold-rolled specimens the β-phase contains 23% niobium, it decomposes after the heat treatment into a β-phase with 40% niobium and the β-zirconium phase.

At JINR residual stress in end plugs of VVER fuel elements made of E110 (Zr1Nb) were determined. Residual tensile stress of about 150 MPa along the radial direction were found in the original plug, which was nearly completely relieved by a heat treatment.

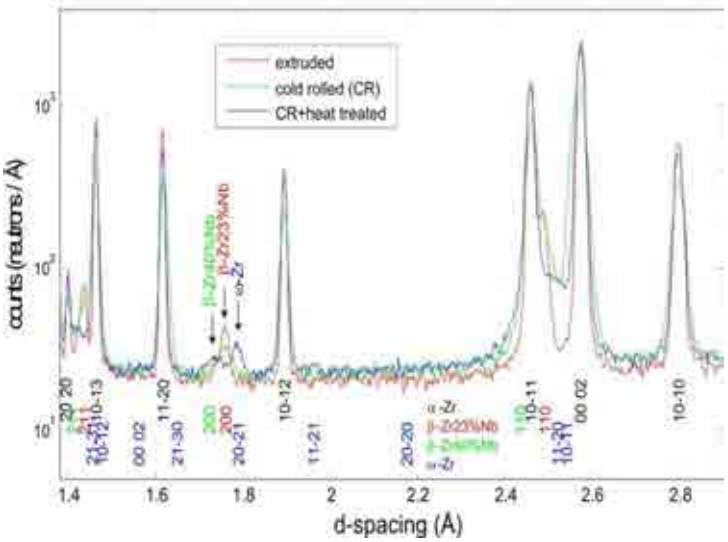

FIG. 12. Bulk diffractograms for specimens from the different manufacturing stages (red: extruded, green cold rolled, blue cold rolled + annealed).

Texture of zirconium components

As mentioned before, the crystallographic texture of the zirconium alloy plays an important role to ensure the properties need for the application as nuclear fuel cladding, guide or pressure tubes. In hexagonal materials, the Kearns texture factor [12] is another widely used method for quantifying texture information. This factor is a quantification of the volume fractions of crystallites with (typically) basal poles aligned along any single sample direction,

$$f_z = \int_0^{\frac{\pi}{2}} I_{(0002)}(\varphi) \sin\varphi \cos^2\varphi \, d\varphi \qquad (8)$$

where z is the direction of interest, and $I_{(0002)}(\varphi)\sin\varphi$ is the fraction of crystals having their c-axis at an angle φ from that direction.

At CNEA the texture development in Zr2.5%Nb pressure tubes after various manufacturing steps was investigated. The neutron diffraction experiments were performed using the ENGIN-X facility at ISIS (UK). Goal of the investigations was the validation of a new cold rolling manufacturing stage as a part of the manufacturing of 380 Zr2.5%Nb pressure tubes to be replaced during the refurbishment of Embalse Nuclear Power Plant, Argentina.

Preferred lattice orientations are produced by the thermo-mechanical treatment of the material. The development of the orientations of the $(1\,0\,\bar{1}\,0)$, (0001) and $(1\,0\,\bar{1}\,1)$ lattice planes after different steps of the production process were measured. Figure 13 gives these pole figures. Subtle changes in the number of crystals having *c*-axis lying in the hoop-radial plane of the tubes were resolved by the experiments. Such variations were quantified in terms of the orientation distribution functions of crystallites (ODF), and by Kearns factors, the operational variable used in manufacturing.

Cold rolling produces a drop of ~30% in the number of crystals with *c*-axes along the hoop direction (φ=90°), and an increase in those with *c*-axis at angles φ<60°. The heat treatment partially reverses this effect.

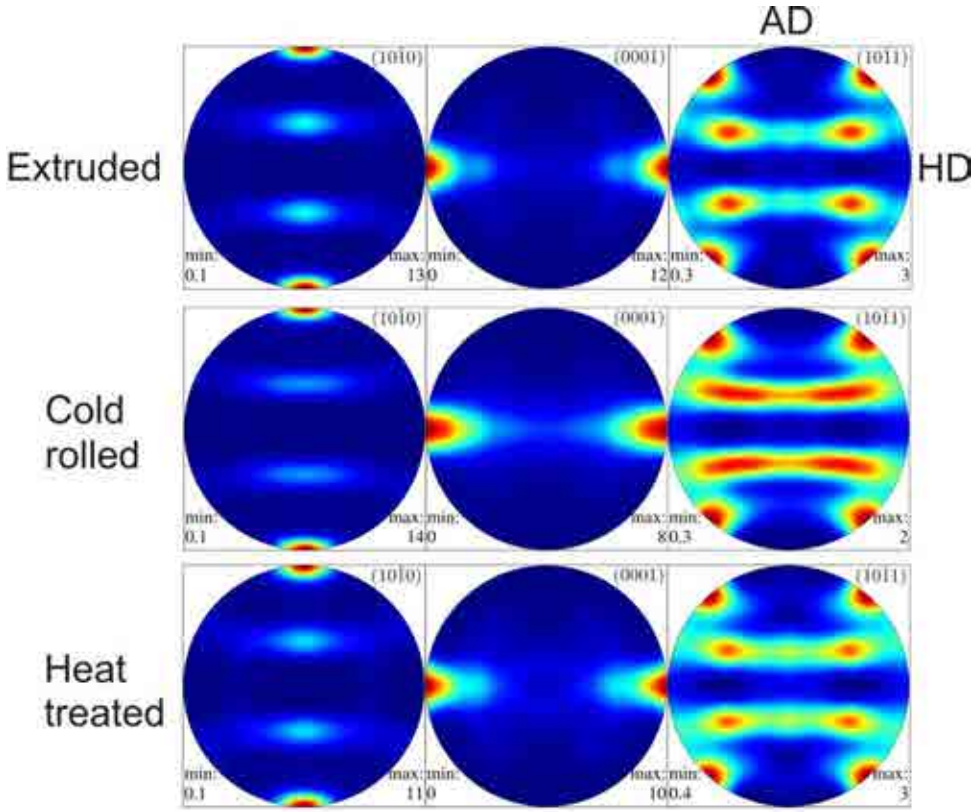

FIG. 13. Recalculated pole figures of the Zr2.5%Nb specimens after extrusion, cold rolling and cold rolling + annealing.

Details about the experiments including a quantitative analysis of the texture are given in the contributed paper by Santisteban** et al.

The reproducibility of the results of texture measurements were studied in a dedicated Round Robin test in the framework of this CRP. CNEA, LANL, JINR, ANSTO and CIAE took part in these investigations. The textures in Zircaloy-4 (Zry-4) specimens and Zr2.5%Nb specimens were measured. Experiments on the Zr2.5%Nb specimens have been performed on the SKAT (IBR-2, JINR, Russia), the Kowari (OPAL, ANSTO, Australia) and the ENGIN-X (ISIS, STFC, UK).

Recalculated pole figures are given in Fig. 14. For texture measurements of the Zry-4 specimen the HIPPO (LANSCE, LANL, USA), the texture diffractometer at CARR (CIAE,

China) and the Kowari (OPAL, ANSTO, Australia) were applied. The pole figures are compared in Fig. 15.

Overall, good agreement was found both qualitatively and quantitatively among the pole figures obtained for the two materials at the different neutron diffractometers.

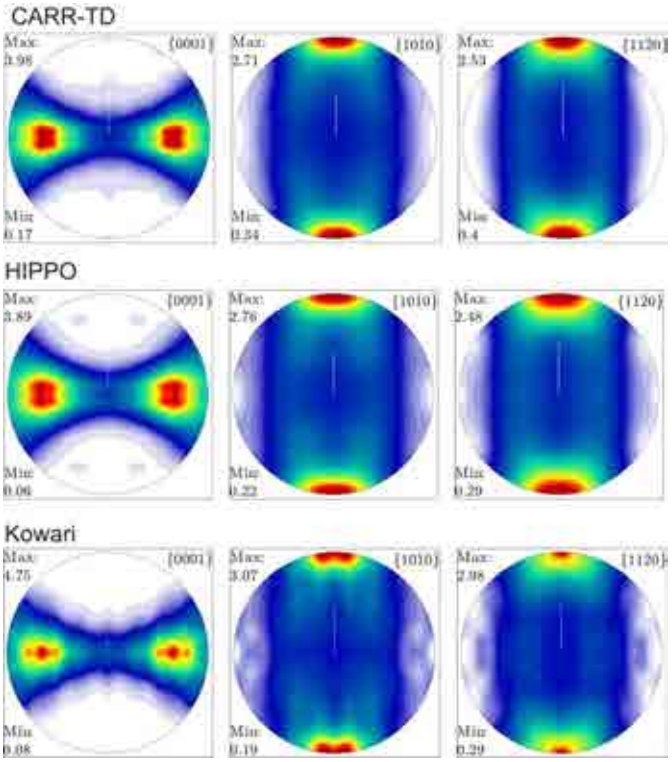

FIG. 14. Recalculated pole figures for the Zry-4 specimen.

All Kearns factors are within an uncertainty of 0.02, which is lower than typical differences usually found between different batches, or between the start and end of pressure tubes. This is deemed very satisfactory, and can be compared with a variation of ~0.06 reported in a 14-participants Round Robin Zircaloy-4 texture measured by X ray diffraction [13]. The Kearns factors measured for the transverse, normal and rolling directions of the Zry-4 plate are comparable to the values reported in that work for stress-relieved Zry-4 fuel cladding of 0.635 mm wall thickness. On the other hand, the Kearns factors measured for the Zr2.5%Nb pressure tube compare well with values obtained by X ray diffraction. So, the 0.02 uncertainty found between laboratories is small compared to conventional X ray diffraction. This is very likely because of the much larger volume of material gauged by neutron instruments. Variations in texture indices were larger than for Kearns factors, particularly for the Zr2.5%Nb pressure tubes. Indeed, the sharpness of this texture makes the ODF determination much more sensitive to the exact gridding used in the experiments.

The differences between the two materials are caused by the different thermo-mechanical treatments. The Zry-4 plate was warm-rolled. The Zr2.5%Nb set was made from billets forged at ~800°C, the fabrication route of this pressure tubes included extrusion at ~800°C, followed by cold rolling to ~28% strain, and autoclaving at 400°C for 24 h.

It is interesting to mention that satisfactory results were obtained from the residual stress diffractometers (ENGIN-X and Kowari), although these instruments are not optimized for this purpose. This opens the possibility of exploiting the spatial resolution of some mm^3 provided

by such instruments to precisely quantify the characteristic texture variation found in zirconium alloys welds.

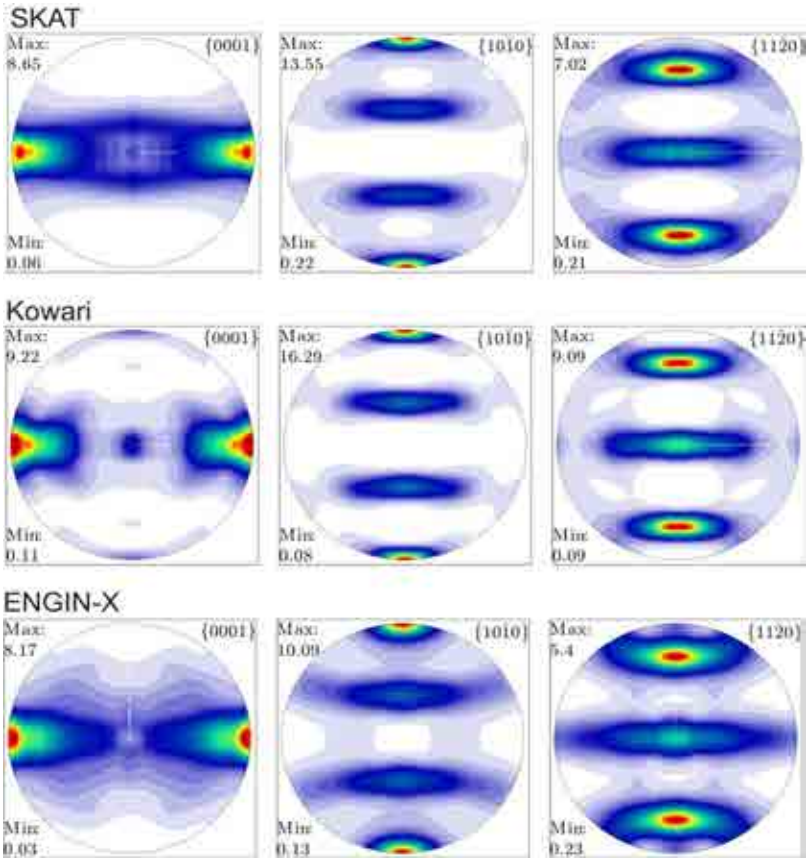

FIG. 15. Recalculated pole figures for the Zr2.5Nb specimens.

From the results reported one concludes that the crystallographic texture of specimens made of zirconium alloys can be precisely quantified in a variety of neutrons instruments worldwide with small efforts in preparing and sharing specific samples. A preliminary Round Robin exercise using specimens made of Zr2.5%Nb and Zry-4 was successful, and demonstrated that operational parameters such as Kearns factors are defined with a typical uncertainty of ±0.02.

More information about the materials, the facilities taking part at the Round Robin and about the texture analysis procedures are given in the contributed paper by Santisteban* et al.

Aditionally, the texture in end plugs of VVER fuel elements made of E110 (Zr1%Nb) was measured by neutron diffraction. The experiments were performed at IBR-2 and HZB in cooperation with NECSA on an original plug before and after an annealing treatment, consisting of 2 h in vacuum (10^{-3} Pa) at 600°C. A fibre texture was found in both cases. However, considerable changes to the original texture were introduced by the heat treatment.

Deformation studies

The analysis of the Bragg peak shape provides information about dislocations and with it about the deformation of the material [see contributed papers: Santisteban** et al. and Bourke].

Current deformation studies were performed at LANL on Zr2.5%Nb pressure tube samples which had been in service for 7 years at an operating temperature of ~250°C and had

experienced a moderate fast neutron fluence of 1.6×10^{24} m^{-2} (E > 1 MeV), and on an un-irradiated control sample. An advanced line profile analysis (DLPA) was used to measure the dislocation densities within the *α*-Zr phase, differentiating between <*a*>-type, <*c*>-type and <*a*+*c*> type dislocations. Distinct differences in dislocation types introduced by plastic deformation were found between the irradiated and non-irradiated materials. Fast neutron irradiation resulted in a fourfold increase in overall dislocation density entirely due to an increase in <*a*>-type dislocations, together with a profound change in the dislocation network arrangement. The results were already published in [14].

CNEA studied the evolution of the dislocation densities during three manufacturing stages. The dependence of the intrinsic Bragg line width ΔK (from the sample related physical line broadening) on the reciprocal inner planar distance $K = 1/d$ is plotted in Fig. 16. From the slope of the curves the dislocation density can be determined. For the anisotropic distribution of dislocations in hexagonal close-packed Zr, this equation can be modified to calculate the type-*a* and type-*c* component dislocations (see the red data points in Fig. 5). It can be seen that the dislocation density increases by cold rolling and decreases again after the heat treatment. The determined dislocation densities are within the values expected for this material for these micro-structural conditions. The values of the dislocation densities found after the final heat treat lie within the specifications for the final product [see contributed papers: Santisteban** et al.].

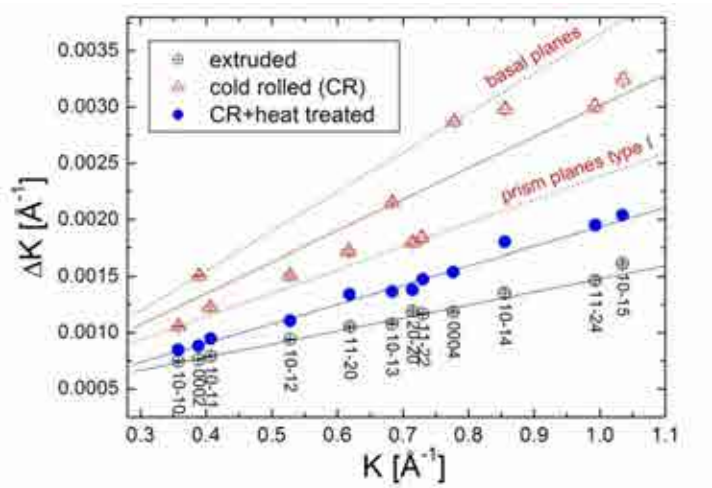

FIG. 16. Williamson-Hall plot of the physical peak broadening measured for the three samples.

2.2.2. Hydrogen in zirconium

As mentioned before, the absorption of hydrogen results in a degradation of the mechanical properties of zirconium alloys. The material loses its toughness which may lead to brittle fracture of the fuel or spallation target cladding with the consequence of fission gas release and fuel relocation. The hydrogen uptake occurs during corrosion in water or high temperature oxidation in steam. In a simplified representation the reaction can be described by:

$$Zr + 2\,H_2O = ZrO_2 + 2x\,H_2 + (4\text{-}2x)\,H_{absorbed} \qquad (9)$$

The free hydrogen produced by the oxidation can be released into the environment with the risk of a hydrogen detonation as happened during the Fukushima Daiichi accident in Japan or can be absorbed by the remaining metallic zirconium.

Neutron imaging methods are very powerful to investigate hydrogen in zirconium. The total microscopic neutron cross sections of the two elements strongly differ. In addition, the total macroscopic neutron cross section of hydrogenated zirconium depends linearly on the number density of hydrogen atoms and, therefore, on the hydrogen to zirconium atomic ratio as demonstrated contributed paper by Lehmann et al. As shown in Ref. [15], the value of the total macroscopic neutron cross section corresponds with the CT (computed tomography) number of neutron imaging too.

Neutron radiography and tomography were applied to study:

- Hydrogen redistribution in mechanically stressed zirconium samples in the framework of investigations of the delayed hydride cracking (DHC);
- Hydrogen distribution in cladding tubes after loss of coolant accidents;
- Additionally, the hydrogen precipitation was investigated by means of small angle neutron scattering (SANS).

Hydrogen uptake and redistribution in mechanically stressed Zircaloy-4 samples

Because the chemical potential of hydrogen in lattice regions under tensile stress is lower than in the stress-free lattice, hydrogen is enriched in the stress field ahead of a crack tip. It weakens the material with the consequence that the crack grows. This process is accompanied with a stress relief at the former crack tip position and a shift of the stress field to the new crack tip position. The hydrogen follows the position changes of the crack tip. Fracture is the consequence even under subcritical load. The phenomenon is known as delayed hydride cracking (DHC). PSI, CNEA and KIT cooperated in the field of in-situ measurements of the hydrogen uptake and redistribution in mechanically stressed Zry-4 specimens. The experiments are related to the delayed hydride cracking research at PSI. The problem of ex-situ investigations is that the hydrogen solubility between the temperatures at which DHC occurs is much higher than at room temperature. A cool-down to room temperature changes the hydride concentration and distribution in the crack region. Therefore, not all information needed to understand DHC are provided by ex-situ investigations.

In-situ investigations are very difficult because a method is needed providing information about the distribution of hydrogen absorbed in the zirconium lattice and precipitated as hydrides at temperatures between 250°C and 400°C with a spatial resolution of some tens of microns. Neutron radiography seems to be the only method suitable to study in-situ the occurring processes.

First experiments were performed using the INRRO furnace (in-situ neutron radiography reaction oven) of KIT at the ICON facility at the Swiss neutron source SINQ at PSI. The samples were mechanically loaded in the furnace by a special device keeping the sample at a constant strain which was constructed by PSI. As an example of the results Fig. 17 gives the hydrogen distribution in the image sequence of the notch and crack tip region of a specimen under yield stress illuminated at different times. In the first 14500 s no hydrogen uptake occurred followed by rapid hydrogen absorption through the notch surface. After the hydrogen supply was switched off, a very slow redistribution occurs. This shows that the chemical potential of hydrogen in zirconium strongly depends on the zirconium lattice strain [see contributed papers: Grosse* et al]. The DHC could not be studied directly yet. However, the cooperation between PSI, KIT and CNEA to investigate DHC will be continued. A more

sophisticated device for mechanical loading allowing controlling not only the strain but the stress too will be constructed.

First results of the investigations were presented on the following events: the 17th International QUENCH Workshop, Karlsruhe in November 20-22, 2011, the 18th International QUENCH Workshop, Karlsruhe, November 20-22, 2012, the MRS Fall Meeting & Exhibit, November 25-30, 2012 in Boston, Massachusetts and the 17th International ASTM Symposium on Zirconium in the Nuclear Industry in February 3-7, 2013, Hyderabad, India.

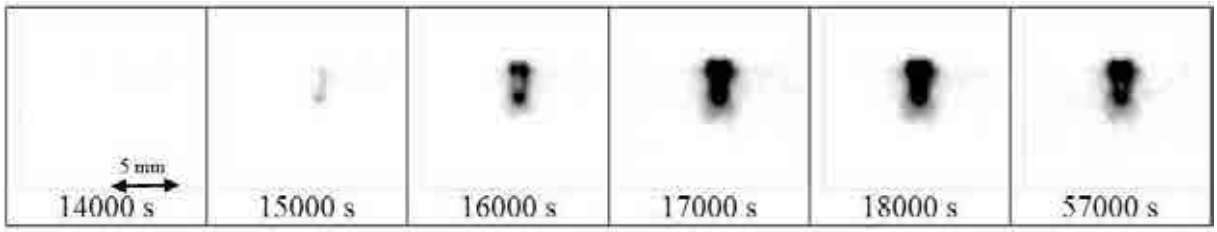

FIG. 17. Neutron radiograph sequence taken during hydrogen loading in Ar/H_2 atmosphere until 18,000 s and inert annealing of a mechanical stressed specimen until 57,000 s at 350°C.

Hydrogen distribution in claddings after loss off coolant accidents

The so-called secondary hydrogenation of nuclear fuel cladding during design basis loss of coolant accidents (LOCA) came into the focus of the licensing authorities after analysis of various single rod experiments. For instance the German licensing rules were changed in November 2012. It has to be proven for licensing of German nuclear reactors that during LOCA not only the cladding oxidation keeps below a certain degree (ECR < 17%) but also the hydrogen uptake does not result in a serious degradation of the mechanical properties. The hydrogen related embrittlement can result in reduced thermo-shock stability and with it in a reduced coolability of the reactor core during LOCA. In order to prove the coolability of German nuclear reactors the QUENCH-LOCA programme was initiated. Up to now three of these large-scale tests were performed. The post-test examinations of the first two tests are already finished.

The hydrogen distribution in claddings from QUENCH-LOCA simulation tests was investigated in cooperation between KIT and PSI. In inner rods of the QUENCH-LOCA bundle hydrogen enrichments were found. The hydrogen is concentrated directly at the burst opening, or bended bands not oriented perpendicular to the tube axis are seen as darker regions in the neutron radiograph (Fig. 18). For quantitative analysis of the hydrogen concentrations radiography experiments are not sufficient because the cladding tube thickness in the ballooning and burst region is not well defined. This thickness is needed to calculate total macroscopic cross sections from neutron transmission. Therefore, neutron tomography investigations at selected cladding tube segments were performed. As mentioned before, the CT numbers of the voxels are correlated to the total macroscopic neutron cross section and with it with the hydrogen concentration. Hydrogen concentrations up to 2600 ppm were determined by means of neutron tomography for the inner rods of the simulation bundle. In the peripheral rods of the bundle barely any hydrogen enrichments were found. The reason is the about 50°C lower temperature of the peripheral rods compared to the inner rods. This gives an important hint on a critical temperature below no hydrogen enrichments were formed [see contributed paper by Grosse** et al]. Results were published in [15, 16] as well as presented by M. Grosse et al. at the International Conference on Advances in Nuclear Power Plants (ICAPP 2012), Chicago (USA) (June 24-28, 2012) on “Analysis of the absorbed hydrogen in cladding tubes applied in the

QUENCH-LOCA tests“ and at the 17th International ASTM Symposium on Zirconium in the Nuclear Industry in February 3-7, 2013 in Hyderabad, India on “Analysis of the Secondary Cladding Hydrogenation during QUENCH-LOCA Tests and its Influence on the Cladding Embrittlement“.

The investigations will be continued. In the framework of the post-test examinations of the third QUENCH-LOCA experiment first neutron radiography investigations were performed in November 2013 and will be reported elsewhere.

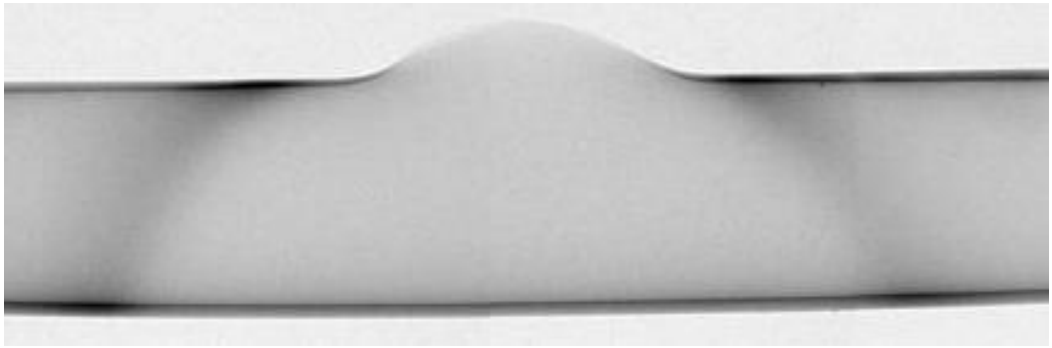

FIG. 18. Neutron radiograph measured at the ICON facility at PSI of the cladding of the fuel rod simulator QUENCH-L0 #03; the darker regions are hydrogen enriched.

SANS investigations of hydride precipitates in zirconium alloys

In the framework of the post-test examinations of the QUENCH-LOCA cladding tubes, XRD investigation were performed at the hydrogen enriched regions. In the diffraction patterns no hint of zirconium hydrides were found but a shift of the zirconium Bragg peaks to lower angles was observed. These results gave hints that hydrogen maybe in super-cooled solution in the zirconium lattice, rather than fully precipitated as a hydride phase. This finding inspired the study of the precipitation behaviour of hydrogen in zirconium alloys. On the other hand, transmission electron microscopy (TEM) investigations at the Zr2.5%Nb alloy gave hints that the hydrides seen in the optical microscope consist of smaller precipitations. By optical microscopy rod-shaped hydrides with a thickness of 1–2 µm and a length of 15–25 µm were found. Therefore, SANS experiments seem to be well suited to study hydride precipitates in zirconium alloys at least if the hydrides are small. The contrast between hydrogen and zirconium is very strong as mentioned before. In contrast to TEM, integral information is provided by SANS which make the results statistically much more reliable than TEM results obtained at a single precipitate or a couple of hydrides.

The investigations were performed by means of SANS in Cooperation between ENEA, CNEA, KIT and CEA. Measurements were performed at the D22 facility at ILL Grenoble, the PAXY facility at LLB Saclay and the SANS facility at FRM2 in Garching (TU Munich).

Figure 19 compares the 2D SANS pattern of hydrogen loaded and hydrogen free specimens made of Zr2.5%Nb alloy and Zry-4 (Zr1.5Sn). The two materials were measured with different experimental setups. However, some interesting differences are clearly visible. Comparing the measurements of two hydrogen free samples, strong anisotropic scattering was found for the Zr2.5%Nb alloy whereas the scattering of the Zry-4 sample is isotropic. The reason for the anisotropy seems to be the β-Zr phase covering the grain boundaries of the strongly elongated α-Zr grains (rolling grain structure). This β-phase contains a larger concentration of niobium than the α-phase which results in a scattering contrast. The strongly

elongated parallel oriented grains resulting from the thermo-mechanical treatment gives the anisotropic scattering. On the other hand, Zry-4 does not contain a significant amount of β-phase and the tin is distributed homogeneously. Although the grain structure is similar to the Zr2.5%Nb alloy, no strong scattering contrast exists at the α-Zr grain boundaries. Therefore, the grain structure does not result in an anisotropic scattering pattern. The hydrogen uptake results in a significant, more or less isotropic increase of SANS intensity. An analysis of the data shows that the SANS intensities depend on the scattering vector Q by a power law which gives hints that the size of the hydrides is large. Additionally, the annealing behaviour of the hydrides was investigated. The results show that the precipitation process was already finished during the cool-down phase from 1373 K to about 350 K within about 300 s [see contributed papers: Coppola et al. and Grosse*** et al.]. The results are part of a Bachelor thesis and were reported in [17].

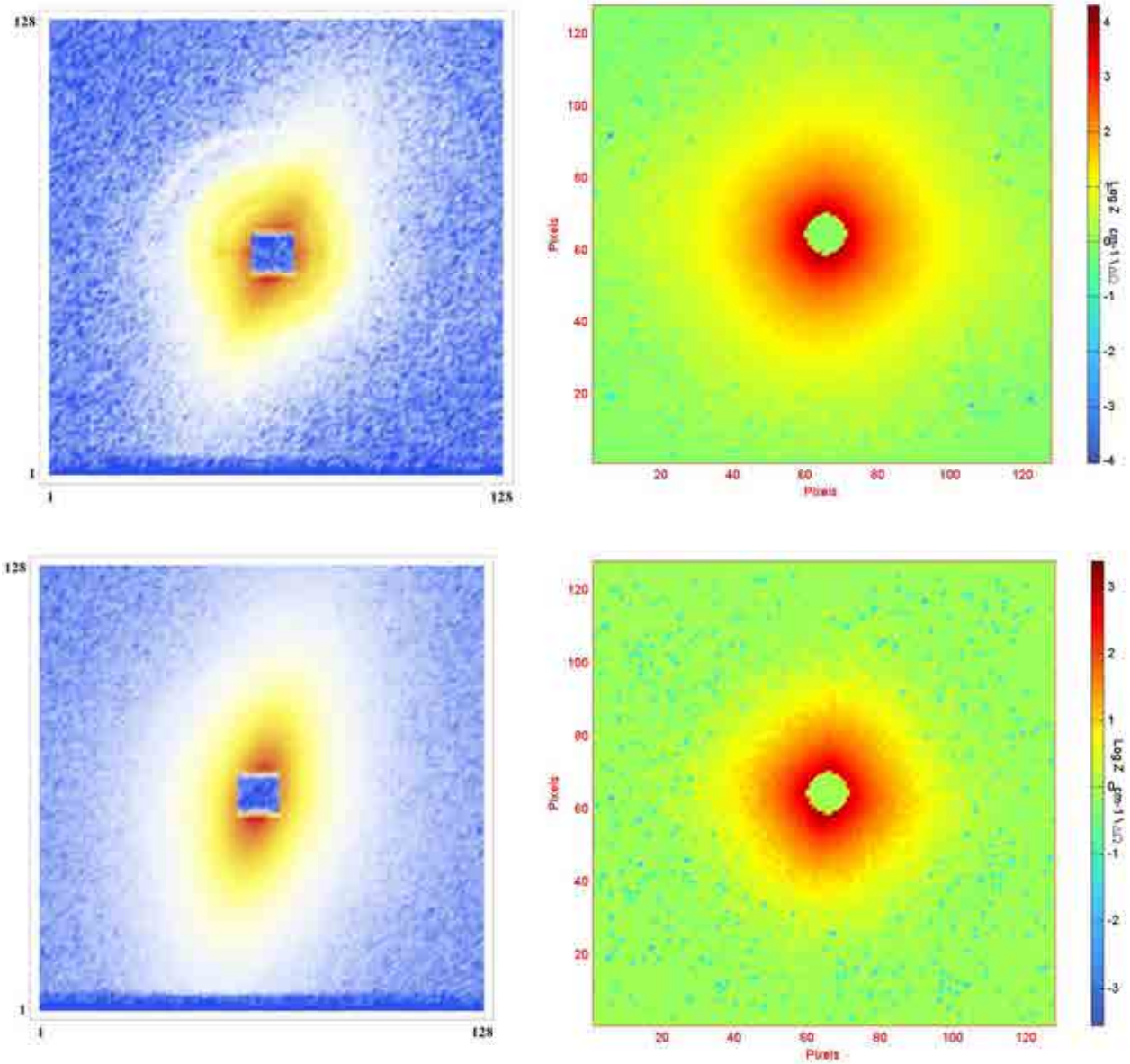

FIG. 19. Comparison of the 2D SANS patterns of hydrogen loaded (top) and hydrogen free (bottom) Zr2.5Nb (on the left from CNEA) and Zry-4 or Zr1.5Sn (on the right from KIT) alloys measured at the D22 facility at ILL Grenoble and the SANS facility at FRM2 in Garching (TU Munich) respectively.

A continuation of the SANS investigations is planned. In order to reach smaller precipitates faster water quenching of the specimens shall be applied.

2.3. INVESTIGATIONS OF WELDED STRUCTURES AND OBJECTS

More than ¾ of all component failure occur at subcritical external load. It means that the external load is smaller than the component strength. Reasons for this can be for instance the following processes occurring in the materials:

- Ageing;
- Fatigue;
- Embrittlement;
- Residual stresses.

Due to the very high safety requirements of nuclear facilities, material failures have to be excluded. Therefore, the residual stresses in the components have to be known to ensure safe behaviour during operation and under transient conditions. Residual stresses can occur during a lot of thermo-mechanical manufacturing processes but also during joining of components or usage. In particular during welding the formation of residual stresses cannot be excluded because of the temperature differences of the weld metal, the heat affected zone and the bulk material of the components.

Neutron diffraction is a powerful tool to determine residual stress and strain in components. In contrast to the classical X ray diffraction, thanks to the high neutron penetration depth, it is possible to measure residual strain in various directions of a sample. Classical X ray diffraction allows only to measure stains in near surface regions by the $\sin^2\psi$ method. High energy X ray diffraction available at some synchrotron facilities has free path length in structural materials comparable to neutrons. However, because of the very small Bragg angles at high energies the gauge volume is strongly distorted and the penetration depths keep low. This section covers principles of elastic strain measurements by means of neutron diffraction and the determination of the stresses from the strain measured in the mean directions, residual strain/stress measurements at components related to nuclear applications and SANS and ND investigations of nickel base super-alloys and stainless steels.

2.3.1. Residual strains/stress measurements in the vicinity of welds

Principles of the neutron diffraction method of residual strain/stress measurements

The principle of the neutron diffraction method is well known [18]. It consists of the precise determination of the d_{hkl}-spacing of particularly oriented crystal planes. Knowing the strain-free lattice spacing $d_{0,hkl,}$, the lattice strain ε_{hkl} can be calculated according to Eqs. (2a and 2b).

In general, the measured quantity in the diffraction experiment is the lattice strain component. For determination of the stress tensor components, Hooke's law can be used. For diffraction experiments, this formula for σ_x stress component can be written in the form:

$$\sigma_x = \frac{E_{hkl}}{(1-2\nu_{hkl})(1+\nu_{hkl})}\left[(1-\nu_{hkl})\varepsilon_x^{hkl} + \nu_{hkl}(\varepsilon_y^{hkl} + \varepsilon_z^{hkl})\right] , \qquad (10)$$

where $\varepsilon_{x,y,z}^{hkl}$ is the *x,y,z*-component of the lattice strain measured at the *hkl* crystal lattice plane, E_{hkl} and ν_{hkl} are the diffraction elastic Young modulus and diffraction Poisson ratio respectively. The $\varepsilon_{x,y,z}^{hkl}$ lattice strain components are determined in the neutron diffraction experiment. Corresponding relations for other *y* and *z* stress components are obtained by simple permutations of *x, z* and *y* indices.

The gauge volume can be defined by a slit system. The slits limiting the primary beam usual define two dimensions and the slit or the opening of a radial collimator before the detector the third dimension of the gauge volume. In order to obtain a nearly cubic volume, a scattering angle of about 90° is needed. Gauge volumes of several mm^3 are usually applied for neutronographic strain measurements.

Neutron diffraction mapping of internal residual stresses around weld joint of austenitic stainless steel plates

Three austenitic stainless steel plates with a longitudinal weld joint were examined. The selected material usually is employed for reactor vessel construction. The plates were marked as "sample 1", "sample 2" and "sample 3". The photograph of one specimen and introduction of the system of coordinates is shown in Fig. 20 and Fig. 21 respectively.

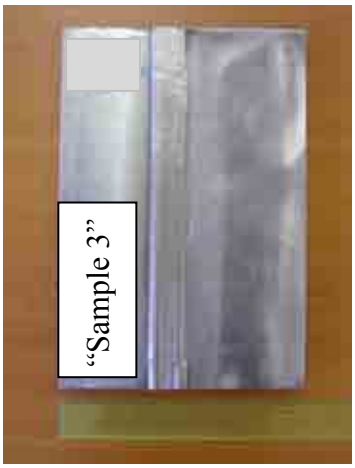

FIG. 20. Photograph of the sample 3 welded plate and chosen system of coordinates (compatible with coordinate system represented in Fig. 21).

For the neutron diffraction experiment the austenite reflection 111 was measured with two neutron wavelengths. Because of the rather substantial thickness of the plates varying from 24-29 mm, the measurement of the strain components *x* and *y* had to be performed with a lower diffraction angle ($2\theta = 44^o$). In the case of measured *x,y*-strain components, the neutron beam carrying the desired information is passing through the plate thickness (see Fig. 21). In the case of the recommended diffraction angles $2\theta = 90^o$, the neutron beam path through the plate is too long and the transmitted neutron intensity is attenuated due to absorption. In this case, the diffraction arrangement with $2\theta = 44^o$ and corresponding neutron wavelength of $\lambda = 0.15$ nm was used to overcome the above mentioned problem. The *z*-strain components was measured with the diffraction angle of $2\theta = 69^o$ and the neutron wavelength of $\lambda = 0.23$ nm.

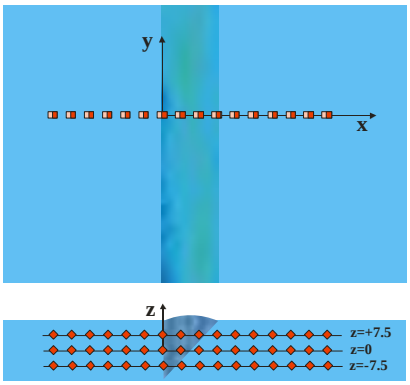

FIG. 21. The system of coordinates used for measurement of internal stresses around the weld joint in different depths. Red squares show the inspected gauge volume.

Two Cd-slits of 3 × 3 mm^2 and 3 × 40 mm^2 in incident and diffracted beam, respectively, were used for definition of the gauge volume. Resulting information on internal stresses was thus averaged over the volume of 27 mm^3. In the case of the present tested welded materials, the chemical composition of the used weld material is different from the base austenitic steel and, consequently, the stress-free lattice parameter of the weld material is different from base material of welded parts. To avoid the misinterpretation of the observed different lattice parameter in base and weld material, respectively, as a lattice strain, we have to perform a calibration and correction measurement. For this purpose, the special correction specimen was produced from each welded plate. The thin slices of 2.5-4 mm thickness were cut from the end face of the welded plates. These slices were further cut to release the internal residual stresses. For calculation of the stress tensors the values of diffraction elastic constants for austenitic steel were found in literature (E_{111}= 248 GPa, ν_{111}=0.24). The resulting *x,y,z* stress components are plotted in Figs. 22-24.

All examined plates exhibit similar distribution of residual stresses around the weld joint. The maximum stress level has been found in the case of the σ_y stress component; the tensile stresses of the maximum amplitude from 300 MPa (plates "sample 1" and "sample 2") to 500 MPa (plate sample 3) were detected. On the other hand, σ_x stress component remain practically negligible in all cases. Surprisingly, observed stress distribution behaves in an opposite way – higher stress level (σ_z = ~500 MPa) and larger relaxation length of stresses in heat-affected zone (~30 mm) are detected in the plate "sample 3". More favourable values were observed in plates "sample 1" and "sample 2"; amplitude of σ_z = ~300 MPa and relaxation length of about 20 mm).

The width of the stress relaxation region in the heat-affected zone of the sample 3 is practically identical in all examined depths (see Fig. 23). On the other hand, the width of the stress relaxation region in plates "sample 1" and "sample 2" follows the width of the weld joint insight the plate and becomes narrower in z = 0 mm and z = -7.5 mm (see Fig. 22b).

In the case of the plate "sample 2", it was practically impossible to measure reliable values of the strains within the weld joint, because the diffracted neutron intensities were strongly attenuated in this region, especially in strain components measured in transmission geometry. The possible interpretation of this effect is a slight contamination of the weld metal by an element strongly absorbing thermal neutrons, such as cadmium or boron.

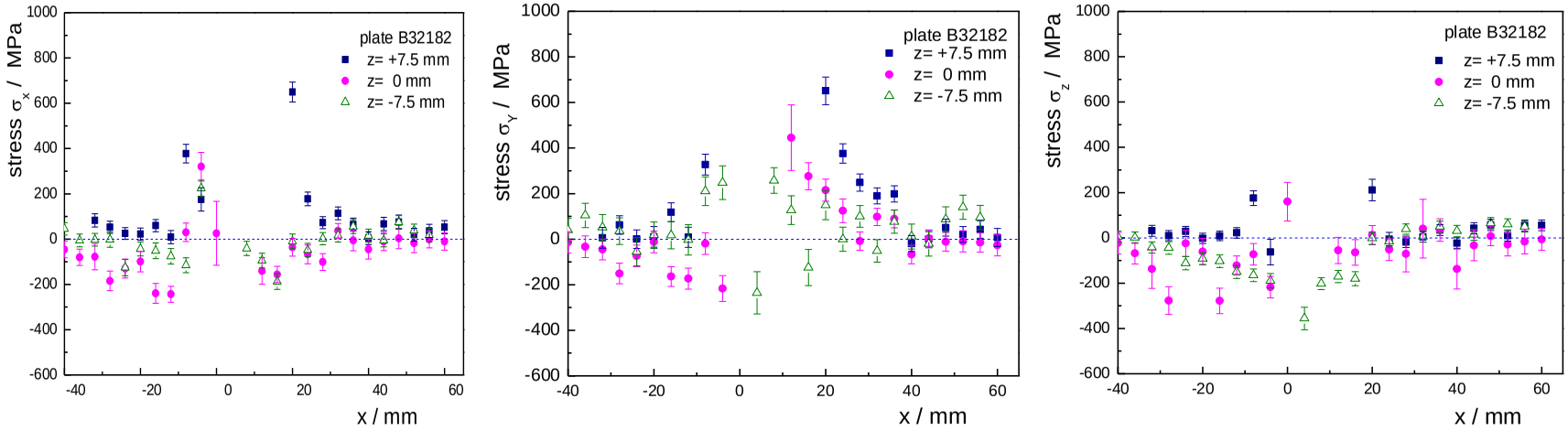

FIG. 22. Scans of individual stress components measured at different depths in the plate "sample 2" (x-component (left), y-component (middle) and z-component (right)).

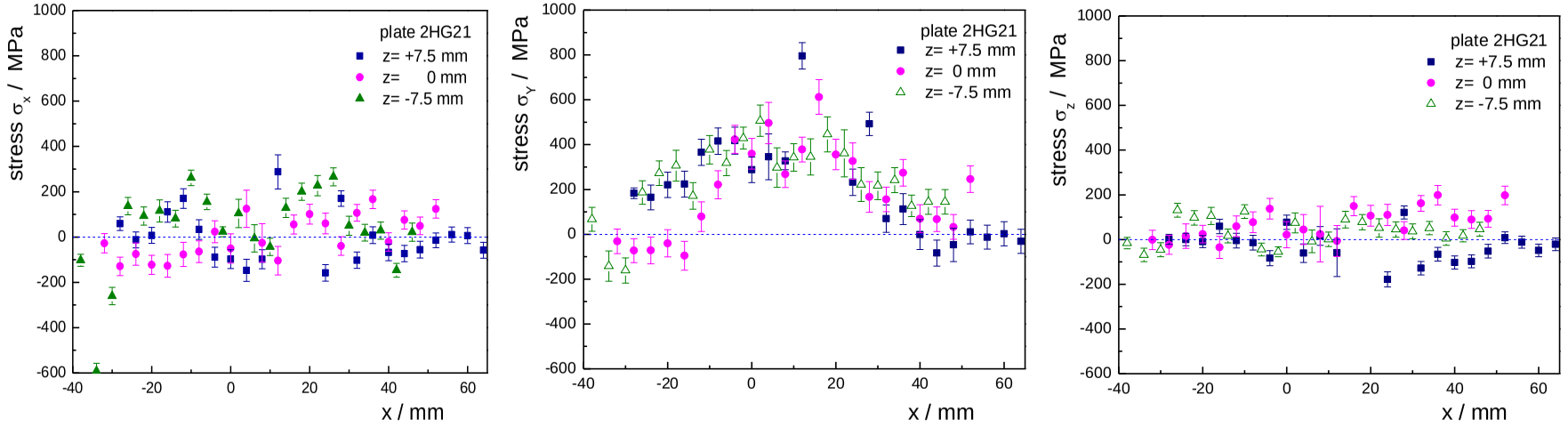

FIG. 23. Scans of individual stress components measured at different depths in the plate "sample 3" (x-component (left), y-component (middle) and z-component (right)).

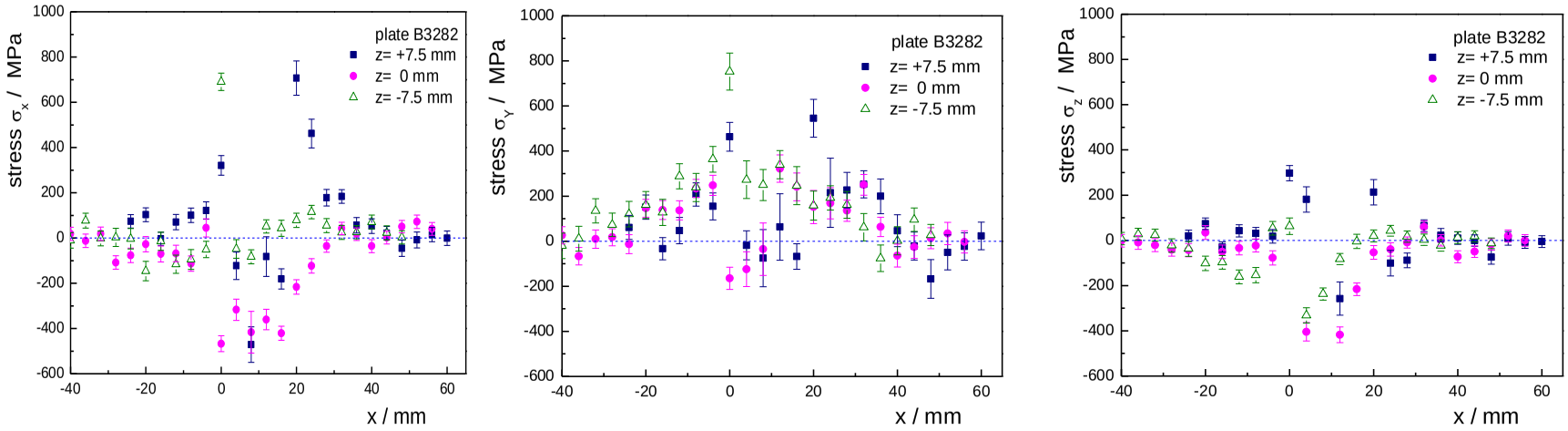

FIG. 24. Scans of individual stress components measured at different depths in the plate "sample 1" (x-component (left), y-component (middle) and z-component (right)).

Neutron diffraction mapping of residual stresses in the vicinity of electron beam welds of Charpy-V notched specimen

The Charpy-V test is very important to monitor the neutron embrittlement of the reactor pressure vessel (RPV). In national rules a maximal shift of the ductile – brittle transition temperature determined from Charpy-V tests is defined which is forbidden to exceed during the life time of the reactor. Surveillance specimens of irradiated RPV steel are of very limited availability and therefore very valuable. On the other hand, the gauge volume of the Charpy-V test is limited to the range directly ahead the notch. Therefore, surveillance specimens can be used more than one time by using the broken parts again and weld some additional material outside the gauge volume.

In this case, the specimens with welds on one side as well as with welds on two opposite sides were prepared. Welding was performed with electron beam in vacuum according ASTM E1253. This technique of constructing specimens from small pieces of material is usually called reconstitution. Such miniaturized specimen technology permits the characterization of mechanical behaviour while using a minimum volume of material. The compound specimen is achieved by attaching an additional material (A) around a material of interest (the insert material - B) which results in a test specimen of standard dimensions. The incorporation of a small piece from a previously tested specimen into a compound one, allows e.g. to multiply the number of tests. This can be especially important if the amount of the available material is restricted and mechanical parameters have to be determined. Very often one can meet with such necessity in the nuclear power plant industry e.g. nuclear pressure vessel surveillance, failure analysis, and post irradiation testing.

The interface between the stud and the insert is created by using welding techniques. However, before testing the mechanical properties the microstructure after welding has to be examined to ensure that the material in the vicinity of the notch is essentially unchanged after the welding process. For example, it is well known that the residual stresses resulting from the welding process can be non-negligible even at the distance up to several millimetres from the notch and thus significantly influence the mechanical properties of the material and in this case on the insert material. In our case electron-beam welding (EBW) was used. Welded pieces were of low-alloy ferritic steel material. The central part of the samples was made of reactor pressure vessel steel (surveillance material). Welding was performed with electron beam in vacuum according to ASTM E1253. After the residual strain/stress measurements (Fig. 25), the Charpy-V specimens were used for performing the impact tests in accordance to the standards ČSN ISO 148-1 and ASTM E23. In the present case the strain/stress measurements had to map the internal stresses after welding, especially in the middle part of the testing sample B, which is the subject of the followed mechanical tests. The main notch is located in the centre of the specimen.

FIG. 25. Photo of the specimen with the weld on one side as installed on the neutron beam defined by slits.

Figures 26 and 27 reveal that residual stresses are present in the vicinity of electron beam weld. Their maximum reaches the value 400-500 MPa. They are, of course, not present at the depth of 7.5 mm of the sample with the weld only on one side, where the heat affected zone is missing (see middle of Fig. 26). Taking into account stress distribution along the scan-axis in the material (along the longest edge of the sample) it can be seen that significant stresses are extended in the area of the length of about 5 mm and in the case of the welding on both sides, the stresses reach the middle area of the insert. More details about the experiment can be found in Ref. [19].

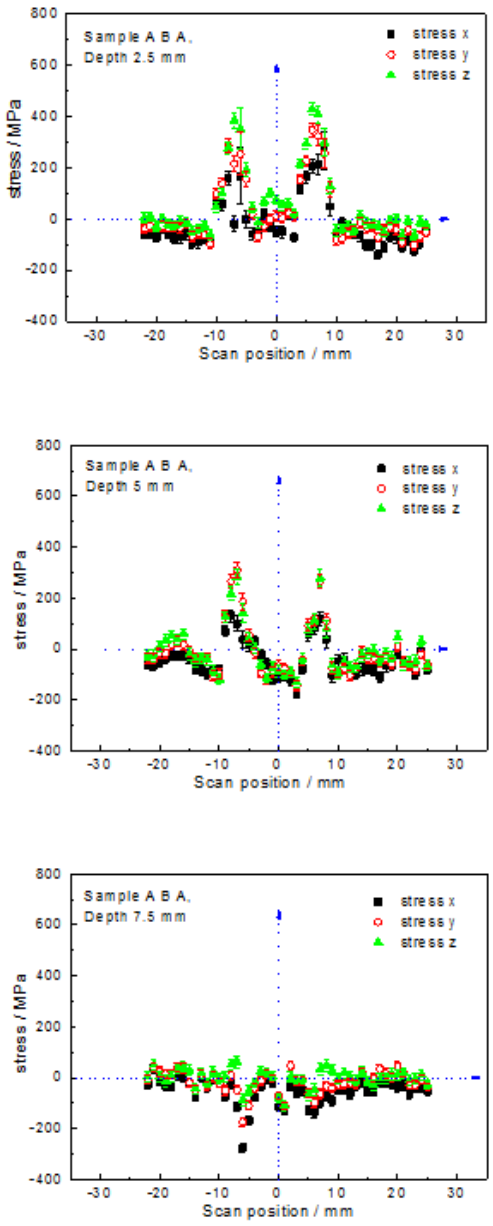

FIG. 26. Residual stress scans performed at different depths in the material for the sample with the weld on one side. See the figure legends for top, middle and bottom figures.

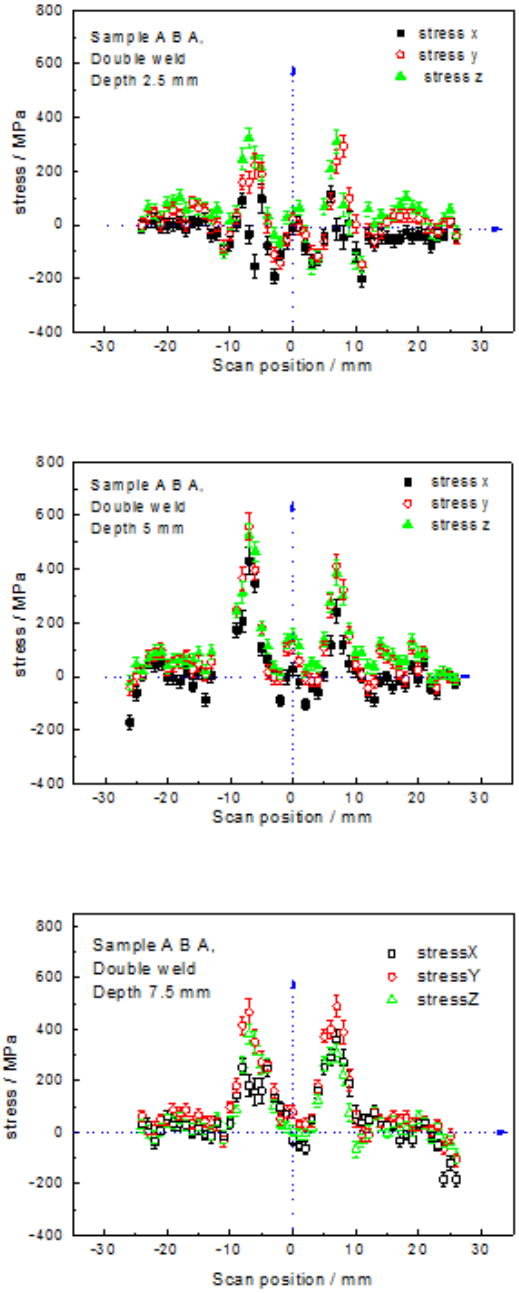

FIG. 27. Residual stress scans performed at different depths in the material for the sample with the weld on both sides. See the figure legends for top, middle and bottom figures.

Residual stress distribution measurement by neutron diffraction in the ferritic single pass fillet steel welds

The aim of these studies was to find an optimum composition of the additive material in order to decrease residual stresses in the vicinity of the foot of the welding joint and consequently to increase the fatigue strength [20, 21]. It is based on the conception of so called LTT (low transformation temperature) metal used for electrodes which (according to a theory) de-creases the level of residual stresses and increases the fatigue strength. WELDOX-700 and DOMEX-650 – refined high strength steels having the yield strength 700 MPa (in reality up to 817 MPa resp. 650 MPa) were used as a base material. Three parent

materials and seven different filler materials were used for the test specimen preparation. Altogether seven test specimens were used for the residual stress distribution measured by neutron diffraction. The photo of one of the samples is shown in Fig. 28. Combinations of parent and filler materials are shown in Table 1. Shielding gas Ar + 2%CO_2 was used for welding.

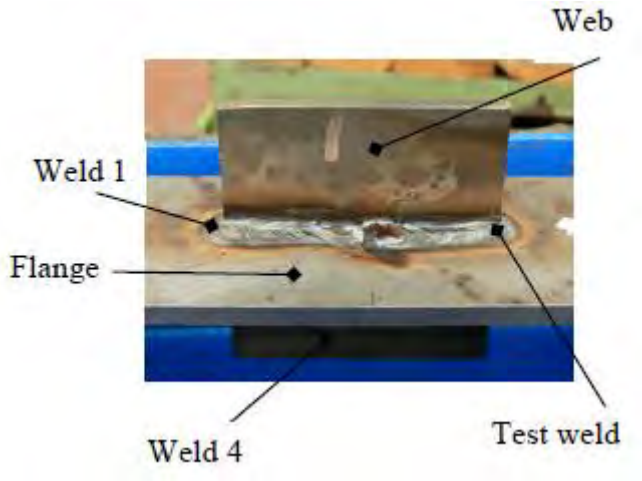

FIG. 28. Photo of one of the samples.

TABLE 1. COMBINATIONS OF PARENT AND FILTER MATERIALS

Specimen designation	Parent material	Filler material
A11	WELDOX 700	LTT-M6
B10	WELDOX 700	B-M3
C11	WELDOX 700	D4-647
E12	WELDOX 700	OK Tubrod 14.03
J11	DOMEX 650	D3-5724
K12	X2CrNi12	D3-6547
L12	X2CrNi12	OK Tubrod 15.30

As an example of variety of the obtained experimental results, Fig. 29 demonstrates the effect of using different filler materials (A-LTT-M6, B-B-M3, C-D4-6547, E-Tubrod 14.03, and J-D3-5724) on individual components of residual stress distribution in the vicinity of the weld with the parent material WELDOX 700/690QL.

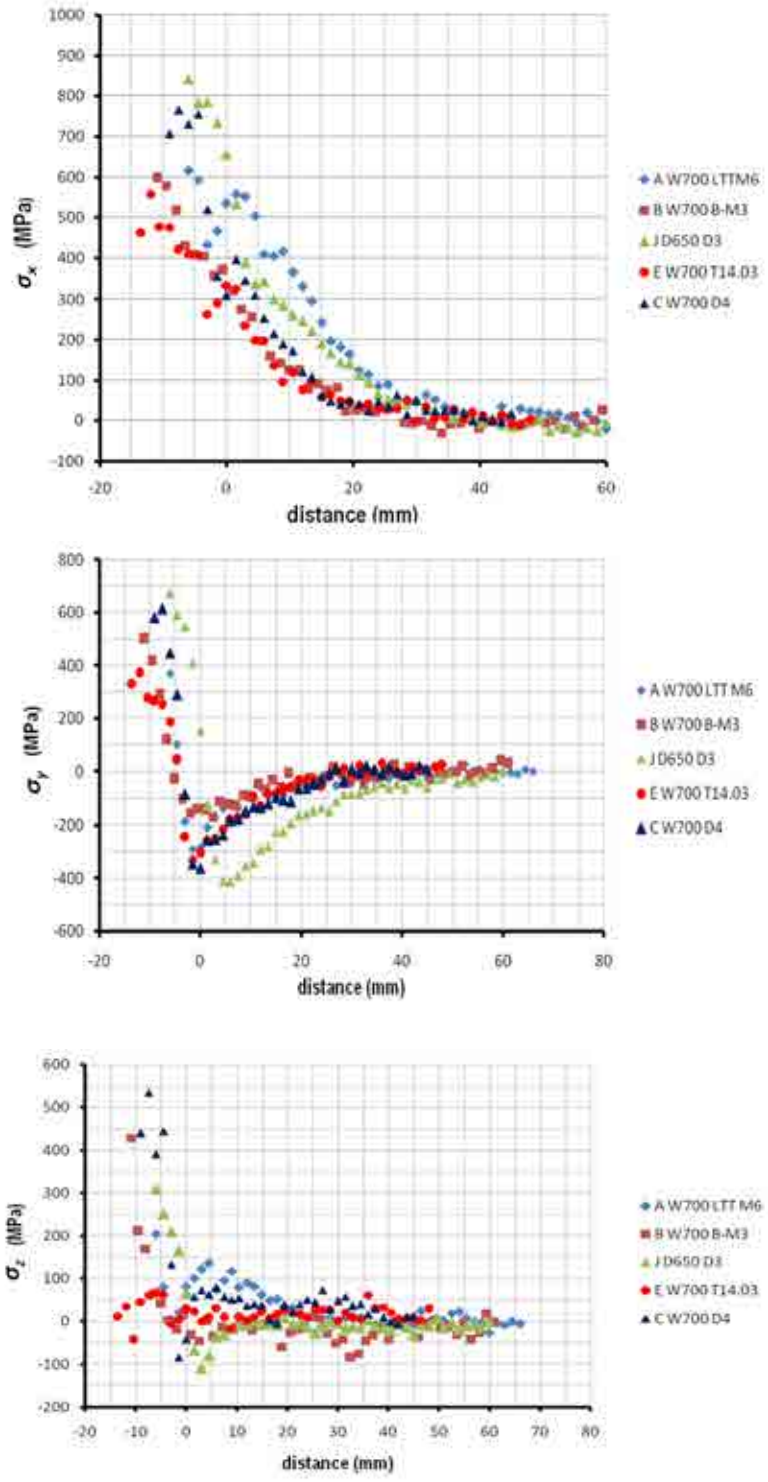

FIG. 29. Components of residual stresses in the vicinity of the weld for the WELDOX 700/690QL parent material and several different fillers. See the figure legends for top, middle and bottom figures.

The following phenomena were studied:

- The effect of filler material LTT-M6(A), B-M3(B), D4-6547(C), Tubrod 14.03(E) welded on high strength steel WELDOX 700 on residual stress distribution;
- The effect of filler materials D4-6547 and Tubrod 15.30 welded on high alloyed steel X2CrNi12 (1.4003) parent material on σ_x, σ_y and σ_z residual stress components distribution;
- The effect of parent material high strength WELDOX 700/690QL and Domex 650MCD steels welded by D4-6547 and D3-5724, respectively, on σ_x, σ_y and σ_z stress components;
- The effect of parent materials high strength Weldox 700/S690QL and high alloyed X2CrNi12 (1.4003) steels welded by D4-6547 filler material on Rx, Rz and Ry stress components;
- The effect of parent materials high strength Weldox 700/S690QL and high alloyed X2CrNi12 (1.4003) steels welded by Tubrod 14.03 and Tubrod 15.30 respectively, on σ_x, σ_y and σ_z stress components;
- The effect of weld location of No. 1 and No. 4 test fillet welds prepared on high strength steel Weldox 700/S690QL welded by D4-6547 filler material on σ_x, σ_y and σ_z stress components.

Neutron diffraction measurements of residual stresses in thick welds

In some samples, e.g. in steels, attenuation of the material gives a significant limitation to neutron diffraction measurements of residual stresses, because the diffraction signal becomes weak (comparable or even below the background) and the measurement becomes inefficient. In order to overcome this problem (at least partially), it is necessary to use an experimental facility with a low measurement background, a high current of the monochromatic beam suitably prepared and formed by neutron optics elements and to exploit neutron wavelengths where a studied material has minima in total neutron cross-section. The latest achievements in this direction can be found in section 2.5 of this document.

2.3.2. Creep studies in Ni-based CMSX4 super alloy by SANS

Ni-based superalloys exhibit a two-phase microstructure consisting of γ′ precipitates growing in the gamma phase matrix. It is the basic feature which determines e.g. a high creep-resistance of nickel-base superalloys. Outstanding high-temperature mechanical properties of these materials strongly depend on the morphology of the precipitates and thus also on the applied heat treatment. During the creep load on CMSX4 superalloy, rafting of originally cuboidal precipitates takes place. The degradation procedure can be investigated by the analysis of the geometrical parameters of γ' precipitates in γ matrix. A new conical form of the sample which was exposed at 1100°C for 100 h was used (see Fig. 30). It permitted to test the stress level continuously in one sample and to obtain variation of the micro-structural changes (see Fig. 31). The development of the morphology of rafts on the value of deformation could be obtained by SANS - average thickness of the channels between the rafts in different crystallographic directions of the single crystal, development of the dimensions of γ' precipitations and their distance and the development of specific surface of the precipitates (see Fig. 32). More details related to this topic can be found in Refs. [22, 23].

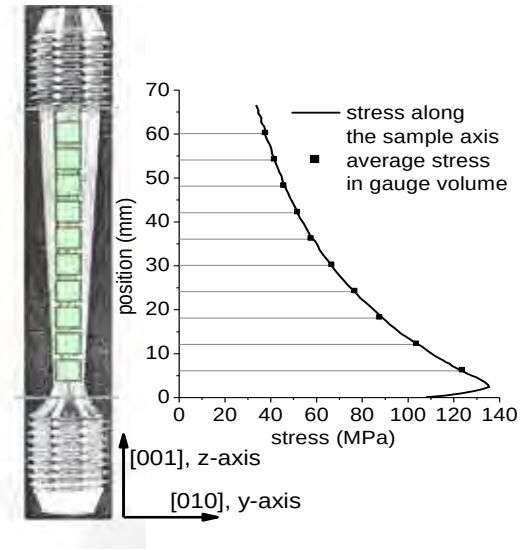

FIG. 30. The picture of the tested specimen (left). Ten points scanned during the SANS experiment are marked. Stress dependence (σ_{min}=35 MPa, σ_{max}=135 MPa) on the position along the sample axis and average stress in the measured gauge volumes (right).

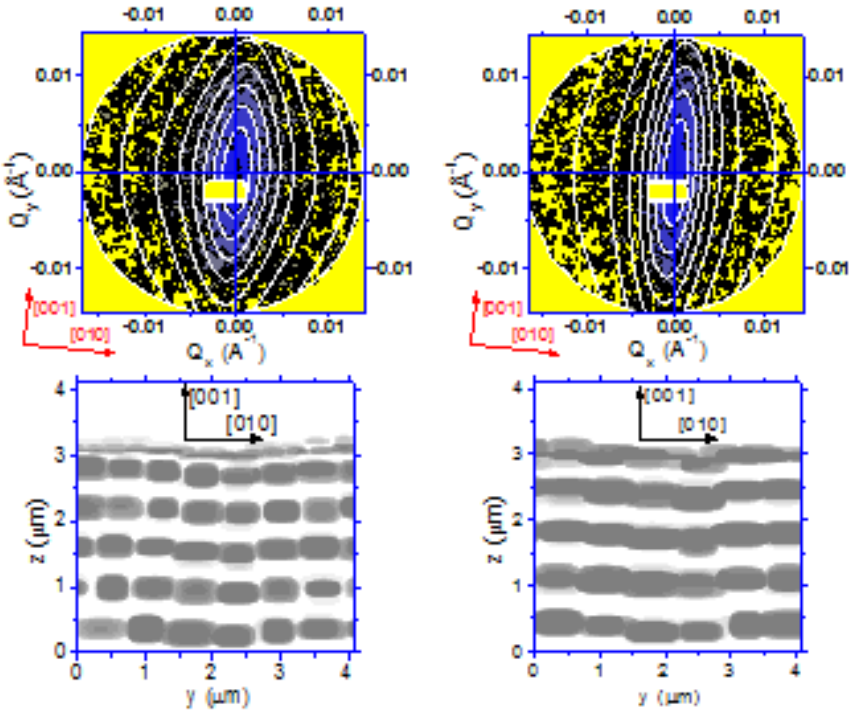

FIG. 31. Scattering curves at two of the scanned points: (a) minimum and (b) maximum stress, respectively. Orientation: [100] parallel to the beam, [001] nearly vertical. Measured data are shown as the colour-scale maps whereas the optimum 2D fits are depicted by the white equal intensity lines. (c), (d): sections through the optimum 3D models (gray: γ' rafts; white: matrix) for the (a) and (b) fits, respectively.

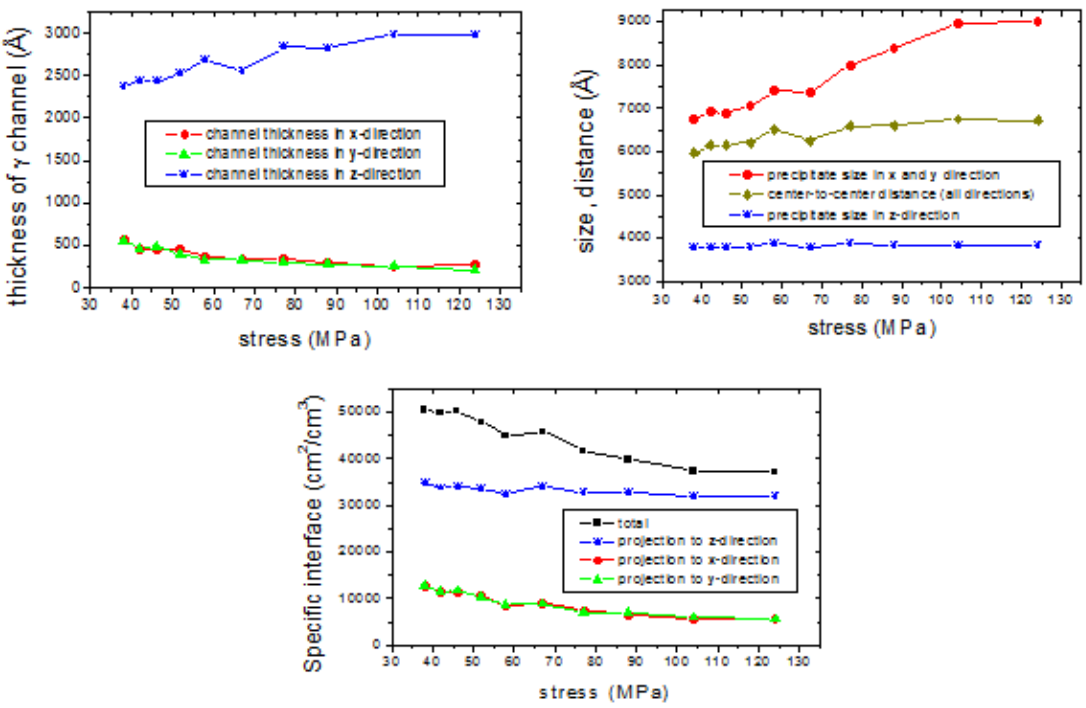

FIG. 32. Resulting evolution of parameters: (left-top) the mean thickness of the g' channel in the respective directions (x–direction is [100], y–direction is [010] and z–direction is [001]), (right-top) the relative evolution of the average precipitate size and distance, (bottom-middle) the relative evolution of the specific interface - total and projection to the respective directions.

2.3.3. Neutron diffraction analysis of Incoloy 800HT and 304L steel samples with different heat treatment

This experiment was carried out in the cooperation with the CRP partner INR-Pitesti, Romania, where the samples were prepared. In total eight samples of two groups were analysed by neutron diffraction on the powder diffractometer MEREDIT at room temperature. First group, referenced here as ig800 was Incoloy 800 HT steel, was consisted of four samples which passed heat treatment at 450°C, 500°C, 550°C and 600°C for 60 days. The second group, referenced here as ol304L was 304L steel, consisted also of four samples which passed the same heat treatment at 450°C, 500°C, 550°C and 600°C for 60 days. All of the samples were in the form of sheets with the rectangular shape of 15 × 25 mm^2 of the thickness of 2 mm with a small hole in the top part. The hole was used for fixing the samples by Cd-wire to the carousel and placed perpendicularly into the neutron beam. The diffraction pattern was collected from the whole volume of the sample. Mosaic copper monochromator (reflection 220) providing the wavelength 1.46 Å was used for this measurement in the range of scattering angles between 4° and 144°. Refinement was performed using FullProf software. First refinements were performed using the full pattern refinement with the structural model just to see and identify the phases in the samples. Next refinement strategy was selected to refine the individual reflections without any structural model to see shifts in the angular reflection position as a function of temperature of the thermal treatment. During the calculation global parameters of background and for individual reflection parameters of intensity, position and value of *FWHM* were refined.

For the full pattern refinement the IRF (Instrumentation Resolution File) was used describing the profile parameters coming from the instrument and was obtained by refinement of the SiO_2 standard sample at the similar conditions.

The apparent reflections in the diffraction pattern were analysed and identified as coming from the austenite phase with space group Fm$\underline{3}$m and cell parameter $a \approx 3.59$ Å for all eight samples. Thus, there were no phase changes brought about by changing the temperature of the thermal treatment. Small reflections observed on the background at different angles were identified as (λ/2)-reflections because of very high (over 8000 counts) intensity of main reflections. The contamination of the ((λ/2)-reflections denoted by the ratio of $I(\lambda/2)/I((\lambda)$ was about 0.44%. Observed and calculated diffraction patterns for the sample ig800-450 are shown in Fig. 32. As all the samples seemed to be monophase, we analysed the relative peak position and peak broadening by the fitting of the individual reflections. For the refinement, all eight reflections of austenite structure visible in the diffraction pattern in the measured 2θ–region, namely 111, 200, 220, 311, 222, 400, 331 and 420 reflections, were selected. The (λ/2)-reflections were omitted. The profile parameters were taken from the IRF2 file. The refined parameters of each reflection were: angular position, shift of *FWHM* (considered as resolution in powder diffractometry) and integrated intensity. From the refined position the strain ε was calculated using of Eq. (2a).

The evolutions of these parameters *(ε,* and $\Delta d/d$*)* as a function of the temperature of thermal treatment are shown in Figs. 34 and 35 for both groups of the samples. The temperature of 450°C of thermal treatment was taken as reference (for $d_{0,hkl}$) for ε calculation.

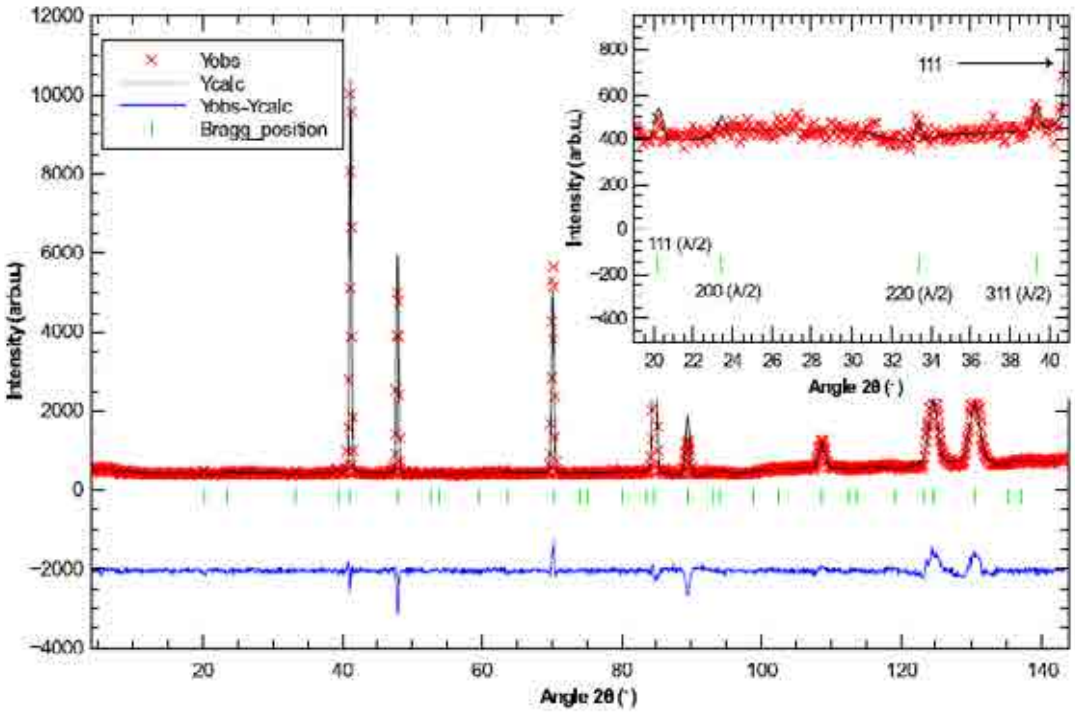

FIG. 33. Observed and calculated diffraction pattern for the sample ig800-45. Inlet shows the small reflections attributed to the second contributions of the main reflections.

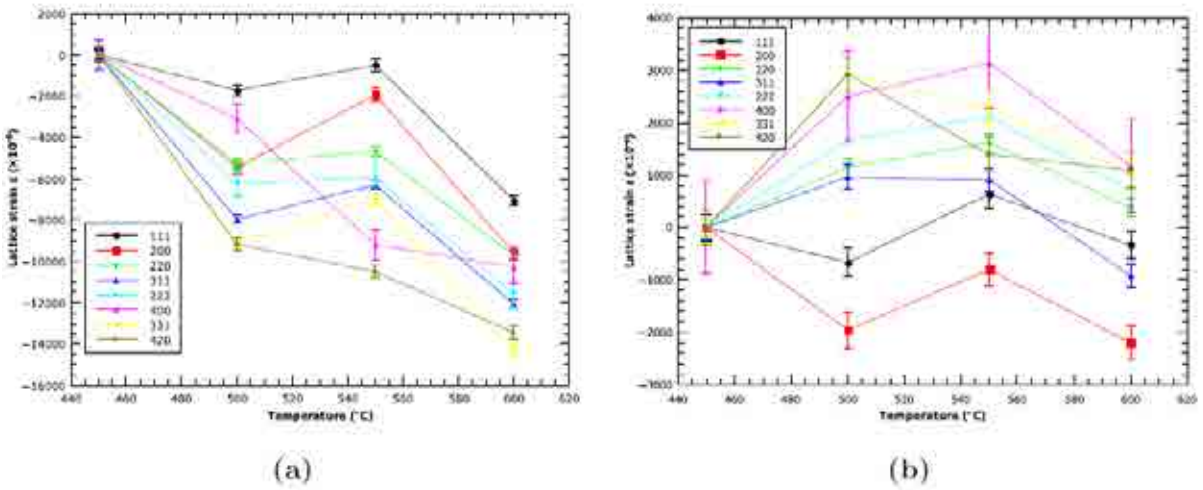

FIG. 34. Sample strain ε calculated for the individual reflections as a function of temperature of thermal treatment for samples ig800 (a) and ol304L (b).

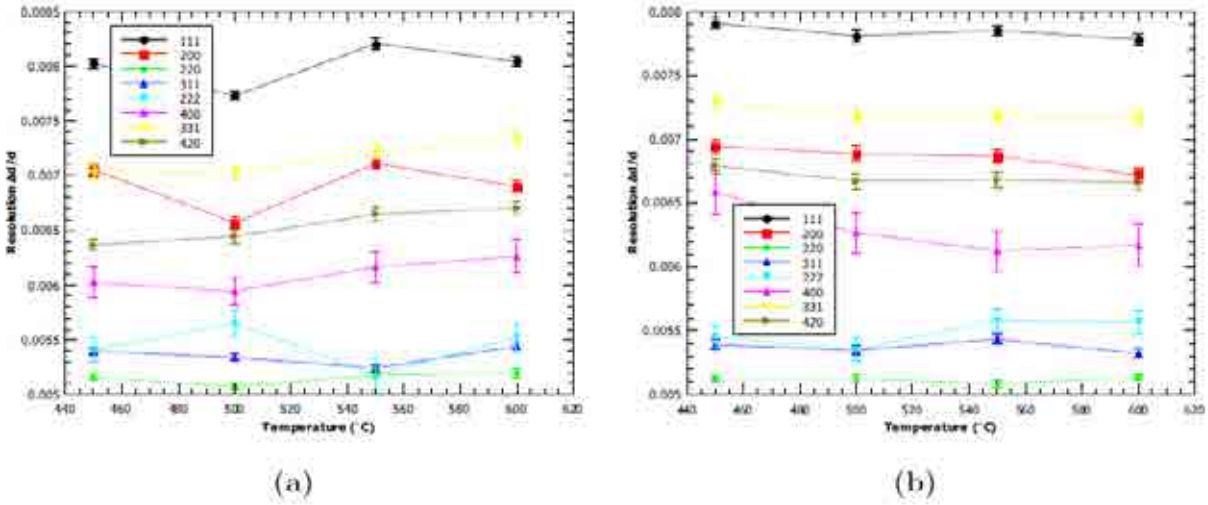

FIG. 35. Value of Δd/d calculated for the individual reflection as a function of temperature of thermal treatment for samples ig800 (a) and ol304L (b).

Figure 35 reveals that the values of resolution slightly increase with the increase of the temperature of the thermal treatment for the ig800 samples. In contrast, for ol304L the values of the resolution are rather constant or have a decreasing tendency with the increase of the temperature. It corresponds to the increase of the micro-strain in the ig800 samples with increasing the temperature. This is in an agreement with the view on the macroscopic lattice strain which dramatically increases with the temperature of thermal treatment in the case of ig800 samples. The negative values of the lattice strain represent the movement of the reflections to higher angles (see Fig. 34) and thus the *d*-spacing decreases which leads to compression forces in the sample. However, in the samples ol304L the evolution of the lattice strain is different. For most of the reflections, except the 200 reflection, the *d*-spacing moves to the higher values and thus the material is in tension. The softest direction [200] follows the opposite way. The fluctuation of the intensity of the high *d*-spacing reflections can be due to the change of the grain and size distributions when the temperature of the thermal treatment is changed.

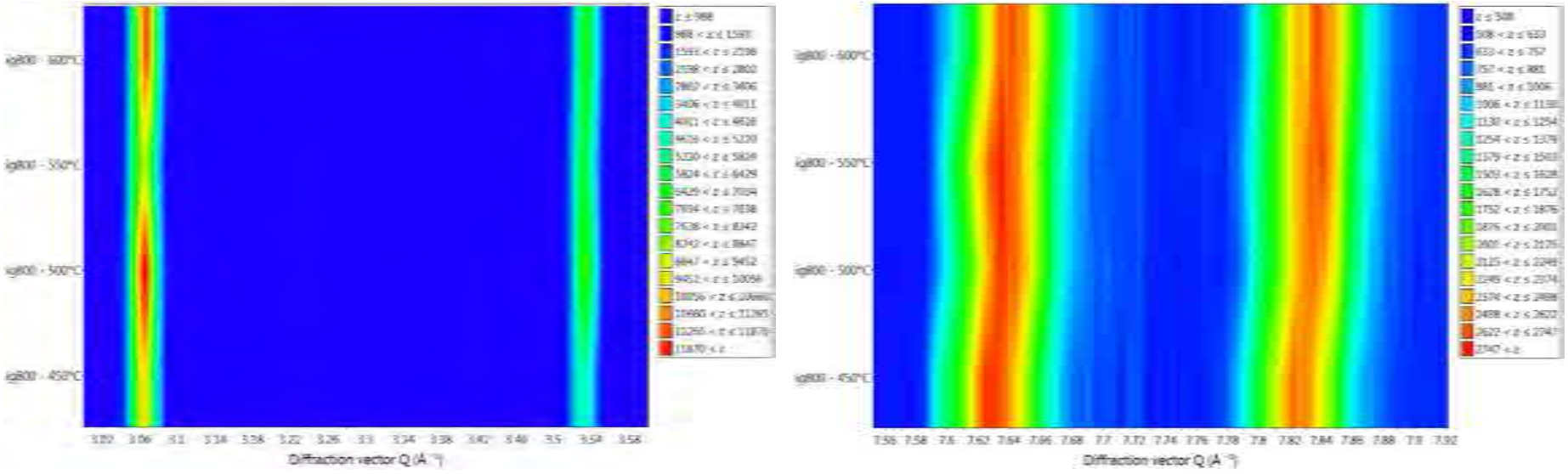

(a) (b)

FIG. 36. Evolution of the position of the reflection with the temperature of the thermal treatment for the ig800 samples. The x axis corresponds to the diffraction angle. (a) 111 and 200 reflections; (b) 331 and 420 reflections.

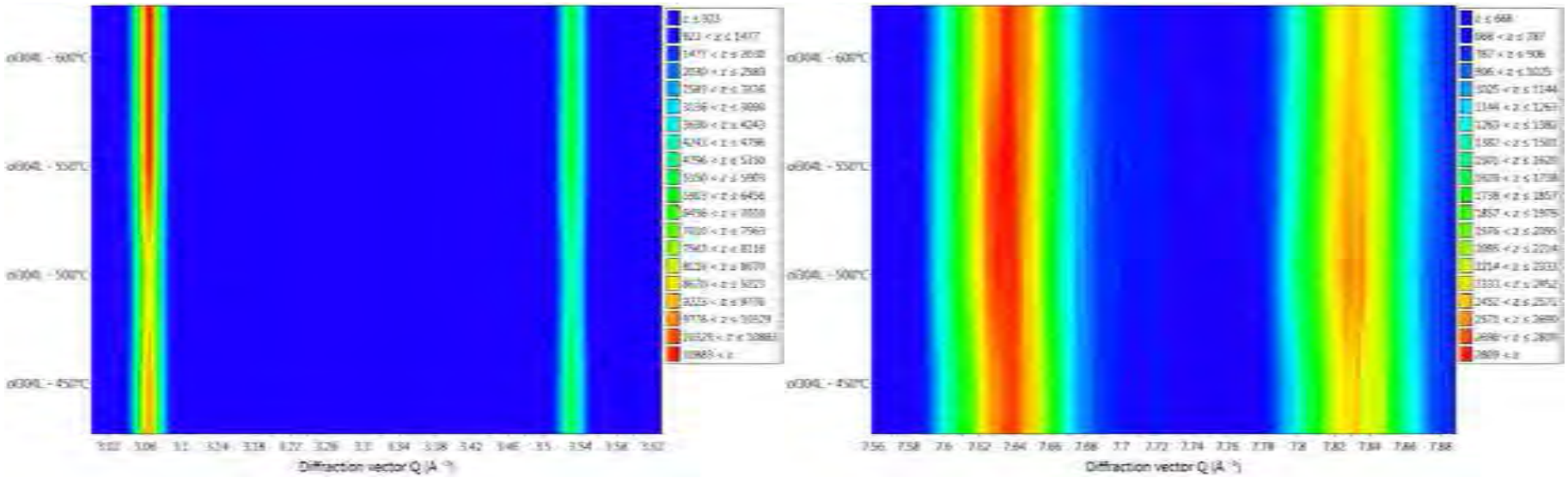

(a) (b)

FIG. 37. Evolution of the position of the reflection with the temperature of the thermal treatment the ol304L samples. The x axis corresponds to the diffraction angle. (a) 111 and 200 reflections; (b) 331 and 420 reflections.

2.4. RESULTS WITH IRRADIATED MATERIALS

The investigation of material processes occurring during irradiation is a big challenge for solid state physics and material science. Irradiation with high energy neutrons, protons or heavy ions results in the formation of the so called collision cascade, in which the particles can knock out atoms from their lattice position forming vacancies and interstitial atoms. These interstitials can conglomerate two-dimensional at dense packed lattice plans forming dislocation loops. Three-dimensional conglomeration results in the formation of foreign atom - vacancy clusters and precipitates. The formation of collision cascades enhances diffusion processes. The first process is known as irradiation induced precipitation, the second one is called irradiation enhanced. Another source of irradiation defects are nuclear reactions for instance the (n,α) reaction. The formed helium can conglomerate to nano-bubbles concentrated at positions with higher diffusivity like grain boundaries or dislocations.

Irradiation also leads to changes in the stability of second-phase precipitates and the local chemical equilibrium near grain boundaries, precipitates, and defect clusters. Grain-boundary microchemistries that differ significantly from the bulk composition can be produced not only by radiation-induced segregation but also by thermally driven equilibrium and non-equilibrium segregation of alloying and impurity elements. Although irradiation-induced grain-boundary depletion of Cr has been considered for many years to be the primary metallurgical process cannot be explained well by Cr-depletion theory. The formation of chromium rich α' precipitates in steels with chromium content above 9% are an example for it.

The size ranges of irradiation induced or enhanced defects are of the order of 1 nm. Therefore advanced methods have to be applied to investigate these defects. Just to list a few, X ray and neutron diffraction, small angle X ray or neutron scattering, transmission electron microscopy, positron annihilation spectroscopy, Mossbauer spectroscopy, atom probe field ion microscopy and magnetic measurement (magnetic hysteresis, Barkhausen) are used to investigate these phenomena. Because structural materials like ferritic-martensitic or bainitic steels have an inhomogeneous microstructure one method alone does not provide enough information to characterize the defects. Indeed, different methods have to be combined to improve the knowledge about irradiation defects. In the following text, the focus is on the neutron based methods.

Irradiation defects result in a degradation of the material properties. Neutron hardening and embrittlement are well known consequences. These changes on atomic level lead to changes for the macroscopic behaviour of the components irradiated. These macroscopic changes can be investigated by means of neutron imaging methods.

The high penetration depth of neutrons allows applying various sample environments. Irradiated materials often become activated, and therefore special shielding has to be applied. For instance at PSI the NEURAP shielding for radiography measurements and a special shielded box for SANS with the possibility of including a sufficient magnet were constructed. The SANS shielding has as a special feature a single crystalline led beam window attenuating the γ radiation but nearly not the neutron beam.

A problem of investigation of radioactive materials is the very high administrative effort for transport and storage. It makes it very difficult to transport such samples abroad. Therefore, the investigations were performed mostly at the local neutron source of the country where the samples were irradiated and prepared for investigations.

2.4.1. Neutron Diffraction on irradiated materials

The neutron diffraction investigations performed at LANL at irradiated Zr2.5%Nb specimens were already reported in section 2.2.1.

In addition, there is a wide spectrum of investigation of reactor steels. Ferritic/martensitic steels such as T91 (9Cr1Mo) and HT-9 (12Cr1Mo) have also been used for nuclear fuel cladding. In similar work to that of the Zirconium study, Hosemann et al. studied the evolution of the microstructure, i.e. phase composition and texture, in situ using neutron diffraction [24].

Deformation behaviour was investigated by Clausen et al. [25] using in situ neutron diffraction and modelled using elasto-plastic self-consistent (EPSC) modelling. These experiments on (non-irradiated specimens) provide baseline data for future experiments on irradiated materials. Comparing the mechanical response of irradiated and non-irradiated materials will allow understanding the influence of radiation damage on the mechanical behaviour of these materials and providing benchmark data for advanced deformation models that attempt to include radiation damage [26]. In complementary work Anderoglu et al. studied the microstructure and phase evolution in a fully tempered ferritic /martensitic HT-9 steel irradiated in the Fast Flux Test Reactor Facility (FFTF) up to 155 dpa at a temperature range of 380-504°C [27] using SANS with the LQD instrument.

As part of this CRP, two austenitic steels, ChS68 and EK164, applied for fast breeder reactor fuel claddings were examined at the Russian Institute of Nuclear Materials. The specimens were irradiated in the BN-600 reactor up to maximum dose of about 80 dpa. These investigations were performed at the D7A diffractometer using a monochromic beam of $\lambda = 0.1805$ nm. The diffraction pattern was recorded with the angle increment of 0.1° in the angular intervals of 5-120°. Obtained data are recorded by a computer and processed with the Rietveld method.

According to the ND experimental data the specimens of both steels have bright marked texture. It is connected with cold deformation treatment during tube manufacturing. The relations of the intensity of the reflexes (111)/(200), (111)/(220), and (111)/(311) were calculated to trace the texture changes. The texture of the materials remains even after irradiation up to 81 dpa, but becomes less than the original one. Maximum decreasing is observed after irradiation at temperatures of 370-390°C and low doses. The effect is weaker after irradiation at temperatures of 520-528°C even at high doses. Table 2 demonstrates the observation results.

It shows that the texture of the *EK164* steel is more stable under irradiation, than in case of the *ChS68* steel. For example, the relative change characteristics of specimens irradiated up to high doses in comparison with unirradiated specimens of the steel *ChS68* are equal to 1.38 and 1.19 (for different reflexes). In the case of the *EK164* steel this relations are 1.19 and 1.04, respectively.

TABLE 2. THE RELATIONS OF THE INTENSITY OF THE REFLEXES (111)/(200), (111)/(220), AND (111)/(311) FOR THE *CHS68* AND *EK164* STEELS

Steel	Dose, dpa	(111)/(200)	(111)/(220)	(111)/(311)
ChS68	0	0.33	0.13	0.37
	1.5	0.33	0.20	0.48
	81	0.30	0.18	0.44
EK164	0	0.35	0.21	0.51
	14.5	0.37	0.27	0.55
	72	0.39	0.25	0.53

Micro-deformations ($\Delta d/d$) and size of coherent scattering areas (L_{CSA}) were calculated by different reflexes characteristics of ND. They are exhibited in Tables 3 (for ChS68 steel) and 4 (for EK164 steel). The micro-deformation in both irradiated steels is larger in comparison with their initial state. Their increase is connected to the formation of dislocation loops and small voids. The micro-deformation changes are different for the two steels. They increase with dose growth for the ChS68 steel as Fig. 38 shows. These changes are non-monotonic for the *EK164* steel (Fig. 39). The dose dependences on size of coherent scattering areas are different too. It increases with dose growth for the *ChS68* steel and decrease for the *EK164* steel respectively.

TABLE 3. THE VALUES OF MICRO-DEFORMATION AND THE SIZE OF CSA OF SPECIMENS OF THE *CHS68* STEEL CALCULATED BY NEUTRON DIFFRACTION DIAGRAMS

Characteristic	Dose, dpa	0	1.5	81
	Temperature,°C	-	370	520
Micro deformation $\Delta d/d \cdot 10^{-4}$	Indexes(hkl)			
	111	9.8	11.9	13.4
	200	29.5	35.9	40.3
	220	14.8	17.9	20.1
	311	24.2	29.4	33.0
	222	9.8	11.9	13.4
	400	29.5	35.9	40.3
	Average	18	24	27
L_{CSA}, nm		64	68	105

TABLE 4. THE VALUES OF MICRO-DEFORMATION AND THE SIZE OF CSA OF SPECIMENS OF EK164 STEEL CALCULATED BY NEUTRON DIFFRACTION DIAGRAMS

Characteristic	Dose, dpa	0	14.5	72
	Temperature,°C	-	390	528
Micro deformation $\Delta d / d \cdot 10^{-4}$	Indexes (hkl)			
	111	10.7	15.2	11.4
	200	32.2	45.7	34.1
	220	16.1	22.8	17.1
	311	26.4	37.4	27.9
	222	10.7	15.2	11.4
	400	32.2	45.7	34.9
	Average	21	30	23
L_{CSA}, nm		74	54	46

The obtained results have shown anisotropic micro-deformations in the irradiated and non-irradiated specimens of both steels. Table 5 exhibits relations of micro-deformations in the directions (100)/(111) and (110)/(111). Here the data were taken from the work [28]. The relations for both steels are equal for non-irradiated as well as for irradiated specimens. Thus, micro deformation anisotropy is inherent in the austenitic steel cladding tubes and it is remained under irradiation. For comparison the reader can find similar values in the case of Steel 316 in Ref. [29].

TABLE 5. THE ANISOTROPY OF MICRO DEFORMATIONS OBSERVED IN BOTH STEELS. THE RELATIONS OF MICRO DEFORMATIONS IN THE DIRECTIONS (111)/(200) AND (111)/(220)

Steel	Dose, dpa	(111)/(200)	(111)/(220)
ChS68m, this work	0	0.33	0.67
	1.5	0.33	0.66
	81	0.33	0.67
EK164, this work	0	0.33	0.66
	14.5	0.33	0.67
	72	0.33	0.67

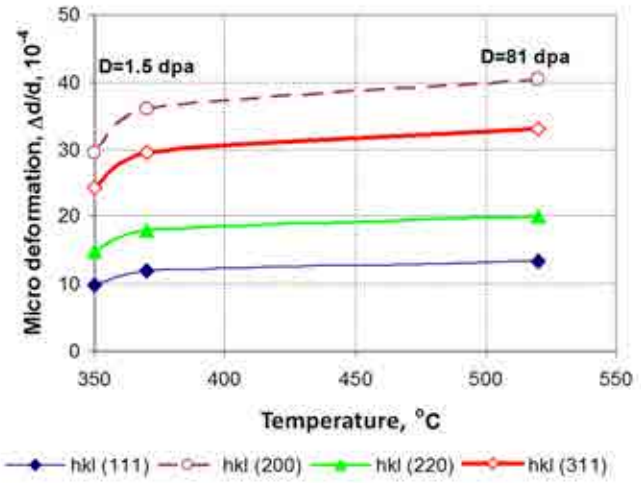

FIG. 38. Dependence of micro-deformations on neutron irradiation temperature of the ChS68 steel.

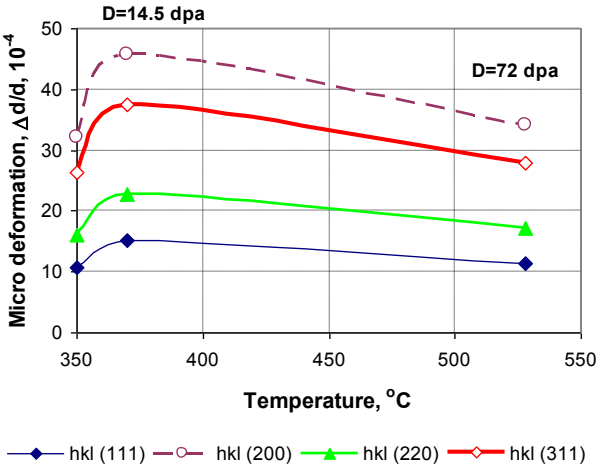

FIG. 39. Dependence of micro-deformations on neutron irradiation temperature of the EK164 steel.

2.4.2. SANS investigations of reactor pressure vessel steels

The austenitic cladding steels ChS68 and EK164 were investigated by SANS too. The investigations were performed at the D6 and D3 facilities using wavelengths of 0.478 and 0.243 nm, respectively. The D6 diffractometer uses polarized neutrons with polarization of 0.95.

It was found that the dose growth leads to increasing SANS intensities for both *ChS68* and *EK164* steels. The dependences of the total scattering cross section $d\Sigma/d\Omega$ on the scattering vector $\boldsymbol{Q}$ for the *ChS68* and *EK164* steels are shown in Fig. 40. The comparison shows that the changing of scattering of the *EK164* steel is greater than of the *ChS68* steel.

The scattering contrasts give hints that in initial state the scattering in mainly caused by titanium carbides TiCx. Other carbides have small contrast for the possibility to be a reason of the scattering observation.

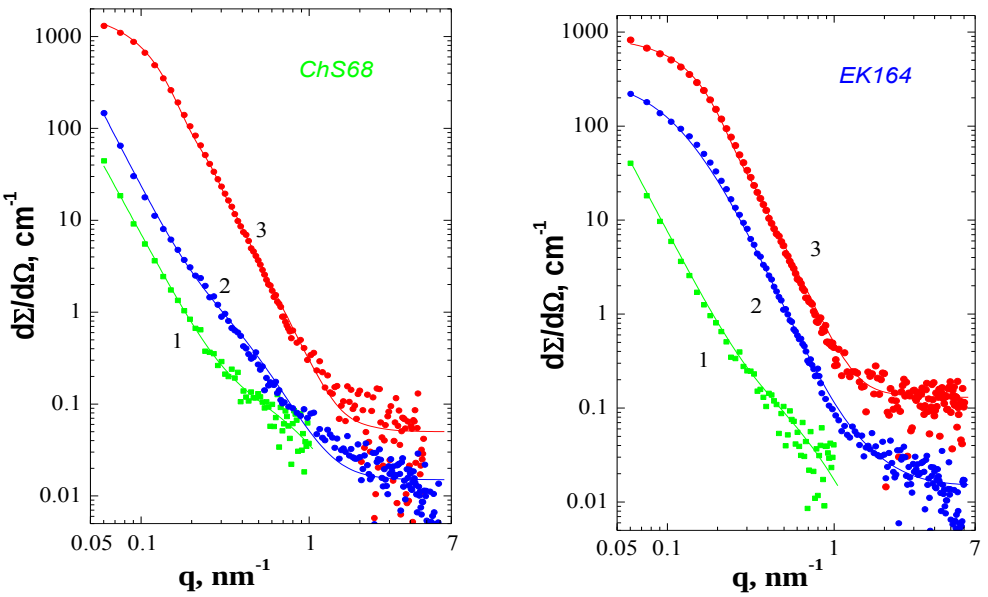

A B

FIG. 40. The SANS cross-section $d\Sigma/d\Omega$ vs. wave vector q for the ChS68 (A) and EK164 (B) steels: (1 – non-irradiated sample; 2 – sample irradiated with low dose; 3 – sample irradiated with high dose; points – experimental data; lines – model calculation).

Two models were applied to analyse the scattering measured at the irradiated specimens. The model 1 is based on stochastic phase particles distribution; used the Debye-Porod formula [30-34]. The model No1 has parameters: the particle size r, their volume part C and Porod parameter D_S. The model 2 uses power distribution on particles size: $N(R) \sim R^{-(3+\Delta)}$ with~~in~~ the interval from R_{min} to R_{max} [29] where 1 μm was the upper limit. Parameters: R_{min}, R, Δ, N, C were fitted to the experimental data. The use of two kinds of scattering particles with different size gives best description of the results, for low dose specimens. Scattering from high dose specimens are more correctly described in the model 2. The parameters are shown in Table 6 [see contributed paper by Kozlov et al.].

TABLE 6. PARAMETERS OF SUBATOMIC STRUCTURE OF SPECIMENS OF CHS68 AND EK164 STEELS

Spacemen and type of conditions	Mode 1			Mode 2				
	$2r$, nm	C	D_S	N, $\times 10^{21}$ m^{-3}	$2R_{min}$, nm	Δ	C	$2R$, nm
ChS68$_{unir}$	1.6	0.0024	2	0.27	4	0.5	0.0003	6.6
ChS68$_{low\ dose}$	4.0	0.0008	2	0.32	4	0.2	0.0005	7.2
ChS68$_{high\ dose}$	–	–	–	28	4	0.1	0.005	5.7
EK164$_{unir}$	2.4	0.0008	2	0.29	4	0.5	0.0003	6.6
EK164$_{low\ dose}$	1.0	0.002	2	–	$2R = 17$	D_S = 2	0.005	–
EK164$_{high\ dose}$	–	–	–	45	4	0.1	0.006	5.2

It can be concluded that the irradiation results in an increase of inhomogeneities with a size of about 4 nm, in particular after irradiation at high doses. Further investigations of highly irradiated material are needed to clarify the various processes going on–during the irradiation.

At the Budapest Neutron Center SANS investigations on the irradiation induced structural changes in the Russian VVER-440 type RPV steel 15Kh2MFA were performed in cooperation with the Helmholtz Zentrum Rossendorf (Germany). The VVER-440 reactor type is widely used for instance in the Hungarian nuclear power plant in Paks. A 15H2MFA type forging material with an unirradiated reference condition and three different irradiation conditions up to neutron fluences of 2.94×10^{20} (sample A), 9.52×10^{20} (sample B) and 14.5×10^{20} cm^{-2} (sample C) (E> 0.5 MeV), respectively, were investigated. The size of the samples was 10 mm x 10 mm x 1 mm.

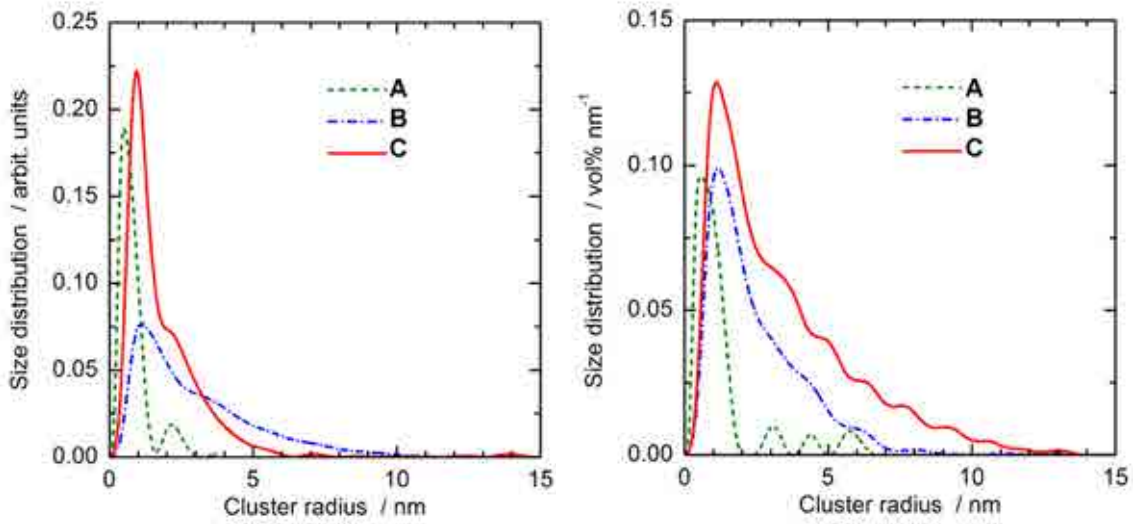

FIG. 41. Size distributions of irradiation-induced defect/solute atom clusters calculated from (left) the nuclear SANS contributions, and (right) from the magnetic SANS contribution (neutron fluences (E > 0.5 MeV) of the samples: **A***, 0.29*10^{21}cm^{-2};* **B***, 0.95*10^{21}cm^{-2};* **C***, 1.45*10^{21}cm^{-2}) [see contributed paper by Török et al.].*

The new SANS measurements were carried out with extended ***Q*** range and statistical accuracy. The results obtained by inverse fourier transform by Glatter method given in Fig. 41 verified the earlier findings that the size of magnetic inhomogeneities is larger than the nuclear ones.

The size of nuclear damage is between 1-2 nm, while the magnetic is slightly bigger. The possible effect of irradiation temperature and chemical composition was analysed. The results were presented at the 26th Symposium on the Effects of Radiation on Nuclear Materials, Indianapolis (USA), June 12–13, 2013 by F. Gillemot et al. on Microstructural changes in highly irradiated 15H2MFA steel and by A. Ulbricht on Analysis of SANS measurements on highly irradiated15H2MFA steel at the International Conference on Neutron Scattering in Edinburgh (UK), July 8 – 12, 2013 (Poster P.034)[see contributed paper by Shikama et al].

2.4.3. Investigation of nuclear fuel rods and highly irradiated components

The non-destructive character of neutron imaging can be used for non-destructive inspection of nuclear fuel rods or spallation target structures before as well as after usage. The neutron attenuation does not depend on the atomic number. In contrast to X rays, neutrons can penetrate some millimetres or centimetres of heavy elements like lead or uranium. As an example, Fig. 42 compares the X ray and the neutron radiographs of nuclear fuel rod simulators consisting of an aluminium cladding tube filled with lead pellets. Whereas no internal structure of the lead component is visible in the X ray radiograph details like pellet shape and boundaries can be studied in the neutron radiograph. Even the contrast of the spring is higher for neutrons than for X rays [see contributed paper by Liu et al].

Neutrons are sensitive not only to different elements but also to different isotopes. This provides the possibility to distinguish between the isotopes or determine the enrichment level for instance of $^{235}U/^{238}U$. The international cooperation in terms of highly irradiated materials is hindered by administrative problems caused by the transport of highly activated or nuclear materials abroad. Therefore, the cooperation in the framework of the CRP was focused on local research and use of on-site available materials at PSI, CIAE and LANL.

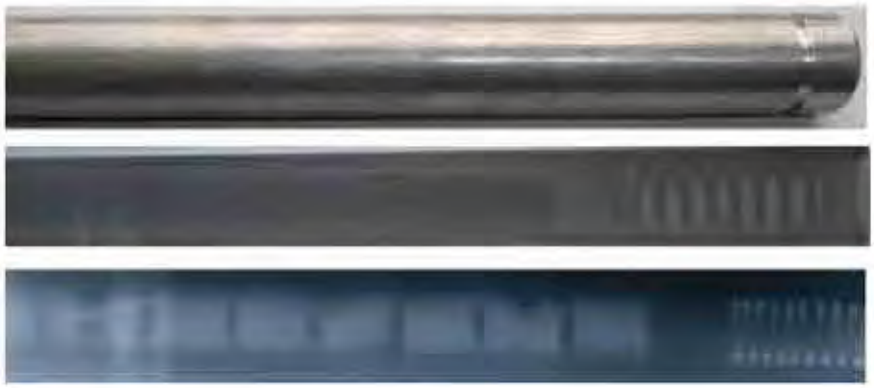

FIG. 42. The photo (upper), X ray image (middle) and neutron image (lower) of nuclear fuel elements taken at the CARR reactor at CIAE (China).

At PSI, SINQ target rods consisting of a Zircaloy cladding filled with lead were inspected before and after usage. While the inspection of the fresh rods can be done under normal conditions without any shielding requirements, the study of the highly activated samples requires much more care. To handle highly activated samples, the NEURAP shielding and positioning device was constructed. The NEURAP setup is a well shielded device where up to 5 single target rods are delivered from a hot cell and can be remotely-handled in the iron shielding block.

In addition to the shielding concept, there is another technique for obtaining the neutron images: Dy doped imaging plates operated in a special procedure. The resulting good image quality is demonstrated in Figs. 43a and 43b. It compares a rod before exposure to the proton beam (Fig. 43a) with a rod long-term exposed to the proton beam in the SINQ target (Fig. 43b). In the fresh target tube the molten inner part consisting of lead can be distinguished from the free volume and the Zircaloy cladding. In the long-term exposed rod the accumulation of spallation products follows the proton beam profile in the centre of the

rod. Some material changes like cracks, hydride blisters and the interaction with cladding become visible [see contributed paper by Lehmann et al.].

FIG. 43a. Pb target rod of SINQ before the exposure with the proton beam; the image was obtained in the routine imaging technique with Gd doped imaging plates.

FIG. 43b. Pb target rod after long-term exposure in the SINQ target; the image was obtained at the NEURAP facility by using Dy doped imaging plates within a special procedure.

Recent detector developments, achieved by the Univ. of California in Berkeley, allow for spatial and time-resolved neutron detection. This opens new avenues of characterization of nuclear materials and nuclear fuels in particular, as they enable isotope-sensitive imaging via so called neutron resonance absorption imaging. At LANL feasibility studies of energy-dispersive neutron radiography on an example of mock-up nuclear fuel rodlets were performed. Each rodlet consisted of five pellets prepared from uranium powder. They were characterized by energy-dispersive neutron radiography, and thermal neutron radiography. To simulate cracks and voids resulting from irradiation and burn-up in a fuel pin, plastic wire was embedded in the mock-up pellets which burned off during sintering leaving similar structures to voids and cracks. To assess the viability of detecting different isotopes, e.g. fission products, tungsten pieces of different sizes and shapes were embedded in several fuel pins. For example, an energy dispersive measurement at energies around the energy where tungsten shows an absorption resonance separates the specific tungsten containing features. It can be done for any other element with a suitable resonance. It seems that quantitative concentration measurements are possible after calibration. The ultimate goal of this work will be the characterization of irradiated fuel pins. Details of these investigations are published in [35].

2.5. OPTIMIZATION OF INSTRUMENTS FOR RESIDUAL STRAIN/STRESS MEASUREMENTS

Residual strain-stress measurement by neutron diffraction has been already established method in the case of development, characterization and testing of materials in many areas of industry. Therefore, it has also a close relevance to nuclear energy sector. Advanced neutron diffraction techniques and instrumentation for residual strain/stress measurements are always connected with possibly maximum usage and performance of neutron optics elements, namely, neutron guides, mirrors and super-mirrors and focusing monochromators in combination with position sensitive detectors. In this section, properties of the dedicated neutron strain/stress diffractometer installed at the beam port ST-1 of HANARO reactor in KAERI which has been designed as a result of cooperation between two CRP partners, namely KAERI Daejeon and NPI Řež, are described.

Thanks to the usage of the horizontally focusing bent perfect crystal monochromator, the optimization procedure and a choice a favourite neutron wavelength and total scattering cross-section, the resolution and namely a high luminosity of the instrument permit one to study kinetic processes in polycrystalline materials running within a few seconds. Equally, one is able to carry out residual stress measurements at the large depths of steel samples with a reasonable time.

The neutron strain/stress scanner evaluates the variations of lattice spacing within a sample with a spatial resolution of the order of mm^3 given by the dimensions of the gauge volume. Generally, neutron diffractometers, which are dedicated for strain/stress measurements, can be divided into two types: angular dispersive and time-of-flight instruments. Typical neutron diffractometer dedicated for strain/stress measurement at a reactor source is shown schematically in Fig. 44 [18, 36]. The polychromatic neutron beam is first monochromated to a chosen wavelength by diffraction from a suitable monochromator. This monochromatic beam of a suitable size and divergence is given by the use of appropriate beam defining elements and is then diffracted from the specimen. In a similar way, the geometry of the diffracted beam is shaped by suitable beam limitation devices, before it is captured by a neutron detector.

The gauge volume to which the strain measurement is related is given by the intersection of the incident and diffracted beams. Typically, neutron strain scanner is established on existing powder diffractometer. At the instrument of the first generation usually mosaic monochromator consisting of Cu, pyrolitic graphite or plastically deformed Ge are being used. As in the case of mosaic crystal monochromator there is no beam focusing, the uncollimated monochromatic beam spreads its cross-section at the place of the sample position up to tens of square centimetres. Then, the beam defining elements, which determine the gauge volume, bring a strong decrease of the final detector signal, while the resolution (*FWHM* of the diffraction profile) is still strongly influenced by the mosaicity of the monochromator β, of the order of tens of minutes of arc. Even in the optimum case, when the diffraction angles at the monochromator (θ_M), and the sample (θ) fulfil the following relation: $\tan\theta / \tan\theta_M = +1/2$, *FWHM* has a minimum value but still it is larger than β [37]. As can be seen from Fig. 44, the best geometrical choice corresponds to $2\theta = 90°$, when the gauge volume is in the form of a cube or rectangular prism. Consequently, it is required to have an intense Bragg peak at $2\theta \approx 90°$. However, in the conventional case, due to the required resolution, a large diffraction angle at the monochromator should be set. The current of the monochromatic neutrons impinging the sample is proportional to the wavelength spread $\delta\lambda = \lambda \cdot \Delta\theta \cdot \cot\theta_M$, where $\Delta\theta$ is the angular divergence of the beam. Therefore, the larger diffraction angle at the monochromator means the smaller neutron beam current and consequently, the smaller detector signal. However, the situation is completely different in the case of employing focusing bent perfect crystal (BPC) monochromator [38, 39], [see contributed papers by Carr et al. and Sutiarso et al].

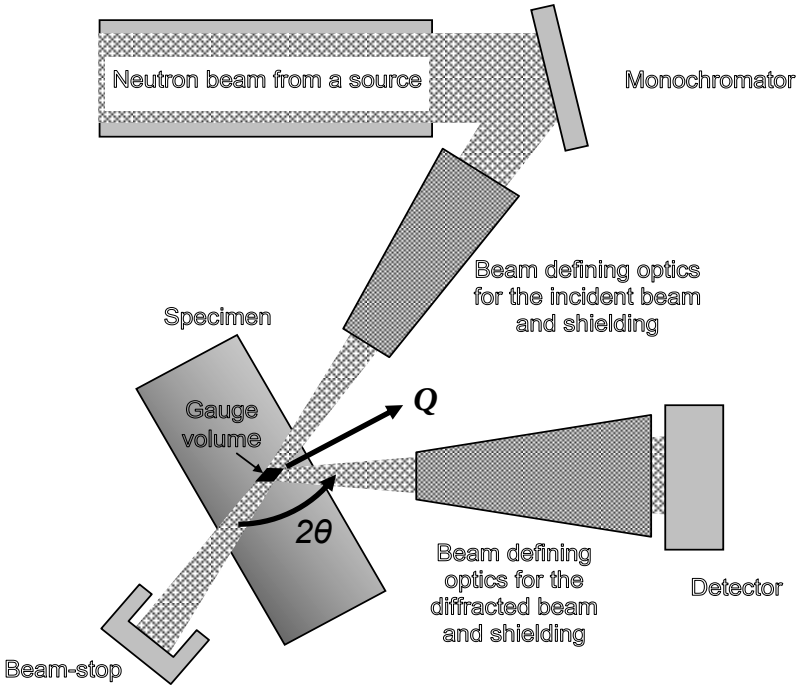

FIG. 44. Schematic illustration of a conventional reactor source based diffractometer dedicated for strain-stress measurement.

2.5.1. Focusing monochromator in the case of power diffration

Methodological background

A great advantage of the strain diffractometer equipped with the focusing BPC monochromator is very good predictability of its resolution and reflectivity parameters as has been many times demonstrated [40-41]. For imaging by a thin cylindrically bent crystal slab of the radius R, the lens formula $(f_a/a + f_b/b) = 1$ can be used. The parameters $f_{b,a}=(R\cdot\sin(\theta_{hkl}\pm\Psi))/2$ are the focal lengths on the image or object side, respectively, which are dependent on the cutting angle Ψ. Ψ corresponds to the angle of the diffracting lattice planes with respect to the surface of the crystal slab. Symmetric geometry means $\Psi = 0$. In practice, the monochromator-sample distance L_{MS} is fixed and should coincide with the image distance b ($b = L_{MS}$) of a point source A being at a distance $a = L_{AM}$ before the monochromator. For the parallel incident beam is valid that $L_{MS} = f_b$ and $a = \infty$. Then, for given θ_M and the bending radius R for any point of the sample, we arrive at the relation $a(R_M) = f_b/(1 - f_b/b)$, where $f_b = (R/2)\sin\theta_M$ is the focal length. Notice, that each point of the sample is reached by a convergent bunch of strongly α–λ–correlated rays according to $\Delta\lambda/\lambda = \Delta\alpha_1(1 - L_{MS}/2f_b)\cot\theta_M$.

This relation also points out that the smaller monochromator Bragg angle θ_M is used, the larger neutron beam current (the larger $\Delta\lambda/\lambda$) is delivered on the sample. However, this is connected with the fact that employing a smaller monochromator Bragg angle θ_M one obtains worsening of the instrumental resolution. Due to this fact, practically all existing neutron strain-stress scanners use monochromator Bragg angle, if possible, close to 90°. Typical

application of real space focusing is that the beam of a large cross-section is focused (e.g. from a thermal neutron guide) on a small sample.

Figure 45 shows a schematic diagram of the conventional diffractometer performance employing a BPC monochromator at a large Bragg angle (left) and the one designed and tested in KAERI using a small Bragg angle (right). The focusing diffraction performance consists then of the following steps.

Monochromatic neutrons selected by the bent crystal from a white spectrum are focused on a sample (real space focusing). There is a strong correlation between the divergence of the incoming and outgoing beams with respect to the monochromator, which can be easily manipulated by changing the bending radius R of the BPC monochromator. Then, by setting an optimum radius of curvature of $R = (2L_{MS}/\sin(\theta_M - \Psi))/(2\text{-}1/a_{SM})$ the divergence $\Delta\alpha_2$ achieves in the vicinity of the chosen scattering angle $2\theta_S$ of a minimum value making a high resolution as well as a highly luminous detector signal related to the corresponding Bragg reflection. The indices S and M mean that the corresponding parameters are related to the sample and the monochromator, respectively. It also means that in this optimum case the resulted divergence is not dependent on $\Delta\alpha_1$ and a large width W of the polychromatic beam irradiated the monochromator can be successfully used [42, 43].

These are unique properties of the focusing diffractometer performance making a simultaneous increase of the detector signal and the diffraction profile resolution (decrease of its *FWHM*). It means in practice that depending on the crystal curvature, the peak intensity and *FWHM* of the diffraction line achieve their maximum and minimum, simultaneously. The beam diffracted by a sample is then directly analysed by using a position sensitive detector (PSD).

As it is shown in Fig. 45, contrary to the conventional diffractometer performance with the mosaic monochromator, no Soller collimators which always cut the neutron current are required. Of course, there are some resolution uncertainties influencing the instrumental resolution which make the diffracted beam to some extent divergent [43]. They come from the effective mosaicity of the BPC-monochromator linearly dependent on the crystal thickness [44] and from the finite width of the irradiated volume of the sample determined by the input and output slits. Both uncertainties bring about the diffracted beam slightly divergent and directly determine the instrumental resolution. However, the effective mosaicity can be changed by decreasing the crystal thickness and to obtain a required instrumental resolution. Contrary to this case, in the conventional performance the required resolution is achieved by increasing the monochromator Bragg angle θ_M, while $\Delta\lambda$ spread of the monochromatised beam decreases [37]. Therefore, the use of smaller monochromator Bragg angle θ_M can considerably contribute to an additional increase of the instrument luminosity.

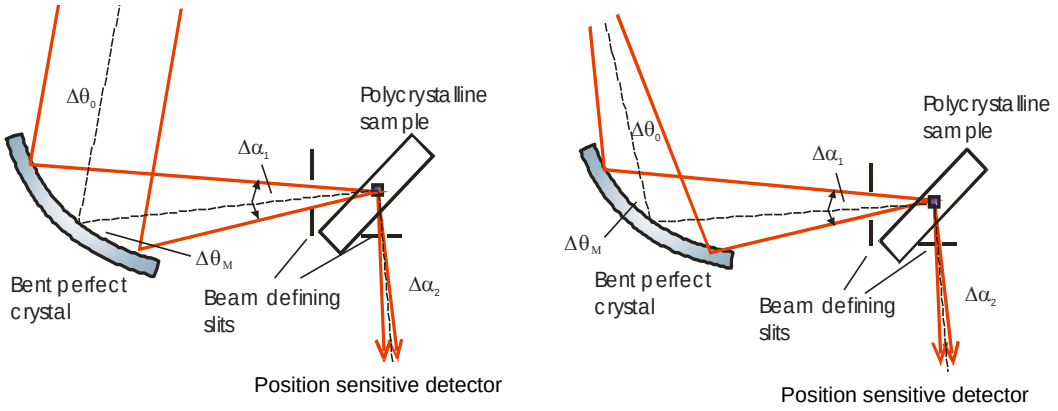

FIG. 45. Schematic geometry of the conventional diffractometer performance employing a BPC monochromator (left) and the one designed and tested in KAERI (right).

Experimental results

First, it was necessary to test the intensity and resolution behaviour of the diffractometer performance when using a small irradiated volume of a polycrystalline sample. For simplicity, instead of a bulk sample and beam defining slits we used an α-Fe(211) steel pin of 2 mm diameter and 40 mm height. By using a focusing Si(111) monochromator (cylindrically bent perfect crystal) set at $2\theta_M = 30°$, for $\lambda = 0.162$ nm the scattering angle on the sample was $2\theta_S = 87.8°$. In fact, several focusing diffraction geometries of the bent Si(111) monochromator were tested, both symmetric and asymmetric, and it was found that the symmetric one is the best alternative (for details see the paper [45]).

Figure 45 shows the behaviour of the required characteristics of the diffractometer on the monochromator crystal curvature. The results document the excellent property expected from the employment of the Bragg diffraction optics that the maximum luminosity is at the minimum of the resolution. Moreover, the resolution can be also optimized by a suitable choice of the thickness of the monochromator crystal slab (compare Figs. 46a and 46b) with an acceptable decrease of the detector signal.

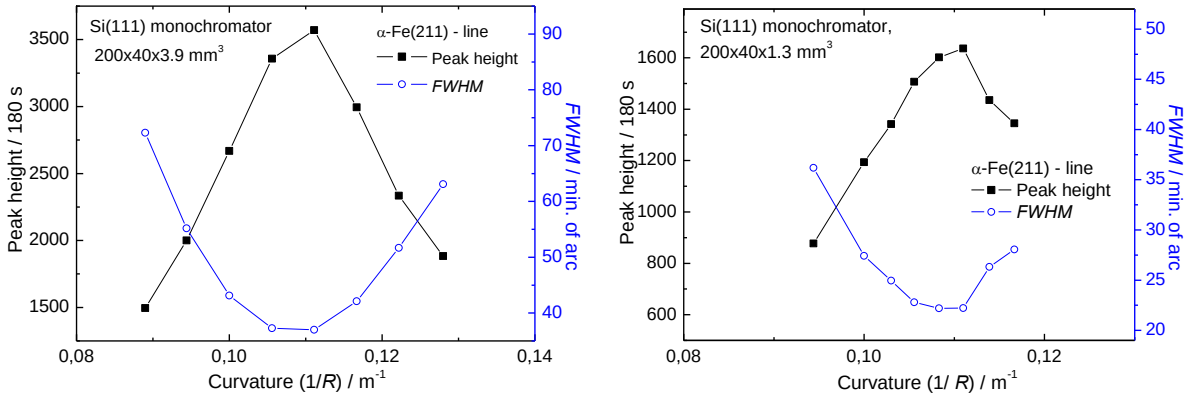

FIG. 46. The luminosity and resolution characteristics of the diffractometer performance with the focusing Si(111) monochromator of the thickness of 3.9 mm (a-left) and 1.3 mm (b-right).

Figure 47 displays the diffraction profiles of α-Fe(211) pin of 1 mm diameter and 40 mm height taken for different measurement times by the PSD at the distance of 120 cm from the sample. Smaller diameter of the sample has practically no influence on the *FWHM* of the diffraction profile, because the spatial resolution of the detector was 2.5 mm (the angular width of one channel was 0.0095°) as well as the uncertainty $\Delta\alpha_{2t}$ were much larger. It is clear that by using a PSD having better spatial resolution, it could be set closer to the sample. In this case we used deliberately only 1 mm diameter pin as a sample and followed the value of the detector signal and the error in determination of the peak position. If we take into account that about 40 channels correspond to the angular range corresponding to *FWHM,* even at the measurement time of 5 s the peak position can be determined with a relative error of about 10^{-4} which is sufficient in most cases of residual strain/stress measurements. It follows from these facts that thanks to very good luminosity and resolution the new instrument performance permits also studies of some kinetic processes related to macro- and/or micro-strain/stress distribution. Namely, so called *in-situ* experiments with samples subjected to external thermo-mechanical load can be attractive. In such cases much larger gauge volume is usually used which would permit to make the measurement time of the diffraction profile even shorter because the detector signal is roughly proportional to the irradiated volume of the sample.

2.5.2. Use of wavelength-dependent attenuation on neutron diffraction stress measurements at depth in steels

Change of neutron transmission at the Bragg edges

In this paragraph the results of systematic investigations of the wavelength dependence of maximum feasible penetration depth for neutron stress measurements in steels are presented. For these measurements, the wavelengths from the close vicinity of the Bragg edges where the neutron total-cross section has local minima and for which the scattering angles are convenient for stress measurements are used. By using such wavelengths (e.g. 0.24 nm which are longer than commonly used $\lambda \approx 0.16$ nm for strain-stress instruments) and focusing bent perfect crystal Si(111) monochromator, a maximum available path length of about 85 mm in ferritic and austenitic steels was achieved. The following results provide useful information for a choice of the instrument configuration which would be most suitable for particular measurement tasks.

For residual strain-stress measurement in thick samples having a non-negligible attenuation (as for example in steels) a decisive role plays neutron beam current delivered on the sample. Another effective and complementary way to increase the maximum available path length in the sample is to exploit the wavelength dependence of the neutron total cross-section in order to minimize the attenuation factor of the material. This method can be realized on the instrument installed at a continuous neutron source when choosing the reflections with a wavelength near the Bragg edge, where the neutron total cross-section is minimal. However, for the chosen wavelength and reflection, the scattering angle ($2\theta_S$) can differ from 90°, so that the section of the gauge volume is distorted from a square shape to a less symmetric diamond shape. But for thick components the distortion is usually acceptable to some extent, especially as it allows substantial increases in the available depth.

Figures 48 and 49 show the calculated total neutron cross-section of the ferritic and austenitic steels, respectively [46]. Indices (hkl) of several Bragg edges and corresponding wavelengths are shown at the top. Scattering angles of reflections corresponding to the

wavelength at Bragg edges are shown at the bottom. In ferritic steel, as shown in Fig. 47, there are Bragg edges at λ = 0.135, 0.153 and 0.234 nm, near which the total cross section has its local minimum. The corresponding scattering angles of the 211 or 110 reflections, which are not much different from 90°, are acceptable for the stress measurements. Since the lowest minimum is located near the (211) Bragg edge at λ = 0.234 nm, this wavelength has appeared as a good candidate for stress measurements at the depth using the 110 reflection. The corresponding scattering angles of the 211 or 110 reflections, which are not much different from 90°, are acceptable for the stress measurements. Since the lowest minimum is located near the (211) Bragg edge at λ = 0.234 nm, this wavelength has appeared as a good candidate for stress measurements at the depth using the 110 reflection. It should be pointed out that measurements at depth with the wavelength corresponding to the exact Bragg edge can cause an additional 'artificial' peak shift and can deteriorate the quality of the obtained strain/stress results. Since attenuation depends on the neutron wavelength, the mean value of the wavelength distribution of the neutron beam, which defines the position of a diffraction peak, changes with path length.

At a Bragg edge, where attenuation significantly changes with wavelength, it can generate a remarkable diffraction peak shift, corresponding to apparent strains at depth. It is difficult to compare the maximum available penetration path lengths among the conditions with different wavelengths only by calculation because the total cross-section and the other parameters (e.g. instrumental and source parameters) are correlated with the wavelength. Therefore, the maximum penetration path length near the Bragg edges at λ = 0.135 nm, 0.153 nm and 0.234 nm in ferritic steel (low-carbon steel, ~0.2% C) was measured experimentally. Following the considerations mentioned above, similar experiments were also carried out in austenitic steel (stainless steel 304L) with the wavelengths near the Bragg edges at λ = 0.122, 0.147, 0.166, 0.218 and 0.255 nm (see Fig. 48). In this case the austenitic steel showed minima of the total neutron cross-section located at long wavelengths near λ = 0.22 nm and short wavelengths in the vicinity of λ = 0.16 nm. For a more comprehensive study, some other wavelengths from the close vicinity of the Bragg edges were tested as well. Since the instrument was set at $2\theta_M$ = 45° for routine operation, the results with the wavelengths corresponding to this take-off angle were also compared.

It has to be mentioned that the steps in the neutron transmission at the Bragg edges of the material provides the possibility of strain imaging too. To achieve such strain imaging neutron radiography or tomography measurements have to be performed with sufficient wavelength resolution. Indeed, it can be obtained by the application of wavelength selectors or double crystal monochromators at stationary neutron sources or by the application of short pulsed sources. In this case the time structure of the intensity provide inherent a high wavelength resolution. Such types of radiography experiments are a very common methodical development on the field of neutron imaging.

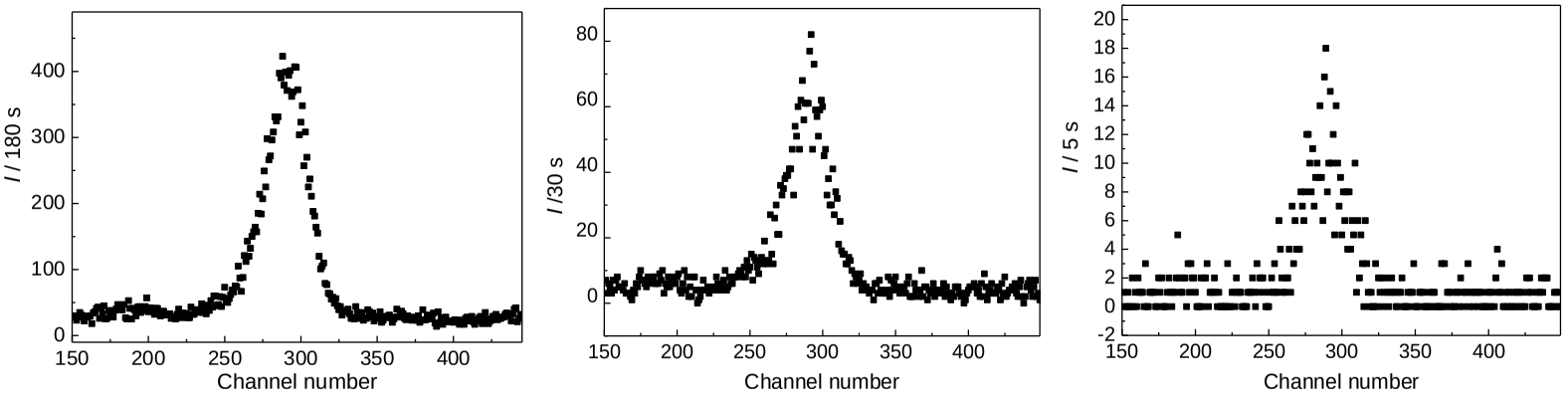

FIG. 47. Diffraction profiles of the sample of α-Fe(211) pin of 1 mm diameter and 40 mm height for different measurement times of 180s, 30s and 5s.

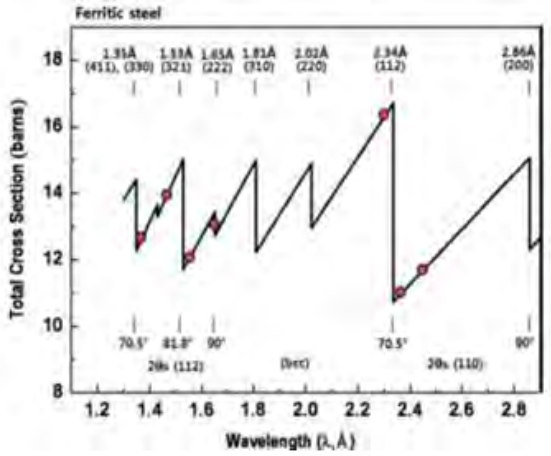

FIG. 48. Calculated total neutron cross-section of the ferritic steel (low-carbon steel, b.c.c.) as a function of the neutron wavelenghts. The wavelenghts corresponding to the filled circles were used in experiment.

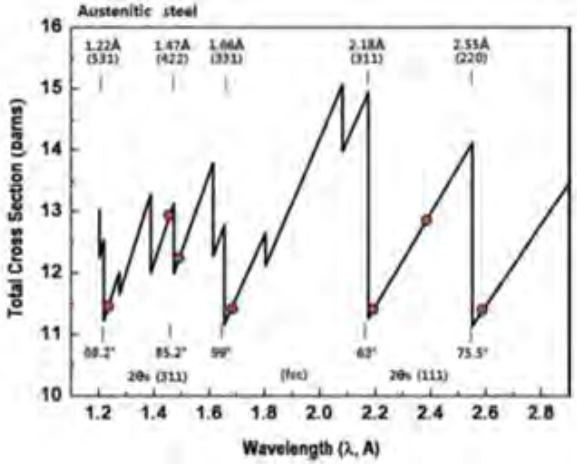

FIG. 49. Calculated total neutron cross-section of the austentic steel (stainless steel 304L, f.c.c.) as a function of the neutron wavelenghts. The wavelenghts corresponding to the filled circles were used in experiment.

Experimental verification

The related experiments were carried out on a reconstructed stress instrument at the HANARO reactor in KAERI Daejeon. Figure 50 shows the experimental geometry in the vicinity of a sample with the parameters used in the text. Figure 51 shows the diffraction peaks that were measured at the maximum available depth in ferrite steel (24 mm depth, $2\theta_S = 72.1^o$, $\lambda = 0.239$ nm) and austenite steel (22 mm depth, $2\theta_S = 63.8^o$, $\lambda = 0.219$ nm). It is obvious that the diffraction peak is about three times higher than the incoherent background. Figure 51 shows the dependence of the strain error on the total penetration path length by measuring the 211 reflection for 0.136 and 0.155 nm and the 110 reflection for 0.228 and 0.239 nm in the case of the ferritic steel and the 311 reflection for 0.124 and 0.15 nm and the 111 reflection for 0.239 and 0.261 nm in the case of the austenitic steel. The following Table 7 shows maximum penetration depths in reflection (D_{ref}) and transmission (D_{tr}) geometries for different wavelengths in ferritic austenitic steels as obtained from the experiment. The maximum available path length, $\lambda = 0.239$ nm) and austenite steel (22 mm depth, $2\theta_S = 63.8^o$, $\lambda = 0.219$ nm) [see contributed paper by Mikula].

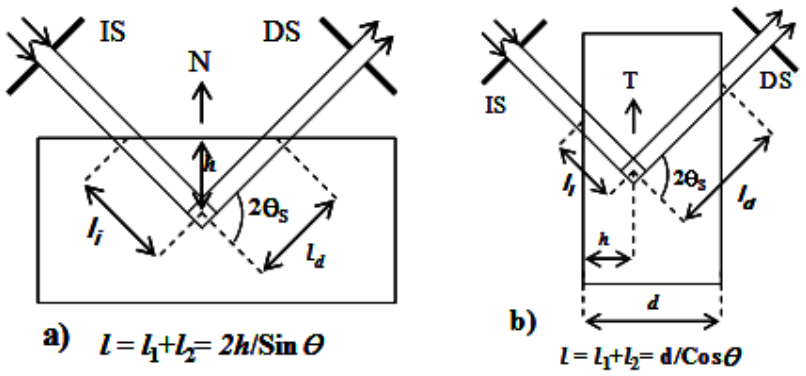

FIG. 50. The gauge volume is defined by slits in the incident (IS) and diffracted (DS) beams. The totalneutron path length l_m is the sum of that for incident (l_i) and diffracted (l_d) beams.

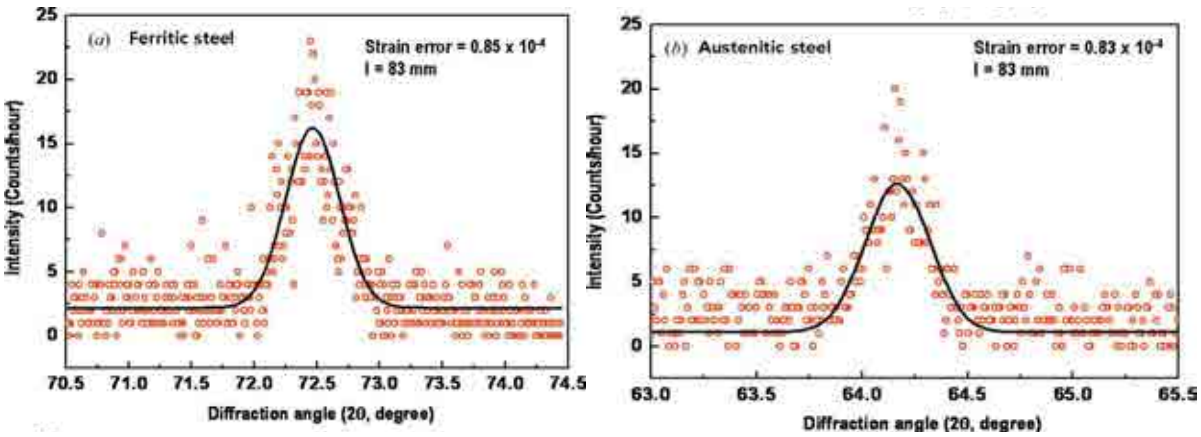

FIG. 51. 110 and 111 diffraction peaks as measured in the reflection geometry for the ferritic and austenitic steels, respectively as measured at 83 mm total path length (1 h measurement time, 80 mm^3 gauge volume).

Figure 52 shows the dependence of the strain error on the total penetration path length by measuring the 211 reflection for 1.36 Å (we remind the reader that 1 Å = 0.1nm) and 1.55 Å and the 110 reflection for 2.28 Å and 2.39 Å in the case of the ferritic steel and the 311

reflection for 1.24 Å and 1.50 Å and the 111 reflection for 2.39 Å and 2.61 Å in the case of the austenitic steel.

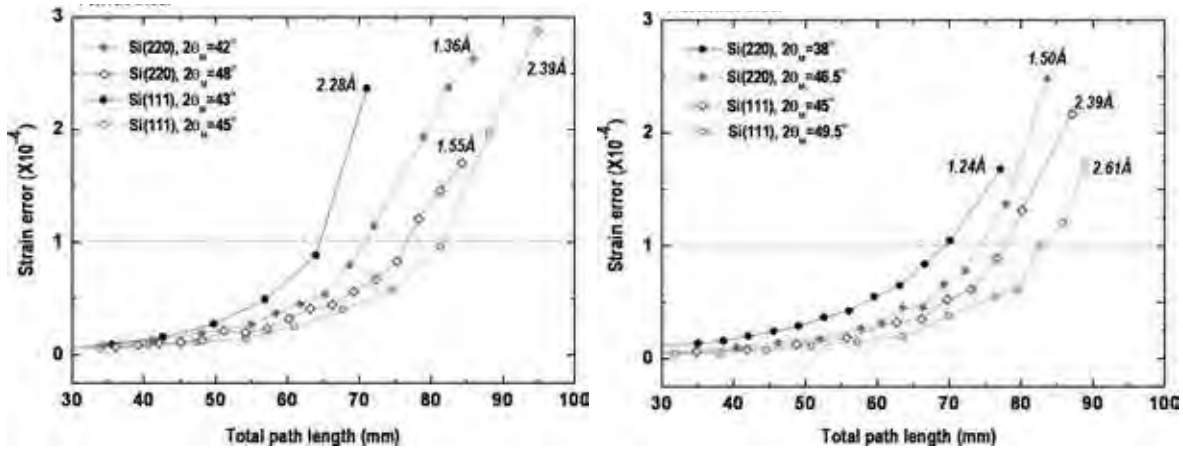

FIG. 52. The dependence of the strain error on the total penetration path length in the ferritic (on the left) and austenitic steels (on the right). The scan was carried out in the reflection geometry (1 h measurement time, 80 mm^3 gauge volume).

Table 7 shows maximum penetration depths in reflection (D_{ref}) and transmission (D_{tr}) geometries for different wavelengths in ferritic austenitic steels as obtained from the experiment. The maximum available path length, l_m, was defined as path length corresponding to the strain error of 10^{-4} in strain determination.

TABLE 7. THE VALUES OF l_M, D_{ref}, D_{tr} AND FoM AS DETERMINED FROM THE EXPERIMENTAL DEPTH SCANS

Ferretic steel (low carbon steel, *bcc*)								
Monochromator	$2\theta_M$ (deg)	λ (nm)	Reflection plane	$2\theta_S$ (deg)	FoM	l_M (mm)	D_{ref} (mm)	D_{tr} (mm)
Si(220)	42	0.136	(211)	71.2	73	71	21	58
Si(220)	45	0.146	(211)	77.1	82	68	21	53
Si(220)	48	0.155	(211)	82.9	105	77	26	58
Si(220)	51	0.165	(211)	90.1	119	68	24	48
Si(110)	43	0.228	(110)	68.5	90	64	18	53
Si(110)	45	0.239	(110)	72.1	100	83	24	67
Si(110)	43	0.244	(110)	73.8	84.5	80	24	64
Austenitic steel (stainless steel 304L, *fcc*)								
Monochromator	$2\theta_M$ (deg)	λ (nm)	Reflection plane	$2\theta_S$ (deg)	FoM	l_M (mm)	D_{ref} (mm)	D_{tr} (mm)
Si(220)	38	0.124	(311)	69.6	54	70	20	57
Si(220)	45	0.146	(311)	85.6	93	72	24	53
Si(220)	46.2	0.150	(311)	87.8	120	75	26	54
Si(220)	53.2	0.171	(311)	104.0	148	76	30	47
Si(110)	41.2	0.219	(111)	63.8	97	87	23	74
Si(110)	45	0.239	(111)	70.1	91	79	23	65
Si(110)	49.5	0.261	(111)	78.0	100	83	26	65

Note that l_m were determined from the depth scans for 80 mm^3 gauge volume and 1 h measurement time. The figure of merit (*FoM*) was calculated by using the integral intensity (*I*) and peak width (*FWHM*) of the diffraction peak from the powder samples (80 mm^3 gauge

volume, 300 s measurement time). *FOM* for ferrite and austenite were set to be 100 for the wavelengths 0.239 nm and 0.261 nm, respectively, the values of which correspond to the lowest total cross-sections in ferrite and austenite.

It can be seen from Table 7 that the maximum available path length of 83 mm in ferritic steel was achieved at $\lambda = 0.239$ nm near the α-Fe(211) Bragg edge at 0.234 nm where the cross-section is lowest. It is clearly demonstrated that a small variation in the wavelength from 0.228 nm to 0.239 nm increases the maximum available path length by 19 mm. Like in ferrite the longer path lengths in austenite were achieved at longer neutron wavelengths by using Si(111) monochromator for γ-Fe(111) reflection. The maximum available path length $l_M = 87$ mm was achieved at $\lambda = 0.219$ nm near the 311 Bragg edge. It is clear that the information about maximum available depths in reflection and transmission geometries as provided in Table 7 is useful for a choice of the instrument configuration which could be most suitable for a particular sample.

After a detailed inspection of the obtained advantageous instrument performances, the new concept was tested on strain-stress neutron diffraction scanning in a 50 mm thick ferritic steel weld (see Fig. 53). The most promising neutron wavelength of 0.230 nm has been applied. Note that residual stresses are not measured directly by diffraction methods but they are determined from measurement of residual strains, which are then converted to stresses using appropriate modelling [18, 36].

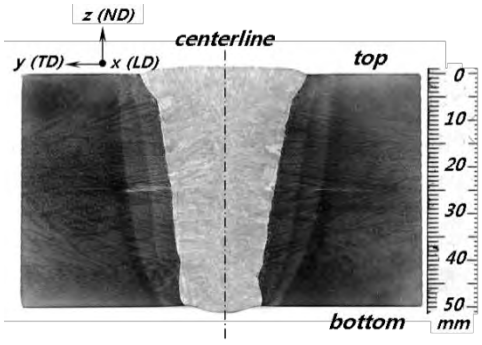

FIG. 53. Macrostructure of the 50 mm thick low-carbon steel weld. Note the following notation: LD (longitudinal, x), TD (transverse, y), and ND (normal, z) directions of the weld plate.

Figure 54 shows the through-thickness variations of residual stresses along the four different locations from the weld centreline using neutron diffraction. Note that the obtained stress uncertainties were mostly about ±30 MPa, which is similar to the typical accuracy of e.g. the deep hole drilling method. Figure 55 shows the cross-sectional mapping of the longitudinal residual stresses σ_x in the 50 mm thick steel weld specimen. It was reconstructed based on the all data points shown in Fig. 54. For more details about the instrument performance as well as some other experimental results see the references [46-48].

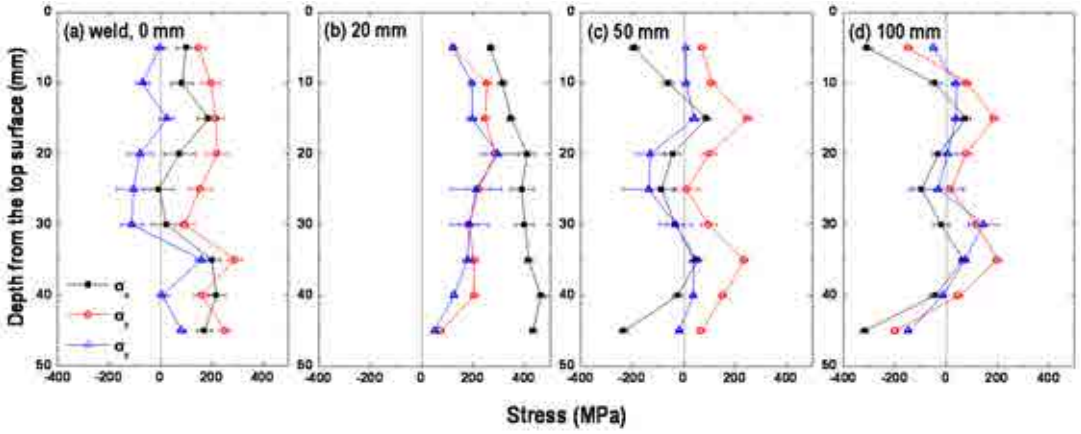

FIG. 54. Through-thickness variations of the macroscopic internal stresses (σ_x, σ_y, σ_z) in a 50 mm thick ferrite steel weld plate specimen: (a) 0 mm, (b) 20 mm, (c) 50 mm, and (d) 100 mm distance from the weld centerline.

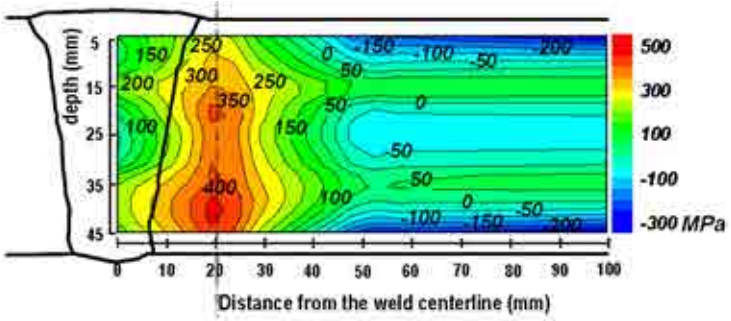

FIG. 55. Two-dimensional mapping of the longitudinal residual stress (σ_x) in the 50 mm thick weld plate.

2.5.3. Summary

New concept of a world class neutron diffractometer equipped with a two dimensional position sensitive detector (2 mm spatial resolution) dedicated to residual strain stress scanning operating at the HANARO reactor in KAERI Daejeon has been presented. It exploits Bragg diffraction optics as well as non-regular behaviour of total neutron cross section of polycrystalline materials. Unique instrument parameters, namely, neutron current delivered on the sample, instrument resolution and the detector signal related to the chosen diffraction profile, have been tested on steel samples. Then through-thickness distributions of the macroscopic residual stresses were successfully determined in the 50 mm thick steel weld plate using neutron diffraction. New configuration provides the significantly increased monochromatic neutron current and successfully exploits decreased beam attenuation and strain uncertainties compared to the conventional methods. The total beam path length over 80 mm was accessible with ±100 micro-strain uncertainty, 2 mm spatial resolution along depth, and one hour measurement time, which is suitable for the precise strain analysis. Moreover, new instrument performance permits to study some kinetic processes in polycrystalline materials running within a few seconds. Some improvements are still possible e.g. by installing horizontally and vertically focusing monochromator and a position sensitive detector of a better spatial resolution. As the vertical focusing has no influence on the resolution of the instrument, its future installation could improve the luminosity by a factor of 2-3.

2.6. EFFORTS TOWARDS STANDARDIZATION OF NEUTRON IMAGING

Digital thermal neutron imaging mainly consists of radiography (2D imaging) and tomography (3D imaging), including other special techniques using neutrons as a probe. Neutron radiography is the process whereby the transmitted intensity of neutrons through a specimen using a position sensitive detection system is detected and recorded, which results in 2D images called radiographs. Neutron tomography is the process whereby a 3D virtual image (tomogram) is obtained through the reconstruction of many radiographs (2D – projections) being obtained by turning the object through many discrete angles. To generate high quality tomograms, the rotation angle range required in the case of parallel beam geometry is $0 \leq \Omega < 180^{o}$. For the determination of the rotation center a range of $0 \leq \Omega \leq$ at least 180^{o} has to be applied. Measurements at angles of $0 \leq \Omega < 360^{o}$ are needed in the case of cone beam geometry. In both, parallel and cone beam geometries, the sample should always be fully illuminated within the field of view (FOV) of the detector.

Internationally, the use of neutron computed tomography (NCT) as analytical probe on routine basis is being perceived as a relative undeveloped method compared to X ray tomography. Until today, little effort was made to compare the performance of different neutron imaging instruments in a controlled and standardised manner. Since every neutron tomography installation is unique in quality and performance due to e.g. the spectrum of neutrons, different power of neutron sources, different experimental set-ups and layout, competence and expertise of operators with regard to setup and image processing, etc., the need for standardisation becomes very important to effectively compare neutron imaging facilities and their performance with respect to each other.

For X ray tomography, used for example for medical imaging, there are quality assessment methods developed and available to certify the quality of the delivered images. Digital radiography (DR), computed radiography (CR) and tomography with X rays (XCT) as a source of penetrating radiation have found applications ranging from medical diagnostics and quality assurance in industry but also a tool for materials research. These imaging analytical techniques have gained acceptance because they are non-destructive and their output are images in real space enabling a direct comparison e.g. to construction drawings.

Because these setups provide results which lead to quality related decision making or diagnosis of an abnormality, it is necessary to qualify the performance of setups using test objects with known and well defined features. It is for this reason that the performance of the setup should be assessed and quantified, to determine the capabilities of the setup with regard to key performance factors. Similarly, neutrons are penetrating radiation with often better penetrability than X rays for most metals and heavy materials (and have high interaction for water and plastics) and a converse contrast. Neutron imaging has proven usefulness with applications ranging from fuel cells, petroleum, mineralogy, welds, and porous media to magnetic systems. Hence there is also the need to characterize (assess and quantify) the performance of neutron setups before they are applied.

Accurate and precise characterization involves adequate human subjectivity (with regard to image sampling and assessment), key performance factors identification, and well derived, designed and implemented performance metrics. Eliminating human subjectivity ensures that the results can be repeated and are precisely and accurately quantified.

This can be achieved by implementing automated systems for sample setup, data processing and analysis as well as quantification of the resulting data. Defining all factors affecting the setup performance of neutron computed radiography and tomography is very important. These factors eventually have to be minimized to key performance factors to establish practical characterization of a neutron imaging facility and its outcome (radiographs and tomograms).

2.6.1. Test objects

Schematic diagrams of standard samples suggested for contrast and spatial resolution assessment are shown in Fig. 56.

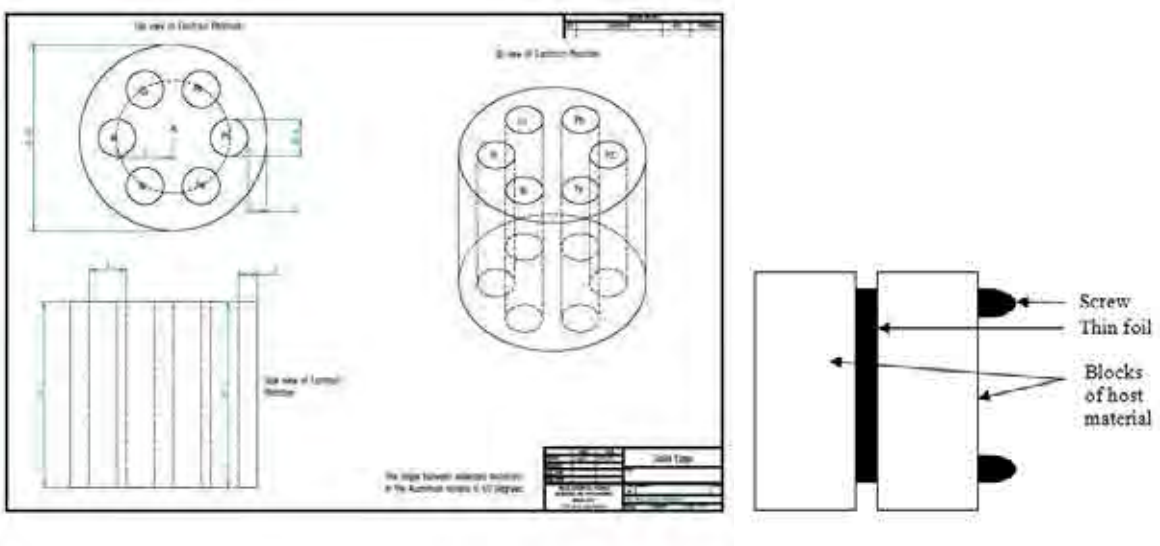

FIG. 56. Design of the NTC standard created by KAERI (on the left). Unless otherwise specified dimensions are in millimetres; side view of the NTSR standard design created by PSI (on the right).

The design of the Neutron Tomography Contrast (NTC) standard sample proposed by the Korean Atomic Energy Research Institute (KAERI) is shown in Fig. 56(a). This NTC sample consists of 6 mm diameter cylinders made of Al, Cu, polyethylene (PE), Ni, Pb and Ni embedded in an Al cylinder of 30 mm in diameter. The Al cylinder was added to verify if edge enhancement effects would appear at the interface between the two components.

A set of 2 x Neutron Tomography Spatial Resolution (NTSR) samples were designed and manufactured by NIAG at Paul Scherer Institut (PSI) in Switzerland. Each sample is made of two solid blocks (matrices of Al or Fe, respectively) with dimensions of 10 mm x 20 mm x 40 mm and fixed together by a set of screws, one at the bottom and one at the top. The space between the two blocks is maintained by a stack of 0.02 mm thick foils placed between them acting as spacers. The dimensions of the spacers are 20 mm x 20 mm x (multiple 0.02 mm layers). The foil materials are chosen to have a complementary attenuation to the supporting matrices, i.e. Al is used within Fe blocks and Cu is used within Al blocks. The side view of the general design of the phantoms is shown schematically in Fig. 56(b).

The evaluation methods for the two sample types are thoroughly discussed in the paper by Kaestner [49] that describes the acquisition conditions and the evaluation procedures in a first approximation. Based on the experiences of the first Round Robin exercise, an

improvement of the test sample and update of the evaluation procedure is proposed (see paragraph 2.6.4).

2.6.2. Round Robin exercise

Five sets of neutron imaging test samples were manufactured to evaluate the proposed sample designs. One sample was kept at Paul Scherrer Institut as reference sample. The remaining four sample sets were sent to different institutes who enrolled to participating in the evaluation procedure. The samples were always returned to PSI for data upload and refreshing the contents of the boxes.

This report summarizes the results from the Round Robin evaluation made during 2012/2013. The Round Robin sample evaluation included experiments at 13 facilities worldwide. The involved institutes are marked on the map in Fig. 56 below. The time for a laboratory to complete an experiment and return the samples was between two and four months. This delay in many cases was caused by problems with the customs that did not accept the samples as non-commercial and intended for research purposes only. Additionally, the arrival of the samples may not always have fitted in the beam time agenda which delayed the experiment further. The current status of the experiment is shown in Fig. 58.

FIG. 57. Institutes participating in the first Round Robin evaluation of the QA samples. The red pin marks PSI-Switzerland, in charge of coordination of the Round Robin.

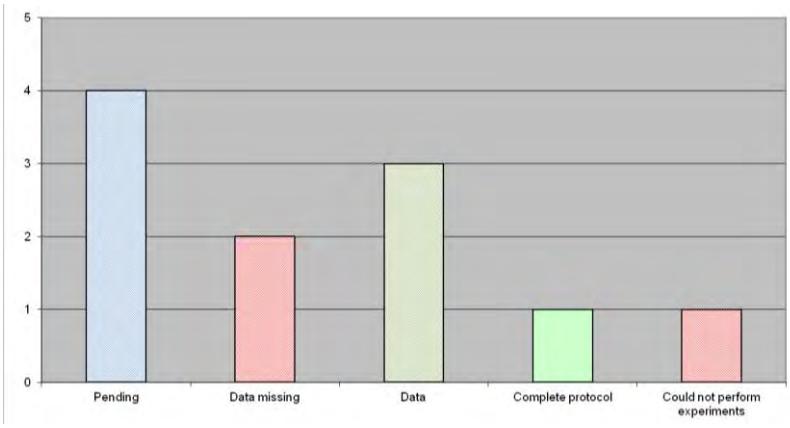

FIG. 58. Status of the Round Robin exercise.

2.6.3. Results

A quantitative and qualitative evaluation is made of all the data sets of the contrast sample and the spatial resolution sample that was returned to PSI by participants after completing the protocol.

Contrast (Using NTC phantom)

The intensity of the slice images from the tomograms of the contrast phantoms first needed to be adjusted since most of the returned data was scaled in the wrong way. Fortunately, the intensity scaling parameters are provided in the image files. The slices and their histograms in Fig. 59 show that most sources have a similar (thermal) spectrum. ICON at Paul Scherrer Institut and the Hungarian results deviate, which is to expect since these were the data from a cold source spectrum. In some cases the image intensity was too hard clipped, which resulted in wrong intensity readings, especially the PE inset was suffering from this clipping. The purpose of the intensity clipping was most likely to improve the visual contrast of the remaining insets.

The returned data also show that there are large variations in field of view (FOV) among the contributed laboratories. This has a direct impact on the pixel sizes which can be seen in Table 8. The size of the phantoms turned out to be adequate for most facilities, but in some cases the FOV was either so large that there were on few pixels for each inset or the FOV was so small that the entire sample could not fit in the radiograph. The latter is not good since the reconstructed data will suffer from truncation artefacts on the boundaries where the sample extends beyond the FOV supported by the detector. However, if the truncated region is moderate and a decent reconstruction tool is used, this artefact may be alleviated.

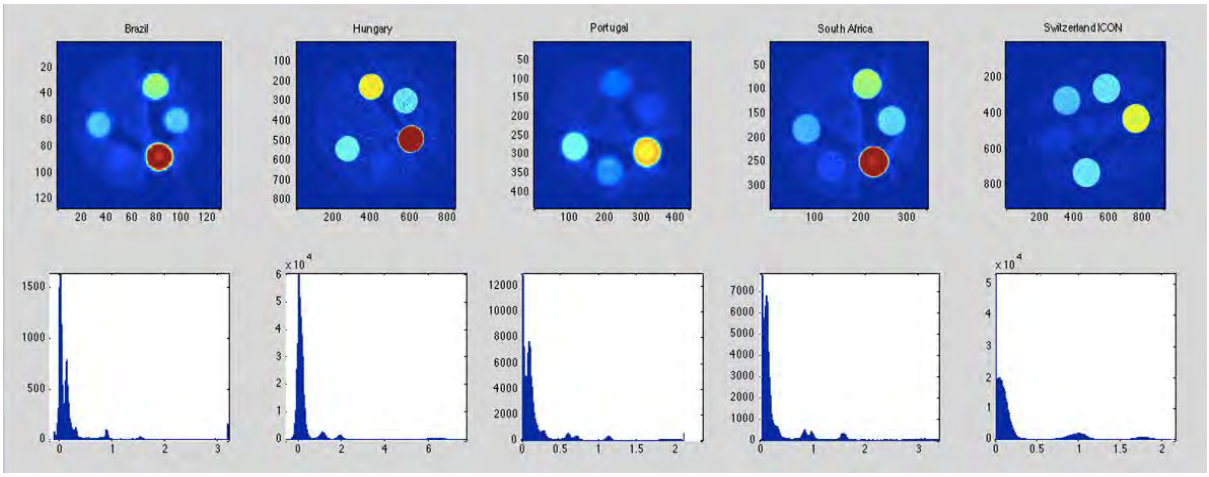

FIG. 59. Contrast images returned from five different facilities. The slice from ICON, Switzerland, was measured using a revised sample with Ti replacing PE. The top row represents the horizontal slices in the middle of the object, while the lower row shows histogram data.

The most important finding was that the PE insertion is attenuating the beam so much that the remaining intensity is insufficient for a correct reconstruction of the projection data. These so called starvation artefacts occurred mainly in combination of PE and Fe, Cu, and Ni.

The artefacts results in wrong intensity values for the involved insets. In general, a lower intensity is expected in the presence of starvation artefacts. The solution to this problem is to replace the PE insert by Ti, which has attenuation in the magnitude of Fe and Cu for thermal neutrons.

TABLE 8. PIXEL SIZES USED AT DIFFERENT FACILITIES TO PERFORM THE IMAGING EXPERIMENTS

	Brazil	Hungary	Portugal	South Africa	Switzerland
Pixel size [μm]	273	47.6	81.0	97.7	43.7

Spatial resolution (NTSR)

NTSR samples show the effect of the large variation in the pixel sizes. The number of inserted foils was directly connected to the pixel sizes obtained at the various facilities. This is an expected outcome for the property that was intended to be investigated. In most cases the estimated thickness deviated by 2-3% from the expected film thickness (Fig. 60 and Table 9). This must be considered as a good result. The data that deviated severely from the expected value were from South Africa, where a malfunctioning sample manipulator caused difficulty in the acquisition of the radiographs in equal step increments.

The sample profile in all cases but one are clearly cupped. This is an expected result since it is caused by the scattered neutrons. The cupped profile makes the evaluation more difficult. It still needs to be clarified which base line to use when the intensity difference is computed. Using the wrong base line will introduce an error in the thickness estimation which is based on full width half maximum (FWHM) approach on an average profile computed from several lines across the gap.

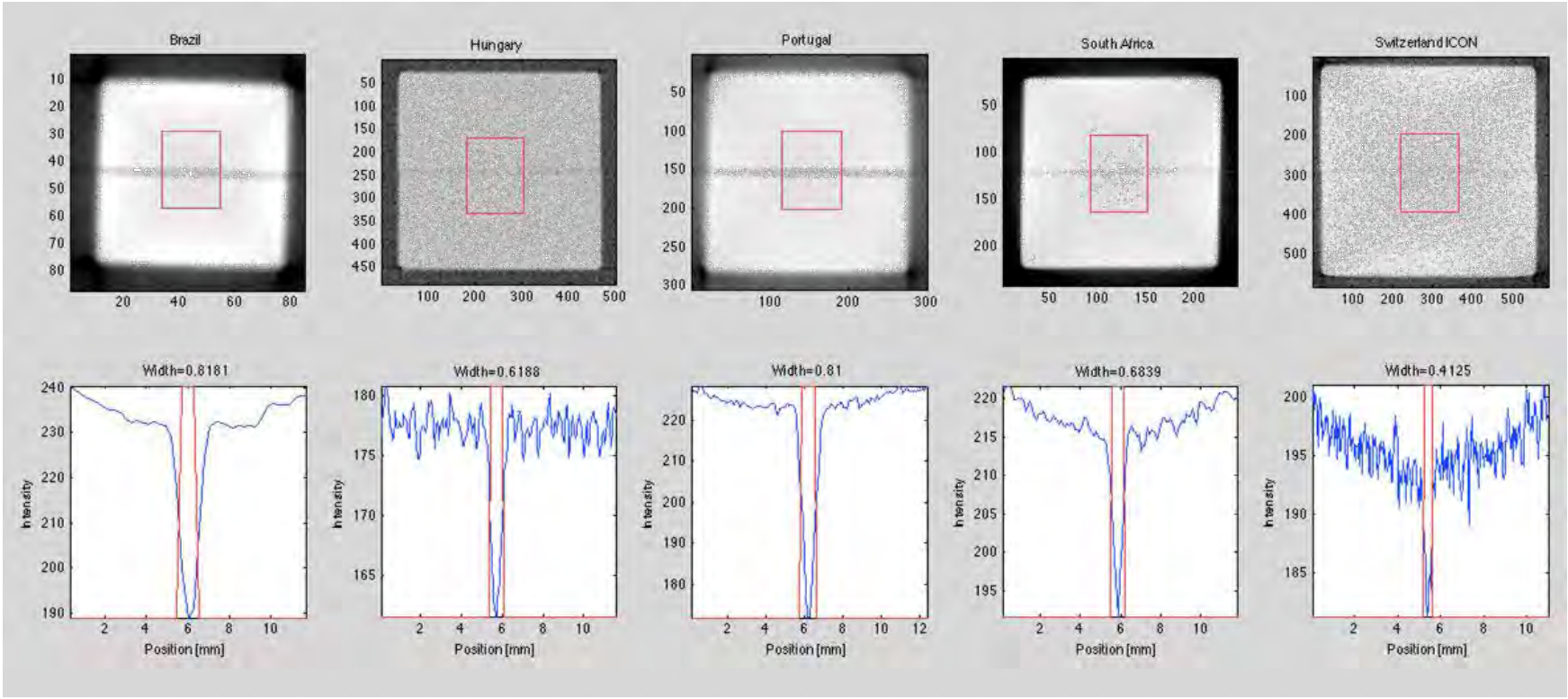

FIG. 60. Slice images of the resolution sample returned from five different facilities. The profile plots are averaged using profiles extracted from the red box marked in each slice.

TABLE 9. SLIT WIDTHS ESTIMATED FROM THE RECONSTRUCTED SLICE IMAGES

	Brazil	Hungary	Portugal	South Africa	Switzerland
Foils	4	3	4	3	2
Width [mm]	0.82	0.62	0.81	0.68	0.41
Deviation [%]	2.50	3.33	1.25	13.0	2.50

2.6.4. Proposed improvements

Samples

The current set of samples is intended to quantify the performance of neutron computed tomography. This is an advanced discipline in neutron imaging and not every international neutron-imaging instrument provides this option of analytical capability yet. The evaluation of the NCT sample also includes several steps to complete, e.g. acquisition of the projection data and reconstruction of the virtual volume dataset.

The basic information for any advanced neutron imaging technique (computed tomography, energy selective imaging, diffraction imaging and grating interferometry) is a set of neutron radiographs. Therefore, it is relevant to provide a set of samples that quantifies basic quality features of the radiograph. Relevant phantoms to investigate are step wedges of different materials to investigate the contrast and line pair masks, knife-edges, and Siemens star phantoms to investigate the resolution. The signal-to-noise ratio also provides relevant information that has an impact on the overall image quality and performance of a radiography facility. Noise propagates through every step of processing and can best be removed by increasing the neutron statistics of the image. With this set of phantoms a suite of evaluation methods are available and can be applied to quantify the radiographs and tomograms and thus the capability of the radiography facility.

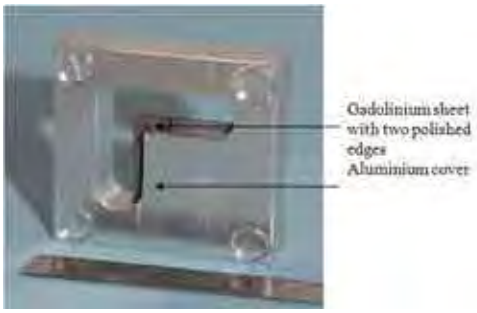

FIG. 61. The 2D edge test object.

With knowledge gained from the first Round Robin exercise and the utilization of the phantoms described, a new set of phantoms is under design including their scientific justification. Among these are phantoms for the evaluation of 2D contrast, 2D edge evaluation according to [50], 3D edge evaluation and improved 3D contrast testing. A preliminary 2D edge test phantom (Fig. 61) has been designed, manufactured and is under evaluation. A proposed automated analysis based on Matlab being designed and is under evaluation in order to analyse radiographs of the 2D Edge test object.

Evaluation procedure

Robust automated image evaluation routines are required to assure that the measured images are evaluated in a repeatable manner and that the impact of human interaction is minimized. The method proposed for the contrast sample in [49] can be considered robust. It is important that the evaluation methods are provided with a user interface that makes the evaluation intuitive. The resolution sample currently does not have a comparable evaluation procedure and has to be developed. Ideally, an analytical tool that directly delivers an evaluation report has to be developed. The exact outline and content of an evaluation report still needs to be determined. This report would then replace the current Excel spreadsheet.

For future experiments, it recommended to divide the Round Robin exercise in two parts. One part intended for phantom development and refinement of evaluation procedures and a second, more extensive, part to evaluate the proposed procedure. In the first part only few laboratories are included to keep the loop short and also to reduce the shipment costs. The second part should be open to any laboratory interesting in participating in the evaluation of the procedure. For this part a general invitation should be sent to all neutron-imaging facilities worldwide. It is important to involve the high-end facilities to assure that the proposed QA procedure is suited for all available cases. For more detailed information see contributed papers by Pugliesi et al., Radebe et al., and Sim et al.

2.6.5. Scientific output

Two contributions related to the analysis of the image data were presented during the International Topical Meeting on Neutron Radiography 7 (ITMNR-7) in Kingston, Canada during 2012. The contributions are also accepted for publication in the conference proceedings. The proceeding was published by Physics Procedia (Elsevier). The paper by Radebe et al. [51] presents the phantoms and provides a histogram-based evaluation of the contrast phantom to show the impact of the choice of reconstruction filter. The appendix of this paper provides a practical guideline for performing a standardized CT experiment. The paper by Kaestner et al. [49] describes the image processing required to automate the image evaluation. The automated evaluation routine is required to avoid the impact of human interaction during the evaluation.

2.6.6. Conclusion

The results of calculations and studies of the 13 participating countries on using the IAEA supported test samples NTC and NTSR were collected and verified. It was concluded that for some participants current measurement procedures and experiment protocols seem to be complex to follow since often the information in the returned experiment forms was incomplete. Often the storage media included in the sample box for storing the experiment data and experiment report was empty. This made the overall evaluation of the Round Robin experiment more difficult. In some cases the missing information was completed by the local contacts upon request. During the follow up IAEA technical meeting, held in November 2012 in Jakarta, it became clear that the data was often missing since the people performing the experiments had very little experience with the use of reconstruction software and did not manage to do the data processing. To improve this, there was a tutorial at the technical meeting where most frequently used reconstruction software (Octopus) was demonstrated.

It was decided, after consultation, to change the overall approach in the standardization exercise from establishing standards for 3D tomography to standards for 2D radiography and only then proceed to 3D standardization.

The design for the current 3D spatial resolution test object is inadequate due to visibility of the foil even when it is smaller than the pixel size simply because the thickness and attenuation of the foil renders it visible due partial volume effects. The specific design was not discussed and limited consultation with the participating member states took place in the exercise. The needed due processes such as discussions, assessment and optimization stages were not followed and therefore will need some follow up in the future.

The spatial resolution will be investigated through an edge method and the first 2D test object for this purpose has been designed and manufactured. The evaluation will be based on the edge analysis method of a projection and reconstructed slice for radiography and tomography respectively. The automated analysis method is currently undergoing development. The design of the 3D edge test object is being discussed by participating facility members.

Noise characterization of radiographs is one of the quality metrics for which preliminary work has been conducted and more detailed work which will look at the pixel-wise context will be conducted at a later stage in the Round Robin exercise.

The experience with the 3D contrast sample shows that the Polyethylene inset is attenuating the neutron beam in a too strong manner, which causes starvation artefacts in the reconstructed slices. An alternative inset made from Ti, replacing the PE inset, was manufactured to avoid this effect. The 2D contrast test object is yet to be designed and manufactured.

There was a time constraint on the Round Robin experiment, which pushed the shipping of the samples to an early date. Due to this constraint it was not possible to work out a more detailed evaluation or to make some sample design iterations before the samples had to be shipped. One example is the PE inset in the contrast sample, which actually destroys the results since it interferes with the contrast readings of the other insets.

3. CONCLUSIONS

The IAEA coordinated research project "Development, Characterization and Testing of Materials of Relevance to Nuclear Energy Sector Using Neutron Beams" (CRP 1575) brought together stakeholders and end users of neutron scattering and imaging facilities to investigate materials for applications in nuclear energy sector. The CRP was an optimal framework to network different international groups dealing with the characterization and developing of nuclear materials, to establish new cooperation or refresh the existing one. The scientific presentations and discussions at the project meetings inspired new experiments and provided valuable results. A number of Round Robin exercises proved to be an effective way for testing and harmonizing the experimental methods applied and the reproducibility of the effects observed in the materials. It also has been shown through concrete examples that neutron scattering and imaging facilities could be improved thanks to the cooperation among groups with long experiences leading in their field and groups developing/modernizing their facilities.

It was acknowledged by all participants that this CRP was a successful and extremely valuable project: a broad spectrum of high level expertise was gathered, good equilibrium among developed and developing countries, providing a great opportunity for joint activities and complementary neutron beam techniques for material research and characterization. The important role and unique capability of neutron scattering in this particular field was highlighted, e.g. work with bulk materials, possibility to investigate radioactive samples, studies of samples in the presence of magnetic fields and tests of sensitivity to hydrogen at extreme conditions, and certainly should continue in the future.

In summary, the CRP scientific topics mainly focused on the material groups such as steels, nickel based superalloys and zirconium alloys. The most important methods employed were:

- Neutron diffraction applied for the investigation of the phase compositions, the determination of dislocation densities and in particular for residual strain/stress measurements;
- Small angle neutron scattering to investigate inhomogeneities like irradiation defects or hydrogen precipitates;
- Neutron radiography and tomography to investigate macroscopic defects or element/isotope distributions.

In order to continue the established cooperation among sub-groups as a result of this CRP, the following follow up activities were indicated:

- Preparation and sharing of specimens needed to perform joint activities, e.g. Round Robin for imaging, standardization for neutron diffraction and SANS, and other research with representative samples of interest and by use of complementary techniques;
- Development of a dedicated information portal/forum for exchange of information and documentation, and maintain constant networking within joint activities;
- Promotion and implementation of the exchange of young scientists among the project partners, e.g. through existing Technical Cooperation projects, possibilities through so-called PhD type CRPs and funding under bilateral and regional agreements;

- Facilitation and support of technical meetings, workshops and schools related to research and applications using neutron beams; some specific research areas were highlighted in this context:

    - Zr based materials and H uptake related issues;
    - Research related to irradiated materials at high doses and fluences;
    - Standardization of neutron imaging and other neutron beam techniques.

REFERENCES

[1] MITTEMEIJER, E. J., WELZEL U., The state-of-the-art of the diffraction analysis of crystallite size and lattice strain, Z. Kristallogr. **223** (2008) 552 – 560.

[2] OHNUMA, M., et al., A new method for the quantitative analysis of the scale and composition of nanosized oxide in 9Cr-ODS steel, Acta Materialia **57** (2009) 5571–5581.

[3] COPPOLA, R., RODRIGUEZ-CARVAJAL, J., WANG, M., ZHANG, G., ZHOU, Z., High-resolution neutron diffraction crystallographic investigation of oxide dispersion strengthened steels of interest for fusion technology, pres. at ICFRM16 and J. N. Mat **455** (2014) 426-430.

[4] HE, P., KLIMENKOV, M., LINDAU, R., MOSLANG, A., J. Nucl. Mater. **428** (2012) 131.

[5] ROGOZHKIN, S. V., ALEEV, A. A., ZALUZHNYI, A. G., ISKANDEROV, N. A., NIKITIN, A. A., VLADIMIROV, P., LINDAU, R., MOESLANG, A., Atom Probe tomography of nanoscaled features of oxide-dispersion-strengthened ODS Eurofer steel in the initial state and after neutron irradiation, The Physics of Metals and Metallography, **113** 1, (2012) 98-105.

[6] SZÁRAZ, Z., et al., SANS investigation of microstructure evolution in high chromium ODS steels after thermal ageing, J. Nucl. Mater. **435** (2013) 56-62.

[7] FISCHER, P., et al., Physica B 276-278 (2000) 146.

[8] Crystallographic tools for Rietveld, profile matching & integrated intensity refinements of X ray and /or neutron data. http://www.ill.eu/sites/fullprof/

[9] General Structure Analysis System (GSAS), http://www.ccp14.ac.uk/solution/gsas/

[10] UNGAR, T., et al., The contrast factors of dislocations in cubic crystals: the dislocation model of strain anisotropy in practice, J. Appl. Cryst. **32** (1999) 992-1002.

[11] HOLT, R. A., J. Nucl. Mater. **372** (2008) 182-214.

[12] KEARNS, J. J., J. Nucl. Mater. **299** (2001) 171-174.

[13] LEWIS, J. E., et al, Proc. 5th Intern. Symp. on Zirconium in Nucl. Ind., ASTM STP 754 (1982) 39-62.

[14] BALOGH, L., ed al., Acta Materialia **60** (2012) 5567–5577.

[15] GROSSE, M. K., et al., Physics procedia **43** (2013) 294 – 306.

[16] GROSSE, M., STUCKERT, J., STEINBRÜCK, M., KAESTNER, A., Secondary hydriding during LOCA – Results from the QUENCH-L0 test, J. Nucl. Mater., **420** (2012), 575 – 582.

[17] PRESTEL, S., GROSSE, M., "Investigation of the annealing behaviour of hydride precipitates in Zircaloy-4", Steinbrück, M. [Ed.], (Proc. of the 18th Internat. QUENCH Workshop, Karlsruhe, November 20-22, 2012), CD-ROM, Karlsruhe, Karlsruhe Inst. of Technology, Campus North (2012).

[18] HUTCHINGS, M.T. and KRAWITZ, A.D., [ed.], Measurements of Residual and Applied Stress using Neutron Diffraction, Kluwer–Academic, Dordrecht (1992).

[19] VRÁNA, M., MIKULA, P., "Residual stress investigations of electron beam welds on samples prepared by reconstitution method", In Proc. of Int. Conf. EAN (Experimental Analysis of Stresses), Litoměřice, June 11-13, 2013, Applied Mechanics and Materials, **486** (2014) pp. 147-150. *doi*:10.4028/www.scientific.net/AMM.486.147.

[20] MRÁZ, L., KARLSSON, L., MIKULA, P., VRÁNA, M., "Identification of Weld Residual Stresses Using Diffraction Methods and their Effect on Fatigue Strength of High Strength Steels Welds", In Proc. of Int. Conf. ICRS9, (Garmisch Partenkirchen, October 7-9, 2012), Materials Science Forum, 768-769 (2014) pp. 668-674. Doi: 10.4028/www.scientific.net/MSF.768-769.668.

[21] MRÁZ, Ľ., KARLSSON, L., VRÁNA, M., MIKULA, P., "Residual stress (RS) distributions at high strength steel welds prepared by low transformation temperature (LTT) and conventional welding consumables", (In Proc. of Int. Conf. MECA SENS 2013, Sydney, Sept. 10-12, 2013) Materials Science Forum 768-769 (2014) 668-674.
[22] STRUNZ, P., SCHUMACHER, G., KLINGELHÖFFER, H., WIEDENMANN, A., SAROUN, J., KEIDERLING, U., In-situ observation of morphological changes of gamma prime precipitates in pre-deformed single-crystal Ni-base superalloy. J. Appl. Cryst. **44** (2011), Part 5, 935-944.
[23] GILLES, R., MUKHERJI, D., ECKERLEBE, H., STRUNZ, P., RÖSLER, J., In situ investigation with neutrons on the evolution of γ ′ precipitates at high temperatures in a single crystal Ni-base superalloy, Advanced Materials Research **278** (2011) 42-47.
[24] HOSEMANN, P. et al., Micro-structural characterization of laboratory heats of the Ferric/Martensitic steels HT-9 and T91, J. Nucl. Mater. **403** (2010) 7–14.
[25] CLAUSEN, B., et al, In situ neutron diffraction and elastic–plastic self-consistent polycrystal modeling of HT-9, J. Nucl. Mater. **425** (2012) 228–232.
[26] BARTON, N. R., ARSENLIS, A., MARIAN, J., A polycrystal plasticity model of strain localization in irradiated iron, J. Mechanics and Physics of Solids (2012).
[27] ANDEROGLU, O. et al., Phase stability of an HT-9 duct irradiated in FFTF, J. Nucl. Mater. (2012).
[28] VANDERMEULEN, W., et al., Measurement of the Young modulus anisotropy of a reactor pressure vessel cladding, J. Nucl. Mater. **372** (2008) 249–255.
[29] SCHMATZ, W., "Proceedings of the Conference on Neutron Scattering. Gatlinburg", Tennessee, USA, June 6-10, 1976, vol. 2, 1037.
[30] SVERGUN, D.I., FEIGIN, L.A., X ray and neutron small angle scattering, Science, 1986, 34., available in Russian only as СВЕРГУН, Д.И., ФЕЙГИН, Л.А., "Рентгеновское и нейтронное малоугловое рассеяние" М: Наука, 1986. 34.
[31] BALE, H.D., SCHMIDT, P.W., Small angle X-ray scattering investigation of submicroscopic porosity with fractal properties, Phys. Rev. Lett. **53**, (1984) 596-604.
[32] DEBYE P., ANDERSON H.R., BRUMBERGER H., Scattering by an inhomogeneous solid. II. The correlation function and its application, J. Apll. Phys. **28**, (1957) 679-684.
[33] VALIEV, E.Z., OSTROUSHKO, A.A., BOGDANOV, S.G., PIROGOV, A.N., TEPLYKH, A.E., MOGILNIKOV, YU.V., Processes of oxygen phase formation with participation of both polymer-saline complexes molybdate and ammonium wolfram, Surface, X-rays, synchrotron and neutron examination, **11**(2001) 38-48.
[34] BOGDANOV, S.G., GOSHCHITSKII, B.N., PARKHOMENKO, V.D., LEONTIEVA-SMIRNOVA, M.V., CHERNOV, V.M., Small-Angle Neutron Scattering Investigation of Nanostructure of Ferritic-Martensitic 12%-Chromium Steels, Physics of the Solid State. **56** (2014) 1-13.
[35] TREMSIN, A. S., et al., Non-destructive studies of fuel pellets by neutron resonance absorption radiography and thermal neutron radiography, J. Nucl. Mater. **440** (2013), 633–646.
[36] PINCHOVIUS, L., JUNG, V., MACHERAUCH, E., VÖHRINGER, O., Residual Stress Measurements by Means of Neutron Diffraction, Materials Science and Engineering **61** (1983) 43–50.
[37] BACON, G.E., Neutron Diffraction, Oxford, Clarendon Press (1975).
[38] MIKULA, P., LUKÁŠ, P., ŠAROUN, J., WAGNER, V., KULDA, L., Cylindrically Bent Perfect Crystals as Neutron Monochromators, Physica B, **213&214** (1995) 922-925.
[39] POPOVICI, M., YELON, W.B., Focusing Monochromators for Neutron Diffraction, J. Neutron Research, **3** (1995) 1-25.

[40] MIKULA, P., KULDA, J., LUKÁŠ, P., VRÁNA, M., WAGNER, V., Bent Perfect Crystals in Asymmetric Diffraction Geometry in Neutron Scattering Experiments, Nucl. Instrum. Methods in Phys. Res. A 338 (1994) 18-26.
[41] MIKULA, P., VRÁNA, M., LUKÁŠ, P., ŠAROUN, J., WAGNER, V., High-Resolution Neutron Powder Diffractometry on Samples of Small Dimensions, Mat. Science Forum, 228–231 (1996) 269–274.
[42] MIKULA, P., WAGNER, V., Strain Scanning Using a Neutron Guide Diffractometer, Materials Sc. Forum 347–349 (2000) 113–118.
[43] MIKULA, P., KULDA, J., LUKÁŠ, P., ONO, M., ŠAROUN, J., VRÁNA, M., WAGNER, V., Bragg diffraction optics in neutron diffractometry, Physica **B 283**, (2000) 289–294.
[44] MIKULA, P., KULDA, J., VRÁNA, M., CHALUPA, B., A Proposal of a Highly Efficient Double Crystal Monochromator for Thermal Neutrons, J. Appl. Cryst. **17** (1984) 189-195.
[45] SEONG, B.S., EM, V., MIKULA, P., ŠAROUN, J., KANG, M.-H., Optimization of a bent perfect Si(111) monochromator at a small take-off angle for use in a stress instrument, J. Appl. Cryst., **43** (2010) 654–658.
[46] HSU, T.C., MARSIGLIO, F., ROOT, J.H., HOLDEN, T., Effect of Multiple Scattering and Wavelength Dependent Attenuation on Strain Measurements by Neutron Scattering, J. Neutron Res., **3** (1) (1995) 27-39.
[47] WOO, W., EM, V., MIKULA, P., AN, G.B., SEONG, B.S., Neutron diffraction measurements of residual stresses in a 50 mm thick weld, Materials Sc. Eng. A **528** (2011) 4120-4124.
[48] WOO, W., EM, V., SEONG, B.S., SHIN, E., MIKULA, P., JOO, J., KANG, M.H., Effect of wavelength-dependent attenuation on neutron diffraction stress measurements at depth in steels, J. Appl. Cryst., **44** (2011) 747–754.
[49] KAESTNER, A. P., et al. Verifying neutron tomography performance using test objects, Nuclear Instruments and Methods in Physics Research, A**651** (2012) 156-160.
[50] SAMEI, E., REIMANN, D. A., A method for measuring the presampled MTF of the digital radiographic systems using an edge test device, Med. Phys. **25**, (1998) 102-113.
[51] RADEBE, M. J., et al., Evaluation Procedures for Spatial Resolution and Contrast Standards for Neutron Tomography, Nuclear Instruments and Methods in Physics Research, A**651** (2012) 282-285.

ABBREVIATIONS

APT	Atom probe tomography
BPC	Bent perfect crystal
CD	Computed radiography
CRP	Coordinated research project
CT	Computed tomography
DHC	Delayed hydride cracking
DLPA	Advanced line profile analysis
DPA	Displacement per atom
DR	Digital radiography
EBW	Electron beam welding
EM	Electron microscopy
EPSC	Elasto-plastic self-consistent
FFTF	Fast flux test reactor facility
FOV	Field of view
FOM	Figure of merit
FWHM	Full width at half maximum
IRF	Instrumentation resolution file
LOCA	Loss of coolant accidents
LTT	Low transformation temperature
NCT	Neutron computed tomography
ND	Neutron diffraction
NDT	Non-destructive testing
NI	Neutron imaging
NT	Neutron tomography
NTC	Neutron tomography contrast
NTSR	Neutron tomography spatial resolution

ODF	Orientation distribution functions
ODS	Oxide dispersed strengthened
PAS	Positron annihilation spectroscopy
PE	Polyethylene
PSD	Position sensitive detector
QA	Quality assurance
RPV	Reactor pressure vessel
RR	Research reactors
SANS	Small angle neutron scattering
SAXS	Small angle X ray scattering
STM	Scanning tunnelling microscopy
TEM	Transmission electron microscopy
TOF	Time of flight
XRD	X ray diffraction
XRT	X ray tomography

CONTRIBUTORS TO DRAFTING AND REVIEW

Balagurov, A.	Joint Institute for Nuclear Research, Russian Federation
Bartholomew, K.	International Atomic Energy Agency
Desai, T.	International Atomic Energy Agency
Grosse, M.	Karlsruhe Institut of Technology, Germany
Inozemtsev, V.	International Atomic Energy Agency
Kaestner, A.	Paul Scherrer Institut, Switzerland
Lehmann, E.	Paul Scherrer Institut, Switzerland
Mikula, P.	Nuclear Physics Institute, Czech Republic
Rabede, M.	South African Nuclear Energy Corp., South Africa
Ridikas, D.	International Atomic Energy Agency
Török, G.	Wigner Research Institute, Institute of Solid State Physics. Hungary
Santisteban, J.	Comisión Nacional de Energía Atómica, Argentina

Research Coordinated Meetings

Vienna, Austria: 31 May-4 June 2010

Beijing, China: 19-23 September 2011

Dubna, Russian Federation: 13-17 May 2013

LIST OF INDIVIDUAL PAPER CONTRIBUTORS

All contributions are available on attached CD-ROM.

TOPIC 2: RESULTS ACHIEVED

2.1. INVESTIGATION OF OXIDE-DISPERSED-STRENGTHENED STEELS

Author	Affiliation	Title of the paper
Balagurov, A.	Joint Institute for Nuclear Research (JINR), Russian Federation	Investigation of Precipitation-Hardened Steels using TOF Neutron Diffraction
Coppola, R.	National Agency for New Technologies, Energy and Sustainable Economic Development (ENEA), Italy	Characterization of Y_2O_3 particle distribution in Oxide Dispersion Strengthened Eurofer steel for nuclear applications by means of small-angle neutron scattering (SANS) and of neutron diffraction

2.2. RESEARCH ON ZIRCONIUM BASED MATERIALS (INCLUDING HYDROGEN UPTAKE)

Bourke, M.A.M.	Los Alamos National Laboratory (LANL), United States of America	Final report describing neutron scattering activity at Los Alamos National Laboratory in the context of IAEA CRP F1.20.23
Grosse*, M.	Karlsruhe Institut of Technology (KIT), Germany	In-situ neutron radiography investigations of the hydrogen re-distribution during DHC
Grosse**, M.	Karlsruhe Institut of Technology (KIT), Germany	Post-test examination of the hydrogen distribution in zirconium claddings after LOCA tests
Grosse***, M.	Karlsruhe Institut of Technology (KIT), Germany	Small angle neutron scattering investigations of hydride precipitations in Zircaloy-4
Lehmann, E.	Paul Scherrer Institut (PSI), Switzerland	Final report about activities at PSI, Switzerland
Santisteban*, J.	Comisión Nacional de Energía Atómica (CNEA), Argentina	Preliminary Round Robin on the determination of crystallographic texture of Zr components by neutron diffraction
Santisteban**, J.	Comisión Nacional de Energía Atómica (CNEA), Argentina	Crystallographic phases, texture and dislocation densities of ZR2.5%NB pressure tubes at different stages of manufacturing

2.4. RESULTS WITH IRRADIATED MATERIALS

Kozlov, A.	Institute of Nuclear Materials, Russian Federation	Examination of austenitic steels microstructure change induced neutron irradiation by using of neutron scattering methods
Liu, Y.	China Institute of Atomic Energy, (CIAE), Republic Of China	Development, Characterization and Testing of Materials of Relevance to Nuclear Energy Sector Using Neutron Beams in China
Shikama, T.	Tohoku University, Japan	Neutron beam analyses on materials for nuclear applications, being irradiated in fission reactors and having radioactivity
Török, G.	Wigner Research Institute, Institute of Solid State Physics. Hungary	Investigation of irradiation RPV and ODS steels by SANS and residual stress

2.5. OPTIMIZATION OF INSTRUMENTS FOR RESIDUAL STRAIN/STRESS MEASUREMENTS

Carr, D.	Australian Nuclear Science and Technology Organisation (ANSTO), Australia	Final report on evaluating residual stresses and internal defects in nuclear materials at the Opal reactor at ANSTO, Australia
Mikula, P.	Nuclear Physics Institute (NPI), Czech Republic	Development and optimization of high-resolution neutron scattering instruments dedicated to characterization and testing of materials of relevance to nuclear energy sector and related experiments in SANS, residual strain/stress and texture studies
Sutiarso, S.	National Nuclear Energy Agency (BATAN), Indonesia	Optimization of Neutron Beam Techniques for Characterization of Structural Materials

2.6. EFFORTS TOWARDS STANDARDIZATION OF NEUTRON IMAGING

Pugliesi, R.	Instituto de Pesquisas Energeticas e Nucleares (IPEN), Brazil	Improvement of a neutron tomography facility
Radebe, M.	South African Nuclear Energy Corp. (NECSA), South Africa	Use of neutron beam line facilities for nuclear materials related R&D with emphasis on international benchmarking of the technique
Sim, C.	Korea Atomic Energy Research Institute (KAERI), Republic of Korea	Neutron tomography Standardization using NTR and NTC Phantom for industry application

IAEA
International Atomic Energy Agency

No. 23

ORDERING LOCALLY

In the following countries, IAEA priced publications may be purchased from the sources listed below or from major local booksellers.

Orders for unpriced publications should be made directly to the IAEA. The contact details are given at the end of this list.

AUSTRALIA
DA Information Services
648 Whitehorse Road, Mitcham, VIC 3132, AUSTRALIA
Telephone: +61 3 9210 7777 • Fax: +61 3 9210 7788
Email: books@dadirect.com.au • Web site: http://www.dadirect.com.au

BELGIUM
Jean de Lannoy
Avenue du Roi 202, 1190 Brussels, BELGIUM
Telephone: +32 2 5384 308 • Fax: +32 2 5380 841
Email: jean.de.lannoy@euronet.be • Web site: http://www.jean-de-lannoy.be

CANADA
Renouf Publishing Co. Ltd.
5369 Canotek Road, Ottawa, ON K1J 9J3, CANADA
Telephone: +1 613 745 2665 • Fax: +1 643 745 7660
Email: order@renoufbooks.com • Web site: http://www.renoufbooks.com

Bernan Associates
4501 Forbes Blvd., Suite 200, Lanham, MD 20706-4391, USA
Telephone: +1 800 865 3457 • Fax: +1 800 865 3450
Email: orders@bernan.com • Web site: http://www.bernan.com

CZECH REPUBLIC
Suweco CZ, spol. S.r.o.
Klecakova 347, 180 21 Prague 9, CZECH REPUBLIC
Telephone: +420 242 459 202 • Fax: +420 242 459 203
Email: nakup@suweco.cz • Web site: http://www.suweco.cz

FINLAND
Akateeminen Kirjakauppa
PO Box 128 (Keskuskatu 1), 00101 Helsinki, FINLAND
Telephone: +358 9 121 41 • Fax: +358 9 121 4450
Email: akatilaus@akateeminen.com • Web site: http://www.akateeminen.com

FRANCE
Form-Edit
5 rue Janssen, PO Box 25, 75921 Paris CEDEX, FRANCE
Telephone: +33 1 42 01 49 49 • Fax: +33 1 42 01 90 90
Email: fabien.boucard@formedit.fr • Web site: http://www.formedit.fr

Lavoisier SAS
14 rue de Provigny, 94236 Cachan CEDEX, FRANCE
Telephone: +33 1 47 40 67 00 • Fax: +33 1 47 40 67 02
Email: livres@lavoisier.fr • Web site: http://www.lavoisier.fr

L'Appel du livre
99 rue de Charonne, 75011 Paris, FRANCE
Telephone: +33 1 43 07 50 80 • Fax: +33 1 43 07 50 80
Email: livres@appeldulivre.fr • Web site: http://www.appeldulivre.fr

GERMANY
Goethe Buchhandlung Teubig GmbH
Schweitzer Fachinformationen
Willstätterstrasse 15, 40549 Düsseldorf, GERMANY
Telephone: +49 (0) 211 49 8740 • Fax: +49 (0) 211 49 87428
Email: s.dehaan@schweitzer-online.de • Web site: http://www.goethebuch.de

HUNGARY
Librotade Ltd., Book Import
PF 126, 1656 Budapest, HUNGARY
Telephone: +36 1 257 7777 • Fax: +36 1 257 7472
Email: books@librotade.hu • Web site: http://www.librotade.hu

INDIA
Allied Publishers
1st Floor, Dubash House, 15, J.N. Heredi Marg, Ballard Estate, Mumbai 400001, INDIA
Telephone: +91 22 2261 7926/27 • Fax: +91 22 2261 7928
Email: alliedpl@vsnl.com • Web site: http://www.alliedpublishers.com

Bookwell
3/79 Nirankari, Delhi 110009, INDIA
Telephone: +91 11 2760 1283/4536
Email: bkwell@nde.vsnl.net.in • Web site: http://www.bookwellindia.com

ITALY
Libreria Scientifica "AEIOU"
Via Vincenzo Maria Coronelli 6, 20146 Milan, ITALY
Telephone: +39 02 48 95 45 52 • Fax: +39 02 48 95 45 48
Email: info@libreriaaeiou.eu • Web site: http://www.libreriaaeiou.eu

JAPAN
Maruzen Co., Ltd.
1-9-18 Kaigan, Minato-ku, Tokyo 105-0022, JAPAN
Telephone: +81 3 6367 6047 • Fax: +81 3 6367 6160
Email: journal@maruzen.co.jp • Web site: http://maruzen.co.jp

NETHERLANDS
Martinus Nijhoff International
Koraalrood 50, Postbus 1853, 2700 CZ Zoetermeer, NETHERLANDS
Telephone: +31 793 684 400 • Fax: +31 793 615 698
Email: info@nijhoff.nl • Web site: http://www.nijhoff.nl

Swets Information Services Ltd.
PO Box 26, 2300 AA Leiden
Dellaertweg 9b, 2316 WZ Leiden, NETHERLANDS
Telephone: +31 88 4679 387 • Fax: +31 88 4679 388
Email: tbeysens@nl.swets.com • Web site: http://www.swets.com

SLOVENIA
Cankarjeva Zalozba dd
Kopitarjeva 2, 1515 Ljubljana, SLOVENIA
Telephone: +386 1 432 31 44 • Fax: +386 1 230 14 35
Email: import.books@cankarjeva-z.si • Web site: http://www.mladinska.com/cankarjeva_zalozba

SPAIN
Diaz de Santos, S.A.
Librerias Bookshop • Departamento de pedidos
Calle Albasanz 2, esquina Hermanos Garcia Noblejas 21, 28037 Madrid, SPAIN
Telephone: +34 917 43 48 90 • Fax: +34 917 43 4023
Email: compras@diazdesantos.es • Web site: http://www.diazdesantos.es

UNITED KINGDOM
The Stationery Office Ltd. (TSO)
PO Box 29, Norwich, Norfolk, NR3 1PD, UNITED KINGDOM
Telephone: +44 870 600 5552
Email (orders): books.orders@tso.co.uk • (enquiries): book.enquiries@tso.co.uk • Web site: http://www.tso.co.uk

UNITED STATES OF AMERICA
Bernan Associates
4501 Forbes Blvd., Suite 200, Lanham, MD 20706-4391, USA
Telephone: +1 800 865 3457 • Fax: +1 800 865 3450
Email: orders@bernan.com • Web site: http://www.bernan.com

Renouf Publishing Co. Ltd.
812 Proctor Avenue, Ogdensburg, NY 13669, USA
Telephone: +1 888 551 7470 • Fax: +1 888 551 7471
Email: orders@renoufbooks.com • Web site: http://www.renoufbooks.com

United Nations
300 East 42nd Street, IN-919J, New York, NY 1001, USA
Telephone: +1 212 963 8302 • Fax: 1 212 963 3489
Email: publications@un.org • Web site: http://www.unp.un.org

Orders for both priced and unpriced publications may be addressed directly to:

IAEA Publishing Section, Marketing and Sales Unit, International Atomic Energy Agency
Vienna International Centre, PO Box 100, 1400 Vienna, Austria
Telephone: +43 1 2600 22529 or 22488 • Fax: +43 1 2600 29302
Email: sales.publications@iaea.org • Web site: http://www.iaea.org/books

15-37201

International Atomic Energy Agency
Vienna
ISBN 978–92–0–108915–1
ISSN 1011–4289